LONG-LIVED NEUTRAL HADRONS IN THE CALORIMETER OF THE ZEUS DETECTOR

FARIDAH MOHAMAD IDRIS

FACULTY OF SCIENCE
UNIVERSITY OF MALAYA
KUALA LUMPUR

2011

LONG-LIVED NEUTRAL HADRONS
IN THE CALORIMETER OF THE ZEUS DETECTOR

FARIDAH MOHAMAD IDRIS

**THESIS SUBMITTED IN THE FULFILLMENT OF
THE REQUIREMENT FOR THE DEGREE
OF DOCTOR OF PHILOSOPHY**

**DEPARTMENT OF PHYSICS
FACULTY OF SCIENCE
UNIVERSITY OF MALAYA
KUALA LUMPUR**

2011

UNIVERSITI MALAYA

ORIGINAL LITERARY WORK DECLARATION

Name of Candidate: FARIDAH MOHAMAD IDRIS (I.C/Passport No: 651031-02-5788)

Registration/Matric No: SHC060001

Name of Degree: DOCTOR OF PHILOSOPHY

Title of Project Paper/Research ReportiDissertationlThesis ("this Work"):
LONG-LIVED NEUTRAL HADRONS IN THE CALORIMETER OF THE ZEUS DETECTOR

Field of Study: NUCLEAR AND PARTICLE PHYSICS

I do solemnly and sincerely declare that:

(1) I am the sole author/writer of this Work;
(2) This Work is original;
(3) Any use of any work in which copyright exists was done by way of fair dealing and for permitted purposes and any excerpt or extract from, or reference to or reproduction of any copyright work has been disclosed expressly and sufficiently and the title of the Work and its authorship have been acknowledged in this Work;
(4) I do not have any actual knowledge nor do I ought reasonably to know that the making of this work constitutes an infringement of any copyright work;
(5) I hereby assign all and every rights in the copyright to this Work to the University of Malaya ("UM"), who henceforth shall be owner of the copyright in this Work and that any reproduction or use in any form or by any means whatsoever is prohibited without the written consent of UM having been first had and obtained;
(6) I am fully aware that if in the course of making this Work I have infringed any copyright whether intentionally or otherwise, I may be subject to legal action or any other action as may be determined by UM.

Candidate's Signature Date: 22.12.2010

Subscribed and solemnly declared before,

Witness's Signature Date:

Name: PROF DR WAN AHMAD TAJUDDIN WAN ABDULLAH
Designation: DEAN, FACULTY OF COMPUTER SCIENCE AND INFORMATION TECHNOLOGY, UNIVERSITY OF MALAYA

Witness's Signature Date: 23.12.2010

Name: PROF DR ZAINOL ABIDIN IBRAHIM
Designation: LECTURER, PHYSICS DEPARTMENT, FACULTY OF SCIENCE, UNIVERSITY OF MALAYA

ABSTRACT

During the electron-proton collision at HERA, the long-lived neutral hadrons in their final states may travel from the centre of the ZEUS detector to reach the calorimeter and deposit its energy in the calorimeter as islands of energies. The neutral hadrons travel in straight path and were not deflected by the magnetic field in the ZEUS detector.

In this thesis, measurements of the long-lived neutral hadrons K_L^0 and neutron in the final states in the calorimeter of the ZEUS detector has been carried out using the energy deposited by ZEUS Unidentified Flow Objects (ZUFOs) that were not associated with any tracks.. The kinematic variables of K_L^0 has been measured with virtual photon gain $0 < Q^2 < 150 GeV^2$ and centre-of-mass for intermediate boson-proton $W_{JB} = 25 GeV$. The reconstruction of invariant mass of vector meson $\phi(1020)$ using decay $\phi(1020) \to K_L^0\ K_S^0$ and baryon Λ through decay channel $\Lambda \to n\ \pi^0$ has been carried out, with both showing good agreement with the standard invariant mass [35] of $\phi(1020)$ and Λ. The differential cross sections of $\phi(1020)$ and Λ and their respective daughter of K_L^0 and neutron with respect to their momentum were also calculated.

ACKNOWLEDGEMENT

I would like to thank and extend my gratitude to all the people involved in making this project a success.

First of all, I would like express my debt and gratitude to my supervisor Prof Dr Wan Ahmad Tajuddin Wan Abdullah and my co-supervisor Prof Dr Zainol Abidin Ibrahim, both of Jabatan Fizik, Unversiti Malaya, Kuala Lumpur, for their guidance, patience and support in the duration of this project.

I would also like thank ZEUS collaboration and Deutsches Electronen Synchrotron (DESY) for supporting this research project. I would also like thank my department Malaysian Nuclear Agency and Ministry of Science Technology and Innovation (MOSTI) of Malaysia for their support in this project.

For those whose name I do not mention here but have helped me in one way or another, please accept my sincere thank and gratitude. Thank you all very much.

PREFACE

In quest for knowledge, the endeavors put together by all parties to make a project undertaken a success is much more meaningful, than an individual alone. Such quest for the understanding the structure of matter to its most basic building block is an infinity. Save for the occasional tiredness of the mind and body, the hunger to understand more of nature's phenomena will perhaps push one's mind and capability towards excellence.

Thus, this project is dedicated to all mankind in pursuit of knowledge, may we be united by the knowledge that knowledge knows no boundaries.

TABLE OF CONTENTS

List of Figures

Figure 6.20 Reconstructed momentum (in GeV) of K_S^0 candidates (a) momentum of K_S^0 with (b) in x-direction; (b) y-direction (c) in z-direction

List of Tables

CHAPTER 1

INTRODUCTION

In experimental particle physics, the study of the smallest known particle using particle accelerator provides the mankind the instrument to understand the fundamental building blocks of deep within the atoms and its relation to the universe as a whole.

In a particle accelerator, the two beams accelerating from the opposite direction collided and interacted at the scale deep within the atom to produce quarks, neutrinos, leptons and fragmentations from the interaction to challenge the theories that form these observed phenomena.

At Hadron Electron Ring Accelerator (HERA), the collision of electron and proton, accelerated 30GeV and 920GeV respectively in the opposite direction has been used to probe the internal structure of proton. In the ZEUS detector at HERA, the energy and the momentum of the particles produced during the electron-proton collision was recorded by the detectors surrounding the interaction point of the ZEUS detector such as the central tracking detector (CTD) and the hadronic and electromagnetic calorimeters.

While charge particles were often used to reconstruct the kinematic variables of the electron-proton collision in the ZEUS detector, the reconstruction of variables of neutral particles using the uncharged tracks in the ZEUS detector has not been extensively explored. In this thesis we explored the methodology of using uncharged tracks in the calorimeter of the ZEUS detector to reconstruct the long-lived neutral hadrons in the final states, i.e. K_L^0.and neutron *n*, by using the energy deposits of the uncharged ZEUS unidentified energy flow (ZUFOS) objects in the hadronic calorimeter of the ZEUS detector.

The characteristics of K_L^0.and neutron *n*, which has sufficiently long decay length to reach the hadronic calorimeter (HACs) without decaying were used to differentiate the potential K_L^0.and neutron *n* candidates. From identification the potential candidates of these long-lived neutral hadrons the source of K_L^0.and neutron *n* production were narrowed to $\phi(1020)$ and Λ.

The study of strange content of light unflavored meson $\phi(1020)$ $s\bar{s}$ from the mixing of vector meson (ρ, ω, ϕ) and the fragmentation of baryon Λ with quark uds, both as results from the interaction of electron-proton at high energy, carried out with the decay channels $\phi \to K_L^0 K_S^0$ and $\Lambda \to n\pi^0$ respectively, using the measured neutral energy particles deposited in the hadronic calorimeter (HAC) of the ZEUS will give a new information on strangeness conservation and CP (charge conjugate and parity) violation, since both ϕ and Λ decay into neutral particles K_L^0, K_S^0 .and n, π^0 respectively.

It will also give a novel method of data analysis for long-live neutral particle using energy deposits in HAC, conventionally carried out using charge particles detection in the CTD (central tracking detector). The information from the neutral energy deposits by neutral particles in the HACs then could be backtracked to CTD vertex to provide more information on the neutral particle trajectory and its origin.

The objective of this thesis is to establish methodology for indentifying long-lived neutral hadrons in the final state, using energy deposited by the long-lived neutral hadrons in the calorimeter of the ZEUS detector. The development of readout control of the calorimeter of the ZEUS detector that includes the software controller and hardware implementation, and halomuon analysis of the ZEUS detector are also included in this thesis, as part of Malaysian contribution to the experimental high energy physics especially for ZEUS collaboration.

In Chapter 2 of this thesis, theoretical reviews that form the basis of the research carried out in this thesis is given. In Chapter 3, setup ZEUS of Experiment at HERA and the Monte Carlo simulation performed simultaneously with the on-line ZEUS experiment is discussed.

In Chapter 4, the Readout Control (ROC) simulated for the ZEUS calorimeter data taking and halomuon analysis carried out in the ZEUS detector are discussed. In Chapter 5, event reconstruction and event selections for reconstructing the $\Lambda \to n\pi^0$ and $\phi \to K_L^0 K_S^0$ channels are described. In Chapter 6, result from the $\Lambda \to n\pi^0$ and $\phi \to K_L^0 K_S^0$ decays reconstruction are given and discussed. Finally in Chapter 7, the conclusion of the research and its future outlook are given.

CHAPTER 2

THEORETICAL REVIEW

To facilitate the understanding of structure of elementary constituents of matter, various quark models have been developed. The Standard Model has been used successfully to describe the existing leptons and quarks within hadrons. In probing the interactions within hadrons, several theories such as the Quark Parton Model (QPM), the Quantum Chromodynamics (QCD), Lund String Fragmentation and Boson Gluon Fusion (BGF) have been used together with the kinematics variables of electron-proton collision to explain the existence of strong and weak interaction within the matter. In this chapter, the various theories involved in kinematics of the long-lived neutral hadrons in the calorimeter of the ZEUS detector were reviewed

2.1 The Standard Model

In high energy physics, research on the structure of elementary constituents of matter and the interaction of radiation with matter is carried out to understand the mechanism of hadrons being bound within the nucleus. The standard model classifies elementary constituents of matter into six leptons and six quarks. The six leptons are electrons (e), muon (μ), tau (τ), electron neutrino (ν_e), muon neutrino (ν_μ) and tau neutrino (ν_τ), while the six quarks, also known as flavors, are up quark (u), down quark (d), charm quark (c) , strange quark (s), top quark (t) and bottom quark (b).

As fermions, leptons are free particles that can be detected, but quarks on the other hand exist in bound states as hadrons and can only be inferred from experimental measurements of the properties of particle interactions and hadron productions [21].

The exchanges of field quanta between these fundamental constituents are governed by three forces –weak, electromagnetic and strong. These forces are mediated by carriers of forces called bosons that comprise of three vector boson mediating weak interactions $(W^{\pm}, Z^0)$, the photon γ mediating electromagnetic and eight gluons mediating the strong interactions. Due to this gluon-gluon force, the quarks are confined within composite particles call hadrons that limit strong interaction to 10^{-15} meters.

As most of the elementary particle do not exist stably outside the confinement of hadrons, but created and detected during energetic collision with other particles, accelerator such as HERA was used as experimental tool to extract information on the kinematic variables of the elementary particles during their creation process.

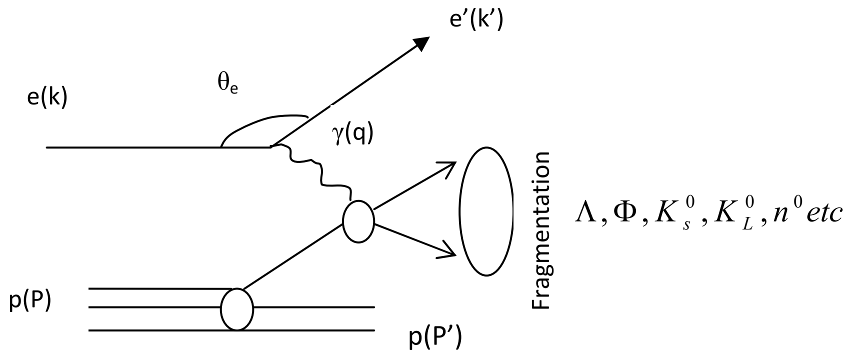

Figure 2.1 Kinematic variables in the electron-proton collision, with P, k , q as the momentum of proton, electron, and photon respectively (generated in the process).

2.2 Quark Parton Model (QPM)

Figure 2.1 shows the Feynman diagram of an electron-proton collision; with a proton p with momentum P colliding with an electron e with momentum k . On collision, the electron loses some of its energy with the emission of virtual photon γ that has a momentum q . The virtual photon then interacts with a quark in the proton resulting in a formation of a new quark, which may decay shortly after, depending on its mean life. The kinematic variables of the collision were measured using ZEUS detector at HERA.

In the quark parton model, the constituents of the proton i.e. two up quarks and one down quarks are assumed to be free and point like, called partons. Thus the electron-proton collision could be viewed as an incoherent sum of a two body that consist of elastic electron - parton, with the scattering cross section weighted by a parton density distribution function $f_i(x)$, given by Callan-Gross relations as [27],

$$F_2(x) = x\sum_i e_i^2 f_i(x) \tag{2.1}$$

and,

$$F_1(x) = \frac{1}{2x} F_2(x) \tag{2.2}$$

with x as the Bjorken scaling variable, F_1 and F_2 as the structure functions e_i as the charge of the parton, and $f_i(x)dx$ is the probability of finding a parton-i in the momentum interval of x and $x+dx$.

In the deep inelastic scattering, partons in the proton structure, the electrons and the emission of virtual photon during the interaction of the electron with the proton, could be viewed point like scattering. During the hadronisation process, the partons were ejected from the electron-proton system to form quarks after interaction with carrier(s) such as bosons, photon or gluons.

2.3 Quantum Chromodynamics (QCD)

In contrast to quark parton model (QPM), the Quantum Chromodynamic (QCD) uses non-abelian gauge theory based on the SU(3) color symmetry group field theory to explain the existence of strong interaction between the quarks. In the SU(3) color symmetry matrices, the process may undergo linear transformation of hadron on 3-dimensional complex linear space C^3. The gluons transform in the adjoint representation of SU(3), which is 8-dimensional, where the quarks are not free but interact through mediating gauge bosons called gluons , which also carry color charge themselves i.e. up (*u*), down (*d*), top (*t*), bottom (*b*), strange (*s*),charm (*c*). Here, a quark may change its flavor (*u,d,t,b,s,c*) and may split into quark and antiquark ($q\bar{q}$) through emission and absorption of gluons [7].

2.3.1 Perturbative Quantum Chromodynamics

In QCD confinement, quarks and gluons do not move freely but are bounded by strong interactions. Partons that are close together behave as free particles have a property known as Asymptotic Freedom. At small separation between the partons, where high energy probe is probable, the Perturbative Quantum Chromodynamics (pQCD) allows the observable associated with a given scattering process to be calculated, in terms of finite expansion series in a coupling constant α_s as [5],

$$f(\alpha_s) = f_1 + f_2\,\alpha_s + f_3\alpha^2 + ... \qquad (2.3)$$

The system is perturbed by the above higher order corrections, the summations run over all possible quark-gluon or gluon-gluon interactions in Feymann diagram of the system. For a Leading Order (LO), the summation runs over a single gluon emission, while a Next-to-Leading order (NLO) includes the second gluon emission or virtual gluon loop from the first gluon emission.

2.4 String Fragmentation And The Lund string Model

Due to color confinement, free quarks and antiquarks created during the electron-proton collision could not exist individually. In the Standard Model, the hadronisation process occurs when these free quarks and antiquarks combine together to form hadrons.

In Lund String Model, the hadronisation of quarks and gluons to form hadrons during the high energy electron-proton collision where free quarks were created, involves the fragmentation of color flux sring-like gluons that are binding the quarks and antiquarks ($q\bar{q}$) into hadrons. The string of strong color field that binds the quark and antiquark may be stretched in the final state radiation, just before hadronisation took place during the electron-proton collision [39].

In the string-fragmentation scheme, the color field between the partons (i.e. quarks and gluons) may be fragmenting itself with the emission of energetic gluon carry “kinks” on the string. If the energy stored in the string is sufficient enough as when two color partons move apart, a $q\bar{q}$ pair may be created from the vacuum. The string may then break repeatedly into color singlet system for as long as the invariant mass of the string pieces exceed on-mass-shell hadrons.

The $q\bar{q}$ was created using the probability the quantum mechanical tunneling process $\exp(-\pi\, m_{q,\perp}^2 / \kappa)$, with transverse mass squared $m_{q,\perp}^2 \equiv m_q^2 + p_{q,\perp}^2$ and string tension $\kappa \approx 1\, GeV / fm$. The transverse momentum $p_{q,\perp}^2$ is locally compensated between the quark and antiquark pair. During the fragmentation, the strange and heavy-quarks production may be suppressed due to the dependence on the parton mass m_q and/or hadron mass m_h. The string-fragmentation function $f(z)$, is given by [40]:

$$f(z) \sim \frac{1}{z}(1-z)^a \exp\left(-\frac{bm_{h,\perp}^2}{z}\right) \qquad (2.4)$$

with $z = \dfrac{(E + p_{\|})_h}{(E + p)_q}$ as the light-cone momentum fraction

$p_{\|}$ as the momentum of formed hadron h along the direction of quark q

$a = 0.11$, $b = 0.54\, GeV^{-2}$ are free parameters adjustable to bring the fragmentation into accordance with measured data.

2.5 Boson Gluon Fusion

In a Deep Inelastic Scattering (DIS) process between a hadron and a lepton, the fragmentation of color partons from the DIS might produce jets of hadrons collimating around the original direction of the partons. The annihilation of leptons into a photon (or a Z^0) with subsequent production of a $q\bar{q}$ pair and the fragmentation of the $q\bar{q}$ pair into jets structure in the final state may emit a gluon with large transverse momentum relative to the parent quark [21].

In Boson Gluon Fusion (BGF), the splitting of gluon into a pair of quarks ($q\bar{q}$) with one of the quarks absorbing a virtual boson (γ^*) might result in the two jets being observed in the final states. **Figure 2.2** illustrates the BGF process of DIS of a hadron and lepton.

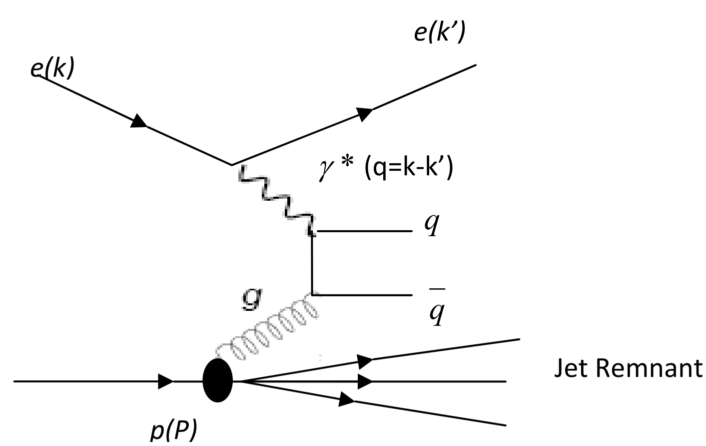

Figure 2.2 Boson Gluon Fusion (BGF) diagram from a Deep Inelastic Scattering (DIS) of a lepton and hadron

2.6 Vector Meson $\phi(1020) \rightarrow K_0^L K_0^s$

In vector meson production, the reaction $ep \rightarrow epV$, the vector meson V represented by (ρ, ω, ϕ) is often referred to as elastic scattering. The Vector meson Dominance Model (VDM) involves the scattering of photon with small virtuality $(Q^2 \approx 0)$ from the irradiation of incoming electron, with the photon acquiring a hadronic structure that allows it to fluctuate into the hadron target during *ep* interaction. At small Q^2 , an ep scattering would involve two processes, namely the radiation of a virtual photon γ^* from the electron, and secondly the scattering of γ^* off the proton with an emission a struck quark from the proton (see **Figure 2.3)** [21].

The electromagnetic coupling of a photon to charge particles allows it to fluctuate into a quark and anti-quark ($q\bar{q}$) pair to interact with a parton inside the photon, when the interaction time was comparable to the lifetime of $q\bar{q}$ fluctuation of the photon [30]. The electromagnetic coupling of the photon to a bound $q\bar{q}$ state that have the same quantum number as the photon could cause the vector meson (ρ, ω, ϕ) fluctuations and scattering elastically off the incoming proton via a pomeron exchange [21] is modeled by the Vector Dominance Model (VDM). The fluctuation of photon into light vector meson production through Vector Dominance Model (VDM) is shown in **Figure 2.4**, with the elastic photon scattering off the proton via an exchange of a pomeron [21].

The coupling of a photon to a bound $q\bar{q}$ pair would add an extra component to the partonic structure of the photon. In the perturbative QCD (pQCD) model, the scattering $(\gamma^* p \rightarrow Vp)$, the sequence of events were well separated in time, from the proton rest mass frame. In this model, the photon fluctuates into a $q\bar{q}$ state that scatters on the proton target. The $q\bar{q}$ pair would later turn into a vector meson.

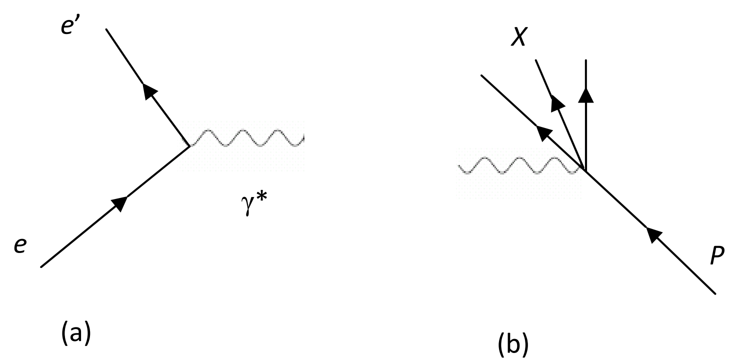

Figure 2.3 Electron-proton scattering at small Q^2, with the electron as a source of virtual photon γ* flux interacting with incoming proton resulting in hadronisation of particle *X* in $\gamma^* p$ interaction

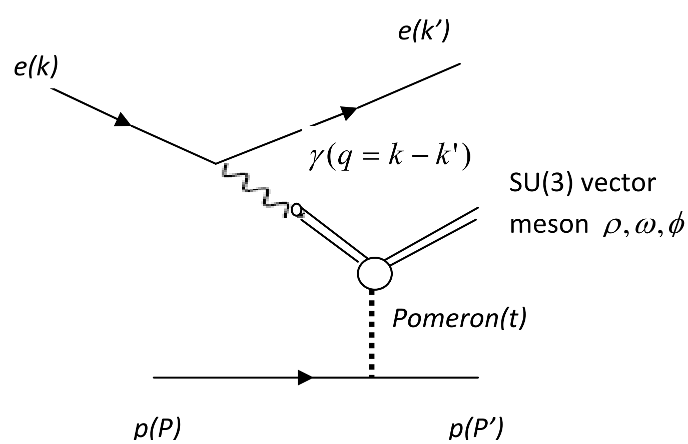

Figure 2.4 Elastic vector meson production through Vector Dominance Model (VDM), with the photon fluctuating into a vector meson, which then scatters elastically from proton via the exchange of a pomeron [21]

In **Figure 2.5**, the exclusive vector meson production through pertubative QCD model is shown, with the proton fluctuating into a $q\bar{q}$ pair with the formation of vector meson via an exchange of two gluons [21]. In the pQCD model, the production of vector meson in the presence of hard scale μ was used to probe the gluonic content of the proton.

The mixture of $u\bar{u}, d\bar{d}, s\bar{s}$ mass-eigenstates with ϕ having the most pure $s\bar{s}$ state with only a very small admixture of $u\bar{u}, d\bar{d}$ states [31].

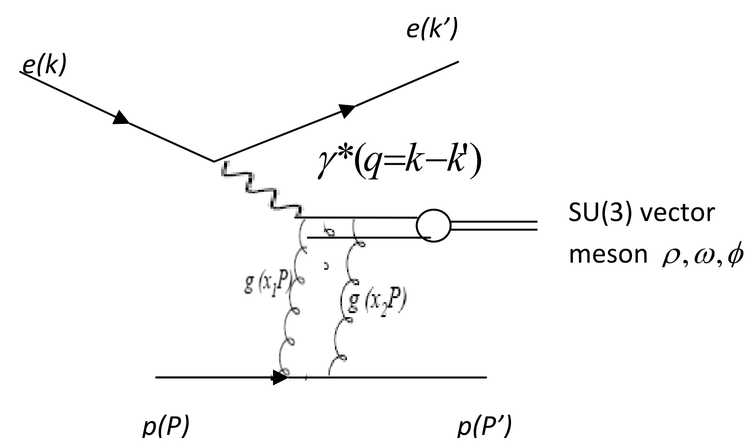

Figure 2.5 In the exclusive vector meson production based on the perturbative QCD model, the photon fluctuates into a $q\bar{q}$ pair, which then scatters off the proton to produce vector meson, via the exchange of two gluons (with momentum fraction x_1, x_2) [21]

In VDM model, when photon fluctuates into a $q\bar{q}$ pair during its interaction with a proton, the gluons transform in the adjoint representation of SU(3) during linear transformation of hadron. In case of ϕ production, the hadronisation of strange quarks could occur through the QPM model of the hard scattering of a virtual photon on the proton strange sea ($\gamma^* s \rightarrow s$), versus the first order QCD Compton (QCDC) reaction ($\gamma^* s \rightarrow sg$) or the Boson Gluon Fusion (BGF) process ($\gamma^* g \rightarrow s\bar{s}$) that depends on the gluon density in the proton [32].

For light vector mesons $q\bar{q}$ pair combinations, there are nine possible combinations of the light u, d and s quarks that group themselves into a nonette, as given in **Figure 2.6** The multiplets of the vector meson are classified by their strangeness S and isospin I. In the centre of nonette,

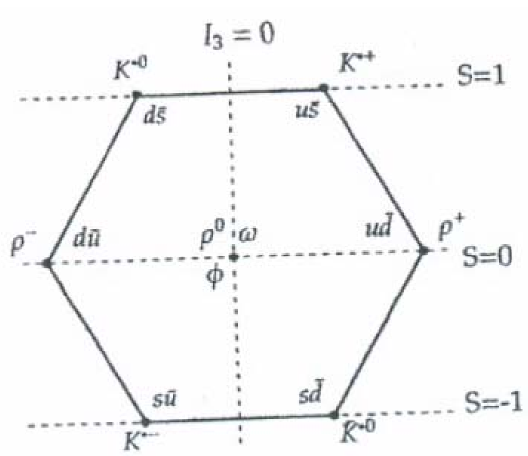

Figure 2.6 SU(3)$_{flavor}$ multiplets of light vector mesons, with various states classified by their strangeness content S and the third component I_s of their isospin [31]

2.7 Color Dipole Moment (CDM)

In QCD cascade model, the partons were treated as independent emitters of gluon. But in Color Dipole Moment (CDM) model, the gluon g emitted from a $q\bar{q}$ pair in an $e^{+}e^{-}$ collision was treated as radiation of color dipole between the quark q and antiquark $\bar{q}$, with consecutive gluon emission from q and $\bar{q}$ treated as two independent qg and $\bar{q}g$ dipoles (see **Figure 2.7)** [49].

The emission phase space in color dipole model was usually plotted as in a $(\ln p_{\perp}, y)$ plane, with $p_{\perp}$ as the transverse momentum and y as the rapidity of the emitted gluon, given by[49],

$$y = \frac{1}{2}\ln\frac{1-x_1}{1-x_3} \qquad (2.5)$$

with $x_i = 2E_i / \sqrt{s_{dip}}$ as the final state energy fraction of the emitting partons in the dipole center-of-mass system s_{dip} and α_s as the effective strong coupling constant between in the incoming and outgoing struck quark.

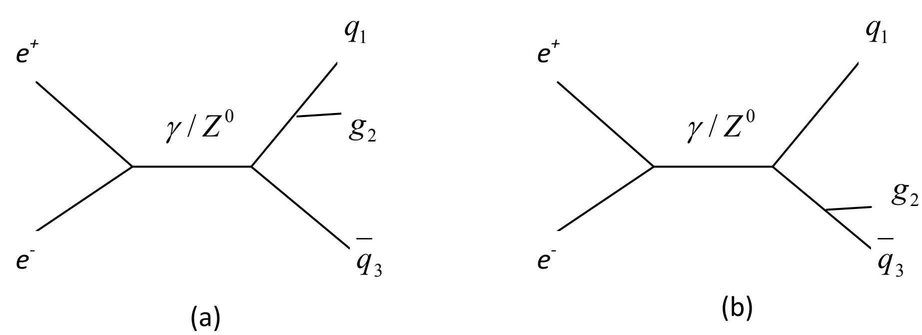

Figure 2.7 Gluon emission g_2 from a $q\bar{q}$ pair in Color Dipole Moment (CDM) model, (a) gluon emission from quark (b) gluon emission from anti-quark [49]

The cross sections of the $q\bar{q}$, qg (or $\bar{q}g$) or gg dipoles were approximated by,

$$d\sigma \propto \alpha_S \frac{dp_\perp^2}{p_\perp^2} dy \tag{2.6}$$

The above approximation as given by CDM was only good when the emissions were strongly ordered i.e. $p_{\perp 1}^2 >> p_{\perp 2}^2 >> p_{\perp 3}^2 >> \; ....$ in the phase space as in **Figure 2.8a**

In CDM, the degree of freedom of the recoil partons during gluon emission was determined by the azimuthal angle ϕ of the emitted gluon and the polar angle θ of the incoming parton..

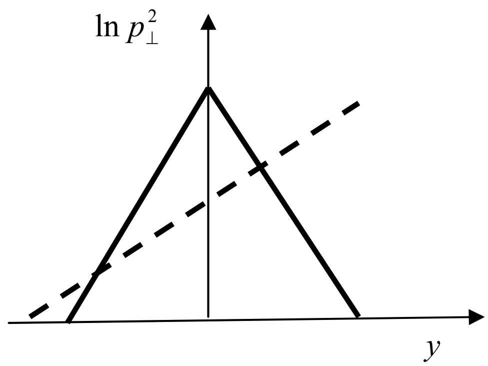

Figure 2.8a Phase space limits for emission of the first gluon (thick lines) and available space for gluon emission (dash lines) in DIS [49]

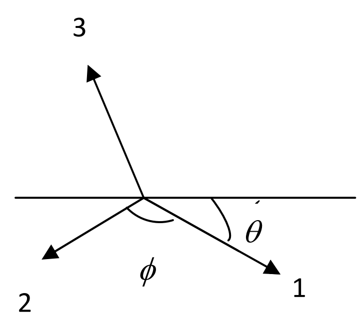

Figure 2.8b Orientation of a dipole after emission**.** azimuthal angle ϕ of the emitted gluon and the polar angle θ of the incoming parton 1

The transverse of recoils should be distributed in such manner that “the disturbance of colour flow in neighboring dipoles is minimized”. In event generator Ariadne, the gluon emitted from the qg dipole always retain its direction while the gg dipole recoiled according to [49],

$$\theta = \frac{x_3^2}{x_1^2 + x_3^3}(\pi - \phi) \tag{2.7}$$

where ϕ is the angle between parton 1 and parton 3. The azimuthal angle ϕ of the emitted gluon is assumed to be evenly distributed between 0 and 2π, with the polar angle θ of the incoming parton as in **Figure 2.8a.**

In case of the Deep Inelastic Scattering (DIS) of the electron on hadrons, CDM assumed that radiation formed between the struck quark and the hadron remnant, with the struck quark treated as point-like while the hadron remnant as extended object. Consequently, only a fraction of small wavelengths $\lambda \propto \frac{1}{p_\perp}$ from extended antenna participating in the emission. The coupling of virtual photon γ^* to a valence quark might produce colour-$\bar{3}$ charge carried by the whole remnant and is treated as simple diquark. The dipole connects to the struck quark with the valence diquark leaving a colour-less meson (with the remaining valence quark and anti-sea-quark). In case of dipole connecting to the anti-sea-quark, a baryon is produced instead. The hadron carries with it a fraction of z of the original proton from the Lund symmetric function.

In the remnant treatment involving “gluonic” object pomeron (such as the production of ϕ meson in Vector Dominance Model (VDM)), the virtual photon γ^* cannot couple directly to a “gluonic” object pomeron . Here, the remnant is treated as extended gluon connecting both the quark and the corresponding antiquark with one dipole each . The “pomeron-induced” part of the total parton density function $f_q^p(x, Q^2)$ is given by a simple convolution [49],

$$f_q^{p(IP)}(x,Q^2) = \int dt \int dz \int dx_{IP} \; f_{IP}^{p}(x_{IP},t) \; f_q^{IP}(z,Q^2) \; \delta(zx_{IP} - x) \qquad (2.8)$$

with $f_{IP}^{p}(x_{IP},t)$ as the pomeron flux taking a fraction x_{IP} of the proton momentum transfer t with density of quarks $f_q^{IP}(z,Q^2)$ within the pomeron and, z as the fraction of the original proton momentum in the Lund symmetric fragmentation function.

In this case, the pomeron remnant is the antipartner of the struck quark. For the struck quark be part of the pomeron, the probability $f_q^{p(IP)}(x,Q^2)/f_q^{P}(X,Q^2) < 1$ will result in the dipole between the struck quark and the pomeron remnant.

2.8 Kinematic Variables of the Electron-Proton Collision

In an electron-proton collision, a proton *p* beam accelerated in the positive z-axis, at a momentum P, collided with an electron *e* beam at momentum *k* in the opposite direction of the proton beam. After the collision, the electron is scattered with momentum k' at angle θ_e from its original direction (as in **Figure 2.9**), while the proton is scattered with momentum P' from its initial direction. During a deep inelastic scattering (DIS), a fraction of electron momentum maybe lost through a photon (real γ or virtual γ*) though the exchange of a boson.

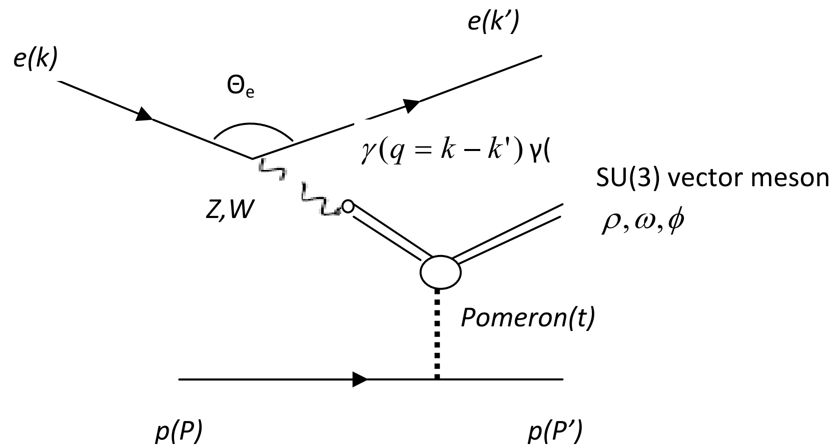

Figure 2.9 Kinematic variables in the electron-proton collision, with P, k , q as the momentum of proton *p*, electron *e*, and photon *γ* respectively (generated in the process). The production of ϕ meson via a promeron exchange an virtual photon γ in the vector meson model (VDM)

Assuming that the mass of the incoming and scattered electron were negligible, the centre-of-mass energy *s*, of the e-p system is given by,

$$s = (k + P)^2 \approx 4E_e E_p \qquad (2.9)$$

where E_e (=30GeV) and E_p (=920GeV) are energies of incoming electron and proton respectively. The centre-of-mass W^2, for the intermediate boson-proton is given by,

$$W^2 = (q + P)^2 \qquad (2.10)$$

During the interaction, the photon, whether real γ or virtual γ*, gains momentum from the incoming electron through the following relation,

$$Q^2 = -q^2 = -(k - k')^2 \qquad (2.11)$$

with *k* as the four-momentum of initial electron and *k'* as the four-momentum of electron emerges from the scattering.

In deep inelastic scattering (DIS) where the struck quark from the proton carries with it a fraction *x* of the incoming proton's momentum as given by the Bjorken scaling *x*,

$$x = \frac{Q^2}{2p.q} \tag{2.12}$$

In the rest frame of the proton, the inelasticity *y* (i.e. fraction of the electron's energy transferred to the proton) reduces to:

$$y = \frac{E_e - E_{e'}}{E_e} = 1 - \frac{E_{e'}}{E_e} \tag{2.13}$$

with E_e as energy of the incoming electron and $E_{e'}$ as energy of the outgoing leptons

2.9 Kinematic Variables of Hadrons in the Final States

During the electron-proton collision in the ZEUS detector at HERA, some particles that emerged from the interaction might travel the whole length of ZEUS detector to deposit their island of energies as in the electromagnetic calorimeter (EMC) and hadronic calorimeters (HAC) of the ZEUS detector. Such particles were identified as either charged through their association with tracks that were formed in their trajectories in the ZEUS detector, or as neutrals if there was no track associated with the energy islands.

Assuming that an object-*i* in the final state states that travels to the calorimeter of the ZEUS detector has a four-momentum $p_i = (p_{xi}, p_{yi}, p_{xi}, E_i)$, that makes a polar angle θ_i with the z-axis and azimuthal angle ϕ_i in the x-y plane is shown in **Figure 2.10**.

Using the momentum in the x-y-z direction, the polar angle θ_i of particle-i is given by,

$$\cos\theta_i = p_{xi}^2 / (p_{xi}^2 + p_{yi}^2 + p_{zi}^2) \tag{2.14}$$

with its azimuthal angle $\cos\phi_i$ of object-i, as

$$\cos\phi_i = p_{xi}^2 / (p_{xi}^2 + p_{yi}^2) \tag{2.15}$$

In the ZEUS detector, the momentum of uncharged tracks of object-i was calculated by assuming object-i as pions. Thus, we could use the equation (2.6) above to calculate the direction of uncharged object-i without from the ZUFOS entry data in the Orange ntuple blocks of the ZEUS analysis code.

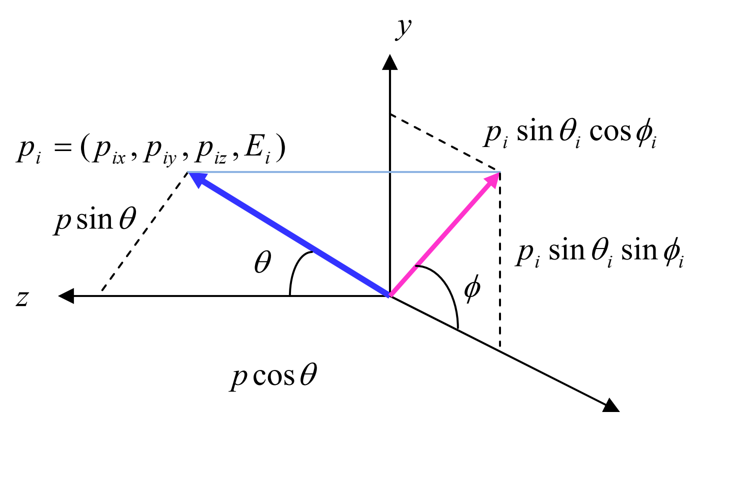

Figure 2.10 Direction of a particle with four-momentum $p_i = (p_{xi}, p_{yi}, p_{xi}, E_i)$, with z-axis positive in the direction of the proton beam, x-axis positive in the HERA ring direction.

In the calorimeter of the ZEUS detector, the energy clusters of cells in the calorimeter that was not associated with any track and not part of the calorimeter objects considered as neutral energy, with the neutral object energy E related to its momentum by $E^2 = p^2$ [27].

In this case, virtual photon produced by the incoming electron in electron-proton collision contributed totally to the formation of neutral particle when the virtual photon, as given in **Equation (2.11)**, strike a quark from a proton through a pomeron as given in Vector Dominance Model (VDM) model. In this limit, the particle is travelling close to the speed of light, the approximation of the mass of the particle is nearly zero or $m \to 0$.

Assuming that the particle-i with energy E_i travel towards the calorimeter of the ZEUS detector and deposits its energy along the trajectory. As the momentum p_i of object-i is proportional to its E_i, therefore the components of p_i in x, y and z-axis would also be proportional to its energy E_i, the transverse momentum is reduced to [6]:

$$p_T = \sqrt{p_x^2 + p_y^2} = \sqrt{(E_T \cos\phi)^2 + (E_T \sin\phi)^2} \approx E_T = E\sin\theta \qquad (2.16)$$

Thus the kinematic variables of the object-i traveling close to the speed of light and exist in the final states, in terms of the momentum components (p_{xi}, p_{yi}, p_{zi}) and energy E_i, could be written as the following [15],

(i) The momentum p_i of object-i, in terms of energy deposit E_i, polar angle θ_i and azimuthal angle $\cos\phi_i$ of object-i [15] ,

$$p_{xi} = E_i \sin\theta_i \cos\phi_i \qquad (2.17)$$

$$p_{yi} = E_i \sin\theta_i \sin\phi_i \qquad (2.18)$$

$$p_{zi} = E_i \cos\theta_i \quad (2.19)$$

$$p_i = \sqrt{(E_i \sin\theta_i \cos\phi_i)^2 + (E_i \cos\theta_i \sin\phi_i)^2 + (E_i \cos\theta_i)^2} \quad (2.20)$$

(ii) Transverse momentum of object-i;

$$p_{Ti}^2 = p_{xi}^2 + p_{yi}^2 = E_i(\sin\theta_i \cos\phi_i)^2 + (E_i \sin\theta_i \sin\phi_i)^2 \quad (2.21)$$

(iii) Invariant mass of object-i,

The invariant mass of the hadronic in the final state, from its measured four-momenta, is given by $mass_i = \sqrt{E_i^2 - p_{xi}^2 - p_{yi}^2 - p_{zi}^2}$ [13], Substituting **Equations (2.17), (2.18)** and **(2.19)** into this equation would give the invariant mass of object-i, in terms of is energy, azimutal and polar angles as:

$$mass_i = \sqrt{E_i^2 - (E_i \sin\theta_i \cos\phi_i)^2 - (E_i \sin\theta_i \sin\phi_i)^2 - (E_i \cos\theta_i)^2} \quad (2.22)$$

(iv) $\delta_i = E_i - p_{zi} = E_i(1 - \cos\theta_i)$ (2.23)

(v) Rapidity: $y_i = \frac{1}{2}\ln\left(\frac{E_i + p_{zi}}{E_i - p_{zi}}\right) = \frac{1}{2}\ln\left(\frac{E_i + E_i \cos\theta_i}{E_i - E_i \cos\theta_i}\right)$ (2.27)

(vi) Pseudorapidity: $\eta_i = -\ln\left(\tan\frac{\theta_i}{2}\right)$ (2.28)

(vii) Ratio p_{Ti} / p_i from energy

$$\frac{p_{Ti}}{p_i} = \sqrt{\frac{(E_i \sin\theta_i \cos\phi_i)^2 + (E_i \sin\theta_i \sin\phi_i)^2}{(E_i \sin\theta_i \cos\phi_i)^2 + (E_i \sin\theta_i \sin\phi_i)^2 + (E_i \cos\theta_i)^2}} \quad (2.29)$$

In the study on neutral and charge current (NCC) cross section at high Q^2 at HERA, the summed the momentum as given in **Equations (2.17), (2.18)** and **(2.19)** was used for all cells in the calorimeter of the ZEUS detector [17]. The **Equations (2.17), (2.18) and (2.19)** was also used to calculate the momentum of the scattered positron in the measurement of dijet cross sections with a leading neutron in photoproduction [9] and the four momentum of scattered electron in the measurement of hadron in final state in diffractive DIS tagged with leading proton spectrometer [13].

From the invariant mass equation of object-i, i.e. $m_i^2 = E_i^2 - p_i^2$, the ratio of the four-momenta p_i of object-i to its energy E_i is given by

$$\frac{p_i}{E_i} = \sqrt{1 - \frac{m_i^2}{E_i^2}} \qquad (2:30)$$

2.9.1 Deep Inelastic Scattering (DIS)

In the deep inelastic scattering (DIS) of the electron-proton collision, the kinematics of DIS for particles is as the follows:

The electron method:

$$Q_i^2 = 2E_{ei}E'_{ei}(1+\cos\theta_{ei}) \qquad (2.31)$$

$$y = 1 - \frac{E'_e}{2E_e}(1-\cos\theta_i) \qquad (2.32)$$

$$x = \frac{Q^2}{sy} \qquad (2.33)$$

At relatively low Q^2 ($Q^2 < 100\ GeV^2$), the reconstruction variables using electron methods is recommended as it has better resolution [28].

At relatively low Q^2 ($Q^2 < 100\ GeV^2$), the reconstruction variables using electron methods is recommended as it has better the best resolution [28].

The hadron method/Jacquet-Blondel method:

$$\delta = \sum_{i=1}^{\#hadronss} E_i (1-\cos\theta_i) = E_{had} - p_{z,had} \tag{2.34}$$

$$y_{JB} = \frac{\delta_{had}}{2E_e} \tag{2.35}$$

$$x_{JB} = \frac{Q^2}{s y_{JB}} \tag{2.36}$$

$$W_{JB} = \sqrt{y_{JB}\ s} \tag{2.37}$$

The Jacquet-Blondel method relies entirely on measurements of the hadronic system under study.

The Double Angle Method:

$$\cos\gamma = \frac{p_{T,had}^2 - \delta_{had}^2}{p_{T,had}^2 + \delta_{had}^2} \tag{2.38}$$

$$Q^2 = 4E \frac{\sin\gamma(1+\cos\theta_e)}{\sin\gamma + \sin\theta_e - \sin(\theta_e+\gamma)} \tag{2.39}$$

$$x = \frac{E_e}{E_p} \frac{\sin\gamma + \sin(\theta_e+\gamma)}{\sin\gamma - \sin(\theta_e+\gamma)} \tag{2.40}$$

In Double Angle Method, the angles of scattered positron and hadronic energy flow are used.

2.10 Long Live Neutral Hadrons in Final States

2.10.1 K_L^0 Production

In the deep inelastic scattering of the electron-proton collision, the sea of strange (s) quarks in the proton may result in the production of ϕ meson. In terms of Quark Parton Model (QPM), a hard scattering of virtual photon on a proton consisting of strange sea of quarks through reaction $\gamma^* s \to s$ could result in the hadronisation of the strange quarks to produce ϕ meson. Other source of the strange quarks is the QCD Compton (QCDC) through $\gamma^* s \to s\,g$ in the first order of QCD process, and the Boson Gluon Fusion (BGF) through $\gamma^* s \to s\,\bar{s}$ reaction [28] in the first order of QCD process. In contrast to the QPM and QCDC process, the BGF events are determined by the gluon density in the proton [28].

Thus, the production of ϕ meson (as the source of K_L^0 and K_S^0 through $\phi \to K_L^0 K_S^0$ decay channel) could provide information on the strange quark production through the hard photon scattering on a sea of strange quarks in the proton. The study of $K_L^0 K_S^0$ production has been carried out using e^+e^- annihilation process and the Vector Dominance Model (VDM) to search for excitations of the $\rho(770)$, $\omega(780)$, $\phi(1020)$, where the vector mesons with isospin $I = 0, I = 1$ decayed into a kaon pair [34].

In the DIS of the e-p system, the hadronisation of the strange quarks during hard interaction could produce ϕ-meson. The study on the ϕ-meson production in DIS and its sensitivity to strange sea quarks in the proton has been carried out by [28] in Breit frame where the exchanged virtual boson is virtuality Q was completely space-like, with radiation of the outgoing struck quark and the proton remnant clearly separated.

With the ϕ-meson in nearly a pure $s\bar{s}$ state due to ideal mixing with the ω and the contribution from resonance decay was small, the sensitivity of ϕ-meson cross sections to strange sea of quarks in the proton was expected to be higher than the K^0 $(d\bar{s})$ mesons and Λ (uds) baryons . Thus, the measurements of ϕ-meson with high transverse momentum p_T that minimize contribution from fragmentation, could provide information on strange quark production by hard interaction with strange sea of quarks in the proton [28].

Figure 2.11 shows the $\phi \to K_L^0 K_S^0$ decay channel, with K_L^0 and K_S^0 in the opposite direction to preserve the ϕ momentum. In this decay K_L^0 with decay length of 15.33m and mean life of $(5.114 \pm 0.021) \times 10^{-8} s$ [35], any K_L^0 produced would proceed to the hadronic calorimeter of the ZEUS detector, while K_S^0 would decay in the immediately after being produced (with mean life of $(0.8958 \pm 0.0006) \times 10^{-10} s$ and decay length 206842cm) detectable by the central tracking detector (CTD) of the ZEUS detector.

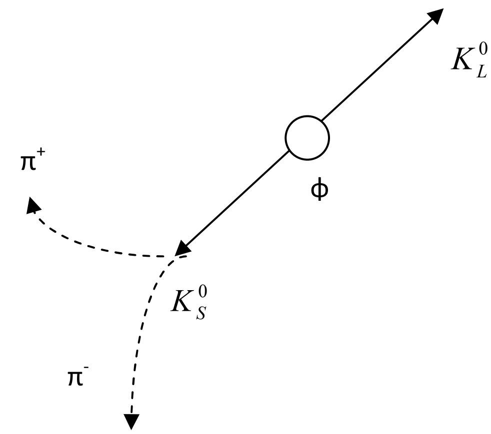

Figure 2.11. An exclusive ϕ decay through $\phi \to K_L^0 K_S^0$. $\phi \to K_L^0 K_S^0$ channel has 34.0% yield, with $K_S^0 \to \pi^+\pi^-$ yield 69.2%

2.10.2 Leading Neutron production at HERA

Neutron and proton are the most common baryon members naturally found in the universe, with proton and neutron as the most common hadrons and are stable with mean life of $> 1.9 \times 10^{29}$ years and 885.7 seconds, respectively.

Neutrons and proton has three quarks each, with proton having two up (u) quarks and one down (d) quark and, neutrons with one up (u) and two down (d) quarks. These quarks are held together in proton and neutron by strong force mediated by gluons. As fermions, the quarks and leptons have (intrinsic angular momentum) spin ½. In the composite particles the quarks combine together to from hadrons with one spin as a whole.

Neutrons and proton as members in baryon family with baryon number B, define as:

$$B=\frac{n_q - n_{\bar{q}}}{3} \qquad (2.41)$$

with n_q as the number of constituent quark and $n_{\bar{q}}$ as the number of constituent antiquarks

The production of leading neutron *n* during the dijet photoproduction events at HERA has been associated to the virtual photon produced during the interaction of proton-electron collision in the following process [37]:

$$e^+ + p \rightarrow e^+ + jet + jet + X + n \qquad (2.42)$$

Leading neutron production has been studied using the Forward Neutron Calorimeter (FNC), located 105.6m downstream the HERA tunnel in the proton direction [38], where the leading neutrons, which carried majority of the energy from the electron-proton collision, moved in straight trajectory as the incoming protons, and was detected at the FNC (Forward Neutron Calorimeter) [38].

Figure 2.12 gives the schematic diagram of resolved photoproduction of dijets in leading neutron mediated by meson exchange, with x_π (x_γ) denotes the fraction of energy exchanged meson (photon) participating the partonic hard scattering, with σ as the hard cross section involved. In case of direct photoproduction and no photon remnant, $x_\gamma = 1$ with the photon behave in point like manner [37].

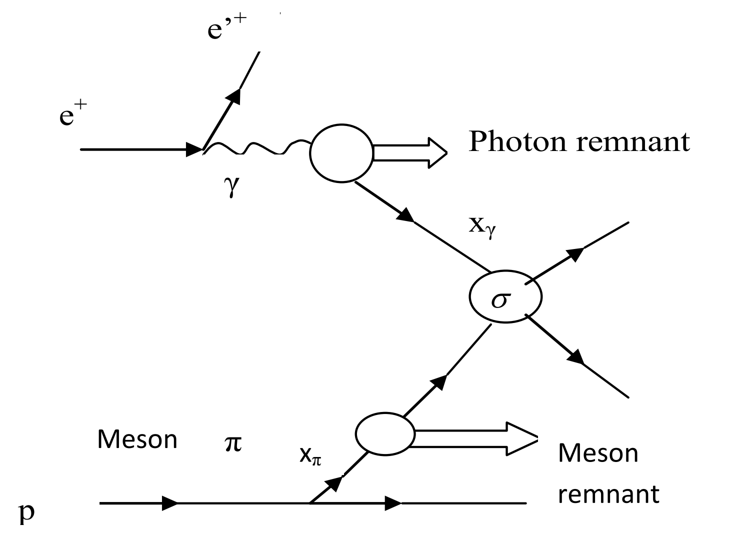

Figure 2.12 Resolved One-Pion exchange diagram[37]

2.10.3 Neutron production through $\Lambda \rightarrow n\pi^o$ channel

The neutral strangeness production study at the ZEUS detector has been carried out using the inclusive production of neutral strange particle to provide insights to the fragmentation process of $\Lambda, \overline{\Lambda}, K_S^0$ in the *ep* collision [7].

While the previous study of $\Lambda \rightarrow p^+\pi^-$ fragmentation (**Figure 2.13a**) was used with ZEUS central tracking detector (CTD), in this thesis, the fragmentation of Λ through the $\Lambda \rightarrow n\pi^0$ channel was used. **Figure 2.13b** gives the schematic diagram of fragmentation of $\Lambda \rightarrow n\pi^0$, where the neutron being produced moves in straight direction through EMC (electromagnetic calorimeter) to HACs (hadronic calorimeter) of the ZEUS detector, and the undetected (i.e.

uncharged tracks) by the CTD. As π^0 is unstable, it decays into two photons moving in the same direction of π^0 and depositing 95% of its energy in the EMC of the ZEUS detector.

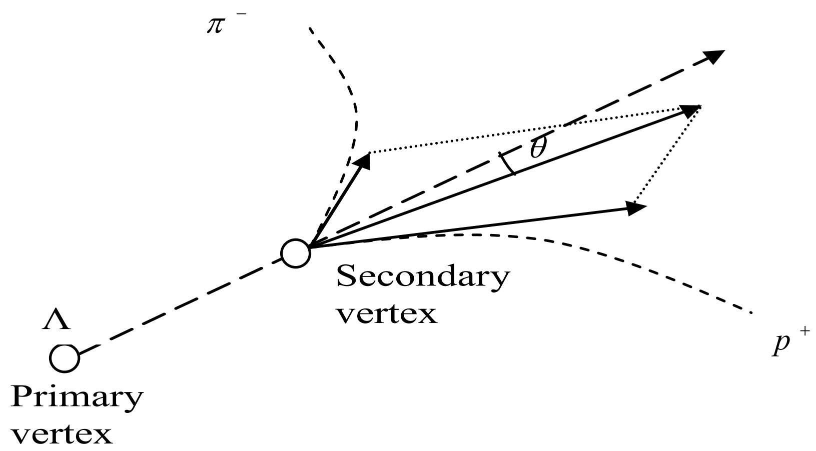

Figure 2.13a An Example of Λ^0 decay through $\Lambda^0 \rightarrow \pi^- p^+$ channel, where the two decay products moved apart in electromagnetic field in CTD., leaving two detectable tracks[7]. The yield is 63.9%.

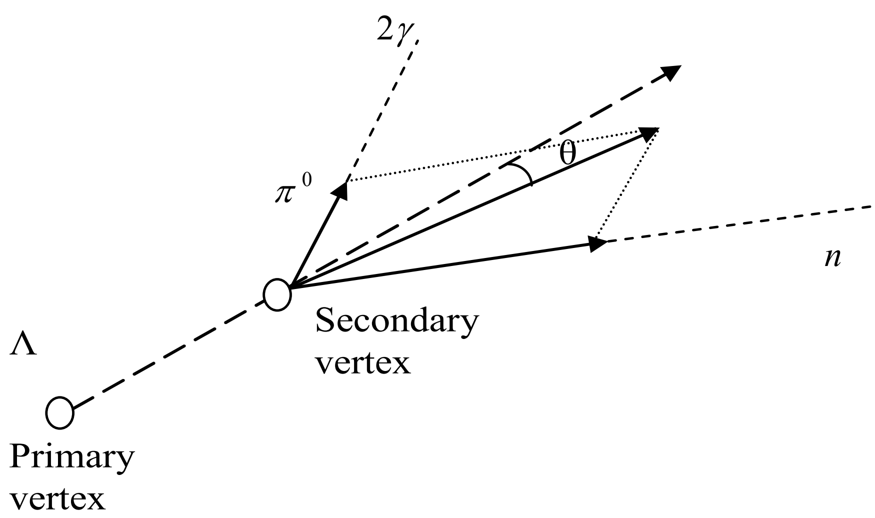

Figure 2.13b An Example of Λ^0 decay through $\Lambda \rightarrow n\pi^0$ channel (35.8% yield) where the two decay products moved along its original trajectories in two undetectable tracks, with $\pi^0 \rightarrow 2\gamma$ (98.8%).

The advantage of using $\Lambda \to n\pi^0$ channel is that the study of CP (Conjugate and Parity) could be carried out using the radial distribution of neutral particles where charges of both mother and decay products were conserved – only the states changes involve i.e. (uds) in Λ to (udd) in n and $(u\bar{d})$ in π^0 .

In this thesis, we attempt to find neutrons in mode $\Lambda \to n\pi^0$ above, using data with uncharged track that form islands in the HAC (hadronic calorimeter) cells of the ZEUS detector, using ZUFOs (Zeus Unidentified Flow Objects) blocks in the ntuples.

2.11 Conservation of Strangeness Number

In 1947, when the process of $\Lambda \to n\pi^0$ was first observed, the fact that Λ has much longer life time (i.e. $10^{-10}s$) than expected ($10^{-23}s$) due large mass and large production cross section.

This observation lead to the term "strangeness conservation" where the baryon Λ preserve the strangeness number S = -1, in such a way that strange quark s must be transformed in a process that can only occur through weak interaction that leads to longer life time.

In case of the ϕ (1020) meson, its nearly pure state of $s\bar{s}$ due to ideal mixing with ω and the contribution of resonance decay to the ϕ meson production is small makes it a good choice for studying the strange sea in the proton. Previous works of on inclusive ϕ (1020) meson production at HERA has been carried out in the virtuality of exchange photon range $10 < Q^2 < 100\,GeV$ using the decay $\phi \to K^+K^-$ channel to study the hard scatterings on an $s\bar{s}$ pair leading to the production of a ϕ meson in the Breit frame to separate the radiation of the outgoing struck quark and the proton remnant [28].

The inclusive production of strange particle $\Lambda, \overline{\Lambda}$ using the $\Lambda \rightarrow p\pi^-$ at high Q^2 in DIS has been carried out at HERA to study the fragmentation in ep collision [7].

In this thesis, the decay of $\Lambda \rightarrow n\pi^0$ involving the strange quark s component in baryon $\Lambda\,(uds)$ and the decay of light unflavored meson ϕ into strange mesons K_S^0 and K_S^0 through decay channel $\phi \rightarrow K_L^0 K_S^0$ will be used to provide additional information on the initial state of state Λ and ϕ during the electron-proton collision in the ZEUS detector by tracking the dynamics of their respective decay products, namely n, π^0 and K_L^0, K_S^0, with n and K_L^0 in their hadronic final states. **Table 2.1** and **Table 2.2** give the properties of $\Lambda \rightarrow n\pi^0$ and $\phi \rightarrow K_L^0 K_S^0$ channel respectively.

Table 2.1 Components of $\Lambda \rightarrow n\pi^0$ channel

Decay scheme	$\Lambda \rightarrow n\pi^0$		
particle	Λ	n	π^0
Quark components	uds	udd	$\frac{\bar{u}u + \bar{d}d}{\sqrt{2}} \approx u\bar{d}$
Strangeness	-1	0	0
$I(J^P)$	$0\left(\frac{1}{2}^+\right)$	$\frac{1}{2}\left(\frac{1}{2}^+\right)$	
$I^G(J^{PC})$			$1^-(0^{-+})$

C : charge conjugation, *P*: Parity, *G*: parity on whole multiplet

Table 2.2. Components of $\phi \to K_L^0 K_S^0$ channel

Decay scheme	$\phi \to K_L^0 K_S^0$		
particle	ϕ	K_L^0	K_S^0
Quark components	$c_1\left(u\bar{u} + d\bar{d}\right) + c_2\left(s\bar{s}\right) \approx s\bar{s}$	$d\bar{s}$	$d\bar{s}$
Strangeness	-1		
$I^G(J^{PC})$	$1^-\left(0^{++}\right)$		
$I(J^P)$		$\frac{1}{2}\left(0^-\right)$	$\frac{1}{2}\left(0^-\right)$

C : charge conjugation, *P*: Parity, *G*: parity on whole multiplet

CHAPTER 3

THE ZEUS EXPERIMENT AT HERA

In experimental high energy physics researches, the particle accelerator provides a high precision instrument for the scientist to conduct research on structure of elementary constituents of matter and the interaction of radiation with matter to understand the basic building blocks that made up the universe. Particle collider such as Hadron-Elektron Ring Anlage (HERA) at Deutsches Electronen Synchrotron (DESY) was one of the pioneers in experimental high energy physics to study the mechanism of hadrons being bound within the nucleus. The ZEUS detector at HERA was constructed as a powerful and versatile detector to measure particles and jets production with energies up to several hundred GeV.

3.1 The HERA Storage Ring

Deutsches Electronen Synchrotron (DESY) was founded in 1959 and part of Helmholz Association, is dedicated to fundamental research in particle physics and the study of synchrotron radiation. DESY at Hamburg campus is home to several particle accelerators, namely DESY accelerator, the linear accelerator (LINAC) the Positron-Elektron Tandem Ring Anlage (PETRA), the Doppel Ring Speicher (DORIS), and the Hadron-Elektron Ring Anlage (HERA) [5].

HERA began its operation in 1992, was the first electron-proton collider in the world to study the scattering interactions between electron of 30 GeV and protons of 920GeV. With circumference 6.3km, HERA two-ring accelerator s located between 10 m and 25 m deep underground (see Figure 3.1).

The protons from the negatively charged hydrogen (H^-) ions were accelerated in phases from 50 MeV in LINAC after which the beam were stripped of the electrons when it passed through a thin foil, to 7.5 GeV in PETRA and accelerated up to 39 GeV before being injected into the HERA ring. In HERA ring, the superconducting dipole magnet with file strength of 4.65 T accelerated the proton further up to 920GeV before it reached the ZEUS detector [5].

The electron and positron for lepton beams at HERA were obtained from the e^+e^- pair production from the bremsstrahlung process of the tungsten sheet. The electron beam were accelerated to 7GeV before being fed into PETRA II, and finally being accelerated up to 27.5GeV by the 0.165 T dipole magnets in the HERA ring before it reached the ZEUS detector.

In the ZEUS detector, the 920GeV proton beam and the 27.5GeV electron beam collided head on to produce leptons, new quarks, hadrons, neutrinos, photons etc., where the data observed during the physics events were recorded by the a an on-line readout control and kept in the DESY data storage system for event reconstruction later.

During the physics experiment, Monte Carlo event generators could be triggered to simulate the physics event simultaneously – these Monte Carlo data would be kept together with the on-line data from the physics experiments in the DESY data storage system for analysis together with the event reconstruction later.

Figure 3.1a HERA and PETRA accelerators aerial view at the DESY campus in Hamburg, HERA is at 10 - 20m underground with circumference 6.3km.

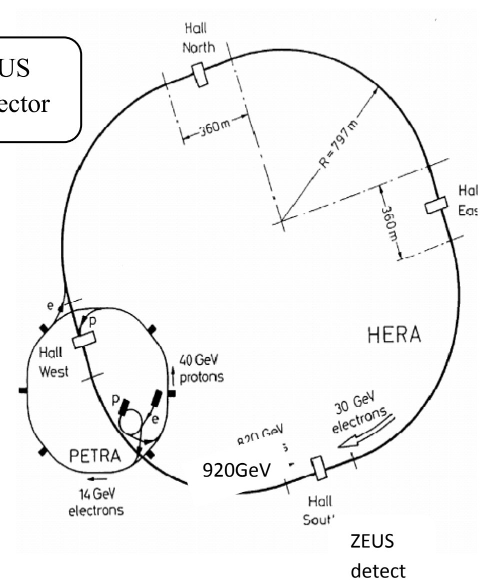

3.1b Schematic diagram of the HERA layout with ZEUS detector at south of HERA

3.2 The ZEUS Detector

The ZEUS detector, located 30 m underground at the southern of HERA experimental hall, was a powerful and versatile detector dedicated to experimental high energy physics, to probe the electron and quark substructure to distance of a few $10^{-18} cm$ and search for new mediators of neutral and charge currents phenomena during the electron-proton beam collision at the centre of the ZEUS detector. In **Figure 3.2**, the longitidunal layout of the ZEUS detector is given [41]. The ZEUS detector comprised of the following components:

(i) vertex detector (VTX)

(ii) central tracking detector (CTD), in the field of a thin magnetic solenoid

(iii) a transition radiation detector (TRD)

(iv) a planar drift chambers (FTD,RTD)

(v) an electromagnetic calorimeter (EMC)

(vi) a hadronic calorimeter (HAC) surrounding full solid angle over the solenoid

(vii) a backing calorimeter (BAC)

(viii) a barrel and rear muon detector (MU)

(ix) a forward muon spectrometer (FMU)

(x) hadron electron separator (HES)

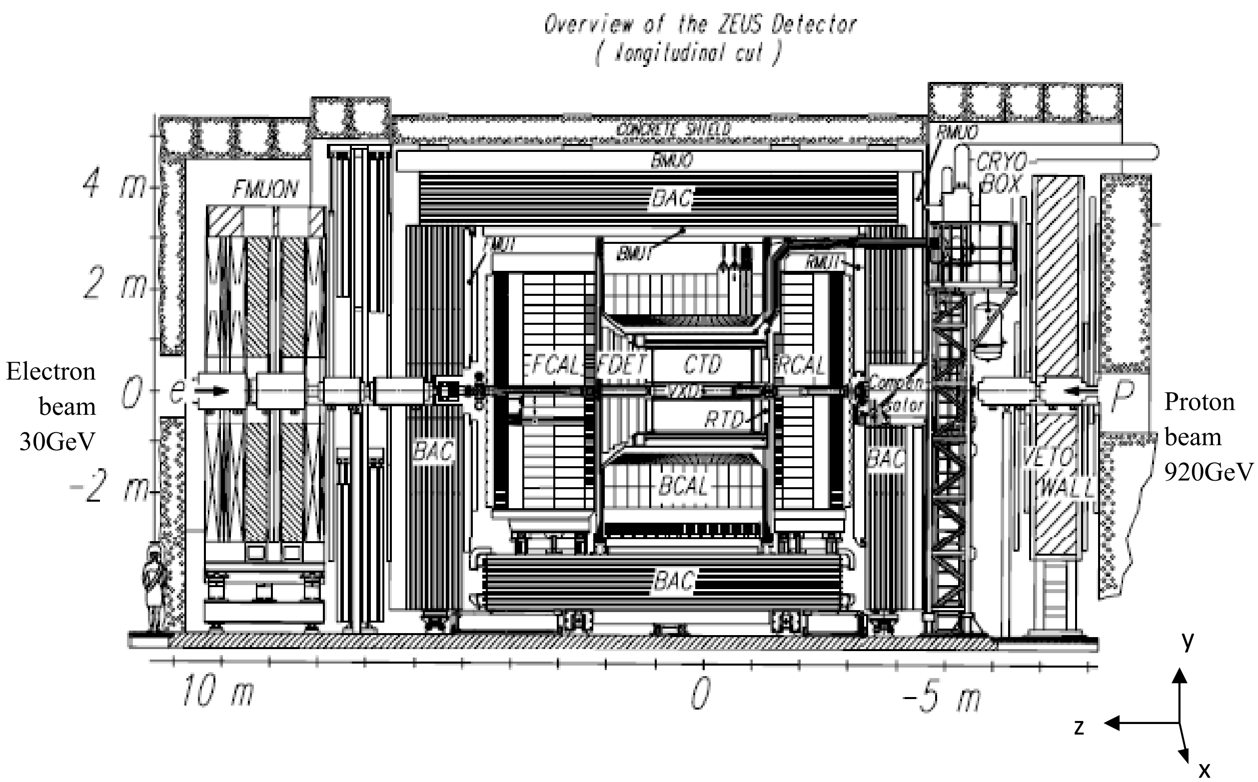

Figure 3.2 Longitudinal cross section view of the Zeus detector [41]. The FCAL, BCAL and the RCAL forms the hadronic calorimeter of the ZEUS detector

3.2.1 The High Resolution Calorimeter

The calorimeter of the ZEUS detector was designed for high energy resolution, uniformity, stability and fast response with the ability to handle up to 10.4MHz of HERA bunch crossing rate. The hadronic energy resolution of the calorimeter was $\sigma(E)/E = 0.35/\sqrt{E} \oplus 2\%$ E in GeV, ($\oplus$ stands for addition in quadrature), while the electromagnetic energy resolution was $\sigma(E)/E = 0.18/\sqrt{E} \oplus 1\%$ [41]. The three main regions of the detector were the forward (FCAL), the barrel (BCAL) and the rear (RCAL). Each region was subdivided into small modules and consist of towers segmented into two parts i.e. the inner parts that constitutes electromagnetic section

(EMC) that detect electromagnetic showers, while the outer parts constitutes the hadronic section (HAC) that detects the hadronic showers. **Figure 3.3** shows the schematic of one such module in the ZEUS detector.

3.2.2 The Uranium-Scintilllator

Throughout the modules in calorimeter, thousands of uranium-scintilllator (SCSN-38) plates were sandwiched together to provide signals to the photomultiplier tube (see **Figure 3.3**). The SCSN-38 scintillator, as active material that contained large fraction of hydrogen atoms, produced the signals by interacting with the slow neutrons from the hadronic shower. The wavelength shifter WLS (Y-7 in PMMA) shifted the wavelength of light emitted by scintillator into visible light before being transmitted to the photomultiplier tube (PMT) as signal from the hadrons as it deposited its energy in the CAL.

Uranium, as passive material, produced slow neutrons through fission reaction that helped in compensating losses in the hadronic shower. It also acts as absorber of electromagnetic particle generated in the electromagnetic part of the hadronic shower, thus enhancing the compensation mechanism [42].

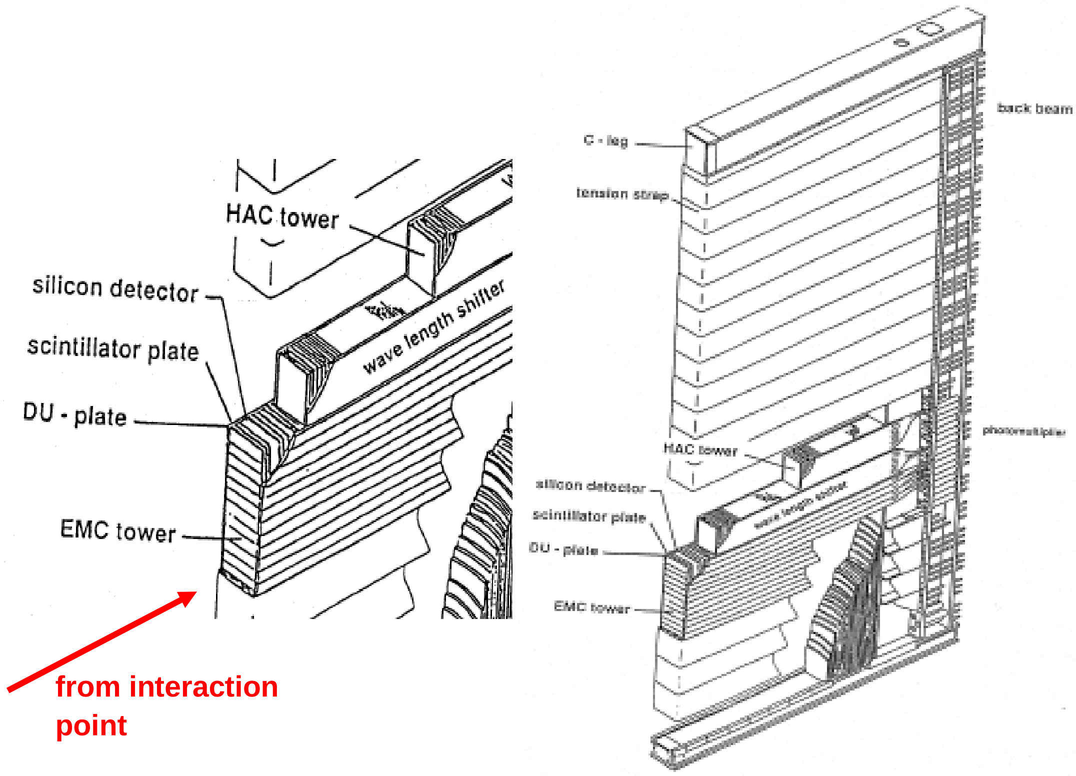

(a) (b)

Figure 3.3 (a) Structure of a tower in a module of a Forward Calorimeter (FCAL) showing the uranium-scintillator sandwich; (b) Side view of a FCAL module . The uranium as passive material produced slow neutron to compensate losses of hadronic shower, while act as absorber to electromagnetic particles. The active scintillator SCSN-38 interacts with slow neutrons from hadronic shower to produce signals for photomultiplier tube (PMT) via the wavelength shifter (WLS) [42][43]

3.2.3 Calorimeter Layout

Figure 3.2 shows the calorimeter which consist of forward hadronic calorimeter (FCAL) and forward electromagnetic calorimeter (FEMC) at the front-end of the calorimeter, the barrel calorimeter (BCAL) and the barrel electromagnetic calorimeter (BEMC) surrounding the middle part of the calorimeter, and the rear calorimeter (RCAL) and rear electromagnetic calorimeter (REMC) at the rear-end, with properties as given in

Table 3.3. BCAL and FHAC comprised of two layers BHAC1 and BHAC2, FHAC1 and FHAC2 respectively, while RHAC consist of only one layer.

During the electron-proton collision, the particles during the interaction would either travel from the point of interaction right to the outer layer of the detector. The particles of electromagnetic radiation such as photons and electrons, traveled from the interaction point at the centre of the detector hitting the superlayers in the central tracking detector (CTD) to the electromagnetic calorimeters BEMC, FEMC and REMC and deposited 95% of its energy there. The hadrons, on the other hand, would deposit 30% of its energy at the electromagnetic calorimeters [3], and continue their paths to the hadronic calorimeters BHACs, FHACs and RHAC.

These particles moved through the uranium-scintilllator sandwich to provide optical signals to the photomultiplier tubes and then to the readout control of the ZEUS detector. **Figure 3.4** shows the showering pattern of the electromagnetic, hadrons and muon showers with the muons having highest penetration depth. Halomuons produced during the proton beam injection into the ZEUS detector, moved in straight path from the rear to the forward calorimeter without losing much of their energies.

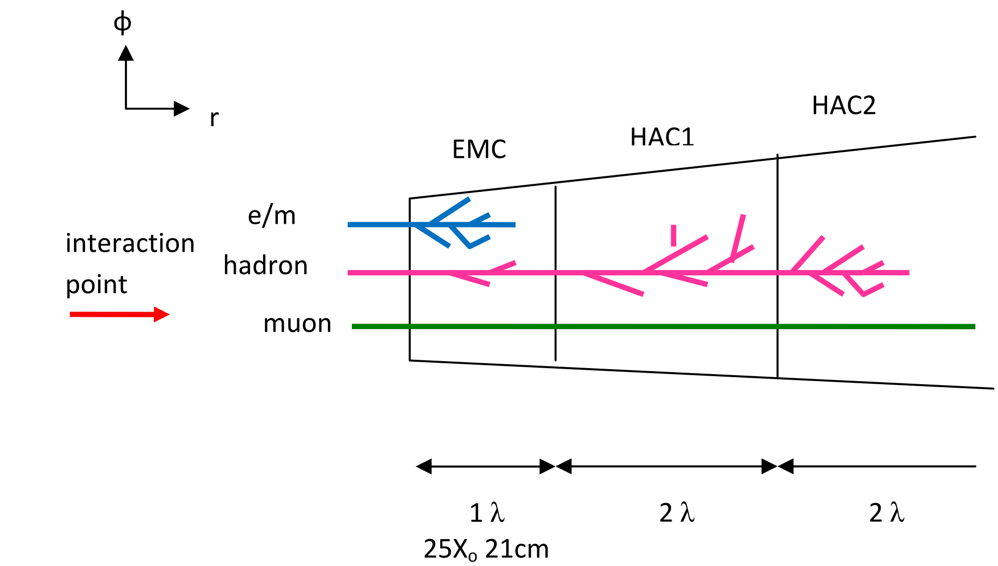

Figure 3.4 Diagram of BCAL tower, with EMC cells backed 2 HAC cells (BCAL towers were projective in η and θ). The hadron particles, electromagnetic (e/m) particles and mouns shower differently in the calorimeter

Table 3.1 Properties of ZEUS CAL listed by section

	FCAL	BCAL	RCAL
Angular coverage (θ)	2.2^0 to 39.9^0	36.7^0 to 129.1^0	128.1^0 to 176.3^0
Angular coverage (η)	101 to 3.95	-0.74 to 1.10	-3.90 to - 0.72
Number of modules	24	32	24
Towers/Modules	11 to 23	16	11 to 23
Number of cells	2172	2592	1668
Depth (m)	1.5	1.07	0.84
Depth (λ)	7.1	5.1	4.0
Depth (X_0)	181.0	129.0	103.0
EMC Front Face Dimension (cm)	5 x 20	5 x 20	10 x 20

3.2.4 ZEUS Tracking Detector

In the ZEUS detector, the trajectory of charge particles such as $\pi^{\pm}, \mu^{\pm}, e^{\pm}, p$ were tracked by the ZEUS tracking detector that comprised of Central Tracking Detector (CTD) and the vertex detector (VTX). In **Figure 3.2,** the CTD is located at the centre ZEUS detector surrounding the vertex detector (VTX).

With active volume 202.4cm between endplates and radial coverage between *r*=19.0cm(innermost) and *r* =78.5cm(outermost), the inner volume of the CTD was lined with 9 superlayers – each superlayers consist of a matrix of 3905 sense wire referred to as cells. When a charge particle passed through the superlayers and hitting the sense wires, the drift distance were digitized. Charge particles produced during the electron-proton-collision and hitting the sense wire inside the CTD would be deflected from its origin.

With an axial magnetic field of 1.8T and radial force distribution along the coil axis of the magnetic field in the CTD of $\int_{-120}^{130} F_r dz = 661\, tons$ supplied by superconducting solenoid between the CTD and barrel calorimeter, the charged particles were deflected for momentum measurements. **Figure 3.5** gives the helix of a CTD hit, where ϕ is the outbound tangent angle in XY plane and, θ as the angle of dip with regard to the XY plane, with the reconstructed momentum as [46],

$$(p_x, p_y, p_z) = (p\cos\phi\sin\theta, p\sin\phi\sin\theta, p\cos\theta) \qquad (3.1)$$

Inside the coil, the magnetic field is approximately parallel to the Z-axis. At any point of a track's trajectory, the path is approximately as an axial helix.

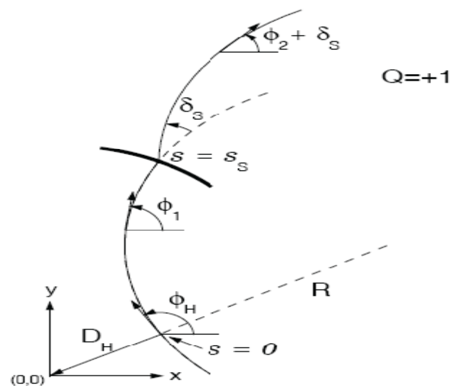

Figure 3.5 A helix in XY plane, where ϕ is the outbound tangent angle in XY plane in the CTD [46]

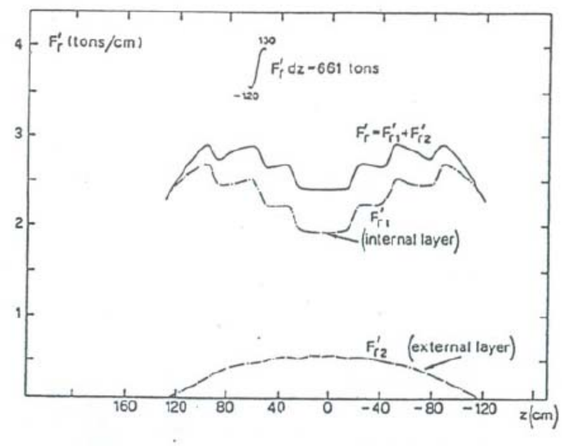

Figure 3.6 Radial force distribution along the coil axis of the magnetic field in central tracking detector (CTD) [41]

Table 3.2 Centre radius of superlayers in the CTD of ZEUS detector [1]

Superlayer	Centre radius of cell (cm)
1	20.97
3	35.00
5	48.73
7	62.74
9	76.54

Figure 3.7 CTD layout of the ZEUS detector [1]

3.2.5 Hadron Electron Separator (HES)

In the ZEUS detector, the Hadron Electron Separator (HES) was used to differentiate electromagnetic showers (electrons) from hadronic showers, to provide the researchers with complimentary data of the electron-proton collision, especially on the electrons from the charm quark decay and to differentiate it from photon showers from electron-proton collision.

Located at the inner front of part of the front and rear calorimeter **(Figure 3.8),** the silicon pad detector on HES recorded the energy deposited by the electron as it passed through the detector. As each the dimension of cell on the pad silicon smaller (3cm x 3cm) than the cell on the calorimeter (20cm x 20cm) the resolution of the electron signal from HES was more refined than the calorimeter. **Figure 3.9** shows the arrays of cells in the calorimeter with silicon pads mounted across the calorimeter.

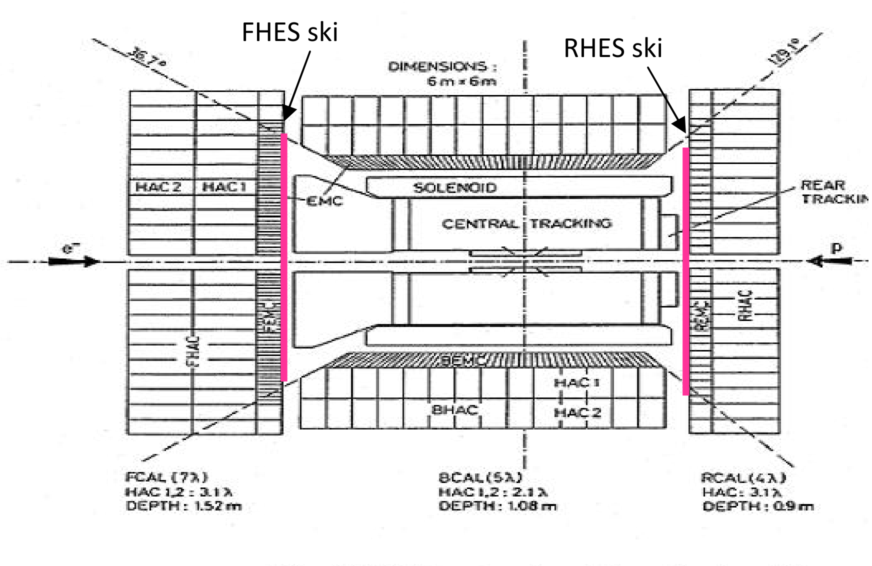

Figure 3.8 Front and rear Hadron Electron Separator (HES) FHES and RHES respectively, in front of calorimeter in the ZEUS detector

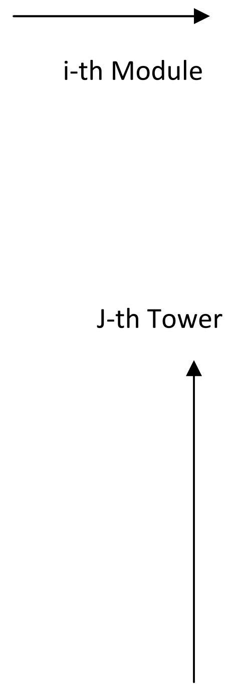

Figure 3.9a The arrays 23 modules and 23 towers calorimeter in the ZEUS detector. Each cell (i, j) in the calorimeter in the calorimeter comprised of i-th module, j-th tower. The figure also shows 3 skis of the HES superimpose in front of the EMC [45]

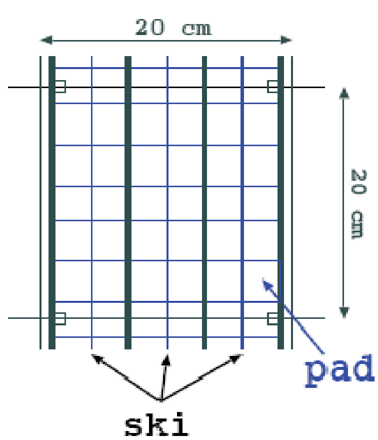

Figure 3.9b Silicon pad (3cmx3cm) mounted on skis, map to one calorimeter cells [45]

3.3 Calorimeter Tracking and ZUFOS

In the calorimeter of the ZEUS detector, the particles originated from the electron-proton collision traveled the across the detector to the calorimeter to deposit its energy in the calorimeter. The energy deposits by hadrons in the final states (whether charge or neutral) and the electromagnetic showers, were recorded by each cells in the calorimeter. **Figure 3.10** shows the trajectory of neutral and charge particles arriving at the calorimeter in the ZEUS detector and depositing energy in the calorimeter cells.

In tracking the particles passing through the calorimeter, each cell of the calorimeter containing energy deposits were clusters to form cone islands, resulting in three dimensional objects known as ZEUS Unidentified Flow Objects (ZUFOs).

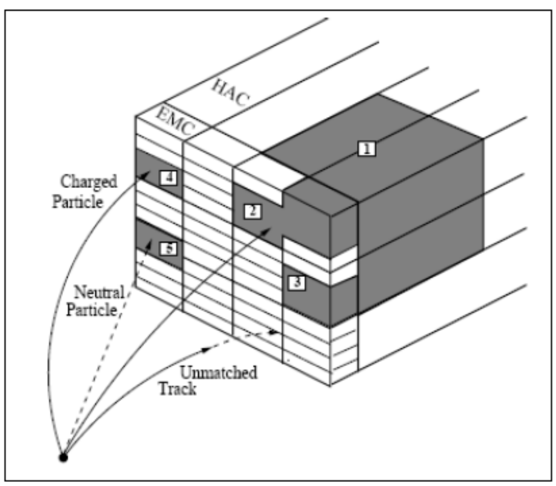

Figure 3.10 Neutral ZUFOs move in straight trajectory from the interaction point through the EMC (electromagnetic calorimeter) to HACs (hadronic calorimeters) in the ZEUS detector, forming islands of energy deposits in the calorimeter. Neighboring cells were clustered to form cone clusters and matched to tracks [2].

These ZUFOs tracks were fitted to the primary vertex. Good tracks were selected if the distance of closest approach (DCA) between extrapolated track from inner surface of calorimeter to the associated island was less than 20cm, or DCA was less than the maximum radius from the plane perpendicular to a ray drawn from the vertex to the island [2].

The energy of charged ZUFOs was determined from the four-momenta by assuming the particle as a pion. The neutral energy of ZUFOs was selected if it was not associated with any track. In this thesis, the ZUFOs were selected as potential candidates for long-lived neutral hadrons in the final states.

3.4 Monte Carlo Event Simulation

To compare the experimental results against theoretical model, the on-line ZEUS detector was equipped with Monte Carlo simulations. **Figure 3.11** gives the flow diagram of the simulation in the ZEUS detector that was being run concurrent to the physics event during electron proton collision.

In the Monte Carlo simulation environment for ZEUS, MOZART (Monte Carlo for ZEUS Analysis, Reconstruction and Trigger), which used the GEANT package, to simulate passage of particles passing the geometry and materials in the ZEUS detector. After MOZART, the event was processed by CZAR (Complete ZGANA Analysis Routine) that simulated ZEUS on-line trigger components based on test beam parameters [5].

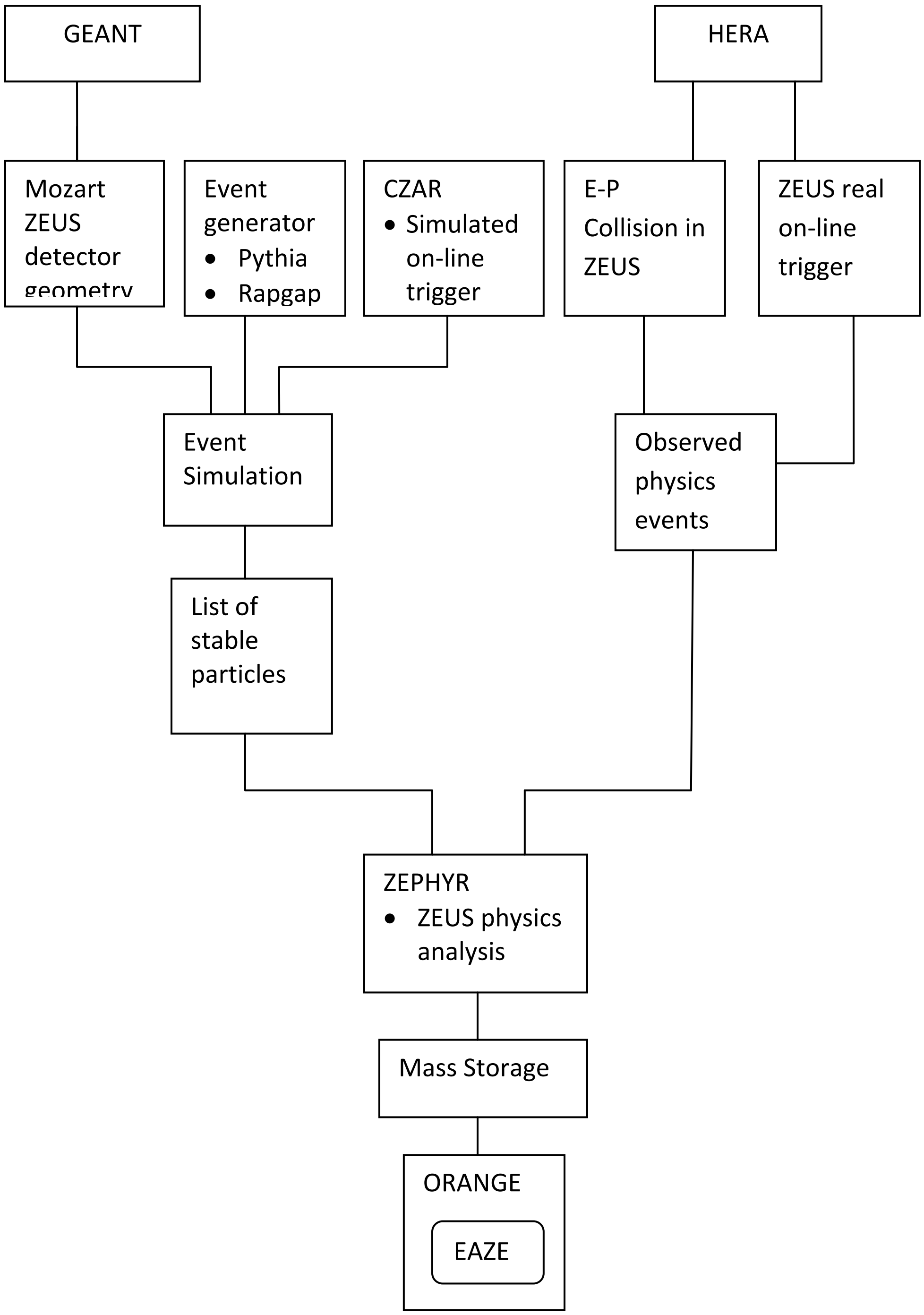

Figure 3.11 Flow diagram of event analysis in the ZEUS detector. Simulated and actual events were run concurrent and compared to extract correction factor from pQCD calculation.

Event generator such as Pythia, Rapgap, Ariadne, Djanggoh were used to provide sets of outgoing particles produced in the interaction between two incoming particles in the electron-proton collision. During real time operation of the ZEUS detector, the global trigger system of HERA provided inputs to the ZEUS detector that accepted 96ns of HERA clock for its synchronized data taking events.

The actual events from the electron-proton collisions and the simulated events were then passed through ZEUS Physics Reconstruction (ZEPHYR) which applied reconstruction code and calibration constants to the events. The raw data were then stored in tabulated forms on ZEUS Adamo table, and kept on mass storage tape for off-line data analysis, available through EAZE (Easy Analysis of ZEUS Events) program integrated in the Orange (Overlying Routine for Analysis Ntuple Generation) package.

3.4.1 Event Generators

The objective of event generators is to use computers to generate events with the same average behavior and the same fluctuation as real data, as detailed as could be observed by a perfect detector by 'factoring' full problems into a reasonably accurate components, with objects branching into two which daughters were free to branch themselves. Monte Carlo technique was used to select all relevant variables based on probability distribution in the final events [48].

The complexity of high energy physics process that based on the level of interactions between fundamental objects i.e. quarks, leptons and gauge bosons , using 'skeleton' process $e^+e^- \to Z^0 \to q\overline{q}$ that branched into subprocesses $e \to e\gamma$ or $q \to qg$, could be treated as 'parton showers' where one initial parton may branched into a whole bunch of partons in the final states, coupling constant α_s that determined the momentum transfer of scale in the parton showering process.

In case of quark and gluon, the structure of incoming hadrons and the hidronisation process, where colored partons (quark and gluons) transformed themselves into colorless hadrons, photons and leptons, fragmentations and decays might take place. These subprocesses were based on specific models such as Lund string model or Color Dipole Moment (CDM).

3.4.1.1 Pythia

In Pythia, the hard process of $e^+e^- \to \gamma^* / Z^0 \to q\overline{q}$, with virtual photon γ^* from of the mass shell, the final state quark *q* might be *u*, *d*, *s*, *b* or *t*, with the flavor picked at random according to the relative couplings evaluated at the hadronic centre of mass (c.m.) energy [48].

In the tunneling picture of the Lund string model, the suppression of heavy-quark production to a ratio $u : d : s : c \approx 1 : 1 : 0.3 : 10^{-11}$ implied that charm and heavier quarks were not expected to be produced in soft fragmentation, but in perturbative parton-shower branching $g \to q\overline{q}$.

When quark-antiquark $q\overline{q}$ pair from two adjacent string moved apart to form a meson, notably a pseudoscalar or vector meson, a quantitative ratio of 1:3 from counting the number of spin states was expected, with the color flow not always well-defined – an algorithm was need to choose between the two.

In the fragmentation process, a large fraction of unstable particles produced decayed into observable stable ones, assuming that the decay products were distributed to phase space with no dynamics involved, where branching ratios and decay modes in normal decay treatment were used.

In baryons production, diquark in antitriplet state behaved as an ordinary antiquark, such that a string could break either by quark-antiquark or antidiquark-diquark pair production (which was not well represented).

3.4.1.2 Ariadne

In simulating the QCD cascade, Ariadne uses the Color Dipole Moment (CDM) to generate particles in e^+e^- and lepton-hadron experiments using the coherence effects in the gluon bremsstrahlung for radiation between two color dipoles as described in **Section 2.7** of **Chapter 2**.

As one of the “Lund family Monte Carlo programmes”, Ariadne only generates the QCD cascade process and is commonly interfaced with other programmes such as PYTHIA, JETSET and LEPTO that handle hard interactions, hidronisation and particle decays.

In approximating the CDM interactions during a $q\bar{q}$ splitting, ordering of transverse momentum $p_\perp$ in the phase space was applied i.e. $p_{\perp 1} > p_{\perp 2} > p_{\perp 3} > .p_{\perp i} > ...$ where *i*=1,2, 3 … refers to the first, second, third dipole originally generated from the first $q\bar{q}$ pair. In case of qg dipole splitting, the gluon always retain its original directing when the color flow in the neighboring dipoles is minimized while the gg dipole is distributed as given by **Equation (2.7)** in **Chapter 2** of this thesis.

CHAPTER 4

READOUT CONTROL AND HALOMUONS

4.1 CAL Readout control (ROC) of the ZEUS Detector

The readout control of the calorimeter of ZEUS detector was extensive and fragmented in design. A Field Programmable Gate Array (FPGA) version of the readout control will give advantage over the old design as it will be single-board and compact, and easier to improve in the future. The FPGA-based readout control for the calorimeter of the ZEUS detector was developed on an Altera Cyclone with Verilog as the hardware description language and with Quartus II as the tool for software testing and simulation. The old circuit diagrams of the readout control modules were used to form basic building blocks of the readout control. This chapter will discuss how the system was developed and simulated for lab-scale testing before being downloaded onto the FPGA hardware for implementation.

4.1.1 The Readout Controlling Modules

In the high energy physics experiment at HERA (Hadron-Electron Ring Accelerator), the proton beam with 920 GeV energy collided with an electron/positron beam (at 30GeV). As a result of the collision, quarks interactions within the accelerated protons and incoming electron/positron were observed and recorded by ZEUS detector, synchronized by the HERA clock at 96 ns or 10MHz. The read-out system controlling the data-taking of the calorimeter part of the detector consists of five analogue modules i.e. table, pipeline, buffer, format and generator modules, with more than 140 input and output signals interconnected to each other. **Figure 4.1** shows the schematic diagram of the calorimeter readout control of the ZEUS detector.

4.1.1.1 The Functions

In this project the analogue circuit diagrams, as well as the block diagram of the table, pipeline, buffer and format modules were used as bass to form the building blocks of a Field-Programmable Gate Array (FPGA) -based readout control, using Verilog as the hardware description language.

The readout electronics were ‘data driven’, i.e. the operation of the components was completely determined by the context provided by the data themselves [52]. The table module gave preset controlling data to the readout system; the pipeline selected which particular cell out of 96 samples [53], to trigger; the buffer keep interim data storage from the pipeline; and the format set the timing for the digitization of the output.

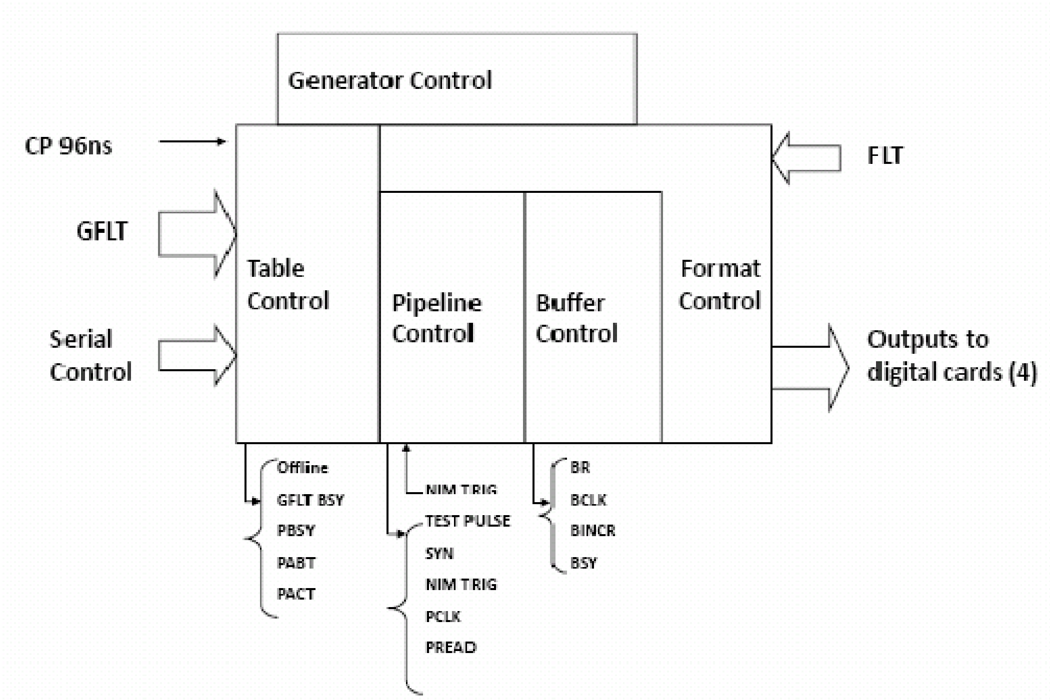

Figure 4.1. Schematic diagram of the calorimeter (CAL) read-out control of ZEUS detector with 96ns HERA clock for synchronization. See **Table 4.1** for parameters definition

4.1.2 FPGA programming

The table module accepts 8-bit serial data from the universal computer interface card i.e. from table, format, pipeline, generator for its RAM (random access memory) data. The controller bits in the table module were synchronized with the 10MHz serial clock. Here, the readout control system was first isolated by giving flag 0, before each subsequent byte pushed the prior byte onto the next register in the chain [52]. Once set, the readout control was put on-line again, where the signals from GFLT (Global First Level Trigger) would determine the controlling sequence of the readout control. In the table module, an FPGA 16-bit shift and 8-bit shift register were design with Verilog to accept serial data and serial clock and compare them with the GFLT signals.

In the pipeline module, the signals from table control would determine which data in the 96 samples of the physics events for accept (ACT) or abort (ABT). While the ACT was true, the buffer controller would continue taking the physics data event and forward them to format controller for digital outputs. On receiving the ABT signal form the table module, the pipeline controller would notify the buffer to reject the current data taking.

Figure 4.2 gives the sequence of the readout control development; the table, pipeline, buffer and format modules were integrated into one FPGA-based module with Verilog.

4.1.3 Coding with Verilog

The converting of the modules was carried out based on the logic block diagram of the readout modules. Connecting inputs and outputs from/into each of the modules were indentified. Smaller sub-modules i.e. shift register (8, 16-bits), multiplexers, JK, RS flip-flops, decoder, counter divider etc. were created and combined to form the four controlling i.e. modules table, pipeline, buffer and format, which were later, combined to form the main controlling module.

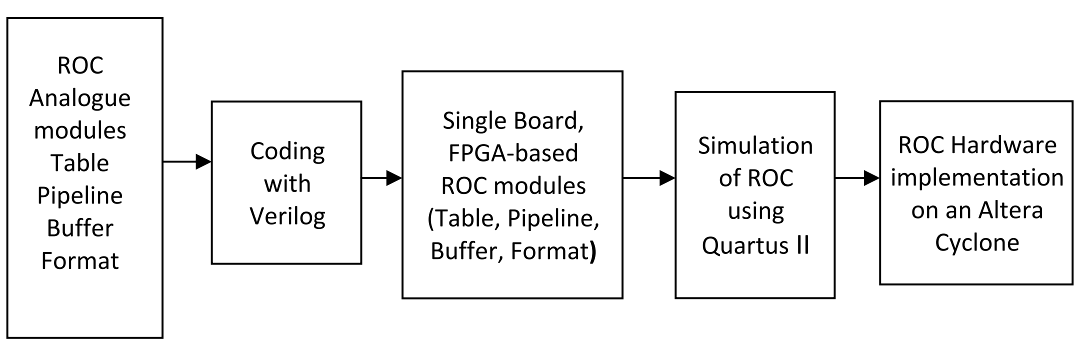

Figure 4.2 . The analogue modules of readout control (ROC) of the ZEUS detector were coded into single board, FPGA-based using Verilog before being simulated on Quartus II.

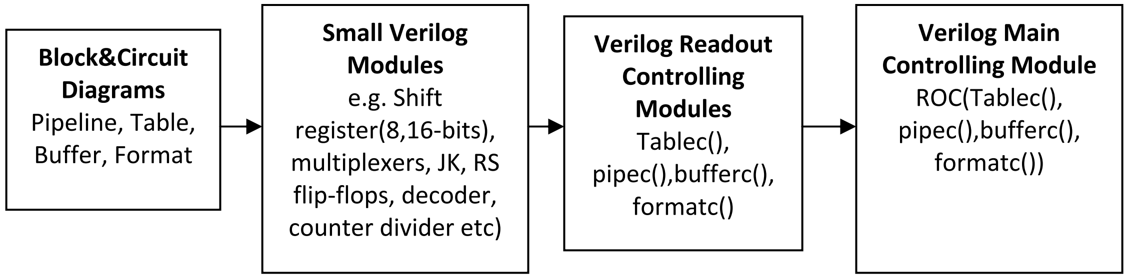

Figure 4.3. Coding sequence of the controlling analog read-out modules using Verilog. Coding were carried our starting with basic blocks, later combined to become the main controlling block

Figure 4.3 gives the coding sequence used in converting the analog table, pipeline, buffer and format modules into the FGGA-based read-out controlling module.

In **Figure 4.4**, two examples of the small FPGA sub-modules used in the ROC are given. Numerous sub-modules were build and combined together to form the controlling modules, which later integrated to form the main read-out control as given in **Figure 4.5**.

Figure 4.5, shows the RTL viewer of the FPGA-based readout control on Quartus II, with full layout of the CAL ROC main modules that integrated the pipeline, buffer, table and format modules to function as a single controlling block.

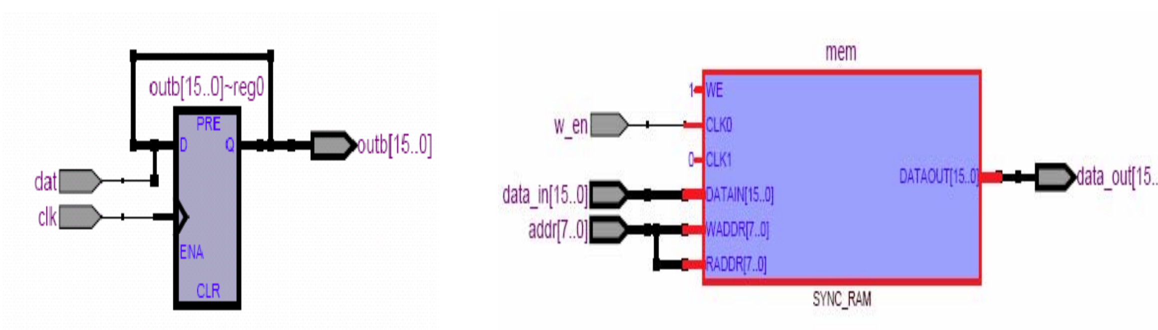

(a) 16-bit non blocking shift register (b) 16-bit RAM

Figure 4.4. Two of the FPGA-based small sub-modules used in the table controlling block.

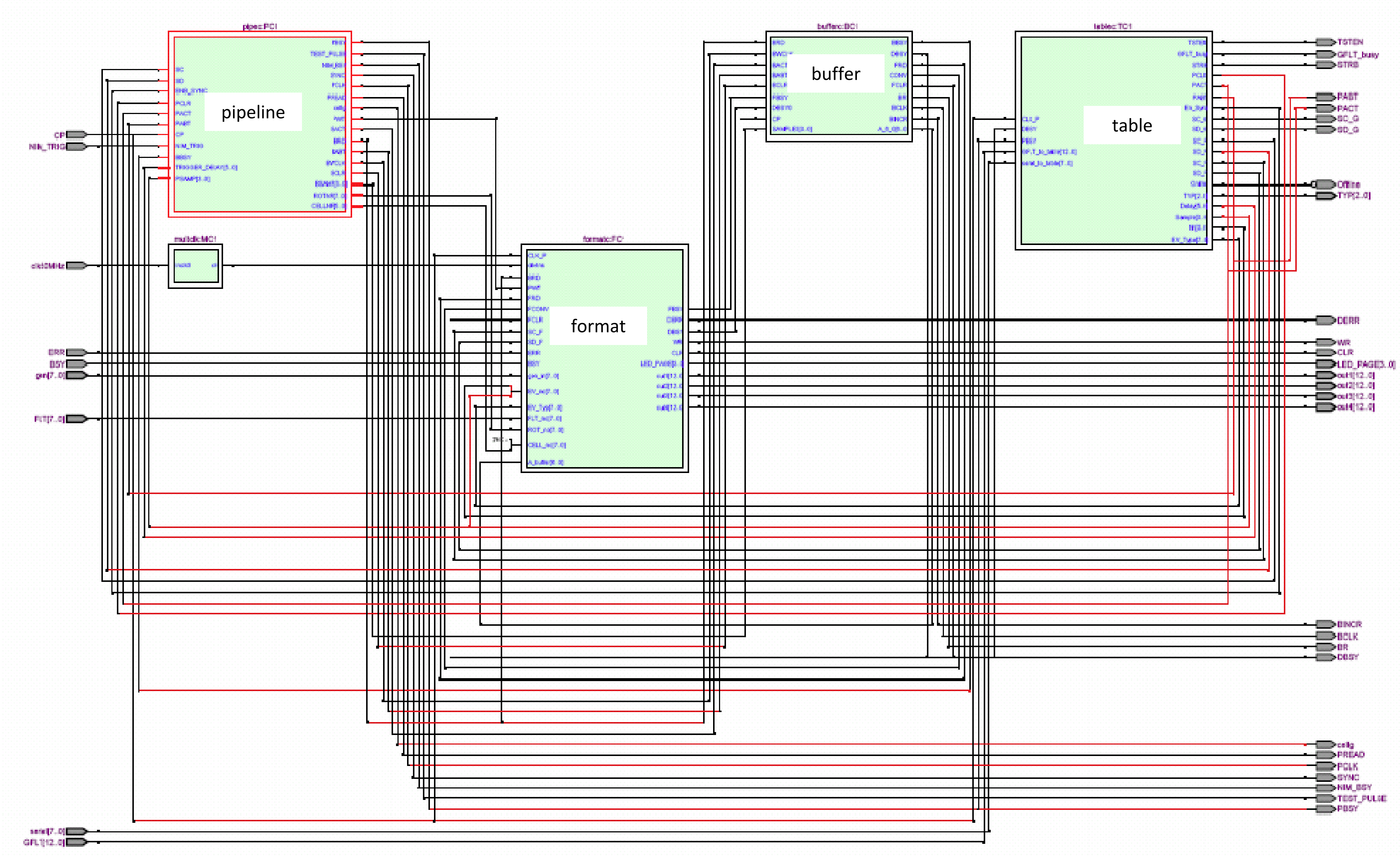

Figure 4.5 Full Quartus II RTL viewer of the FPGA-based readout control (ROC) for the calorimeter (CAL) of the ZEUS detector, showing the four main module i.e. pipeline, format, buffer and table, with inputs on the left and outputs on the right of the diagram.

4.1.4 FPGA Simulation and Results

The integrated FPGA-based modules in Verilog were simulated on Quartus II using the device settings of Altera Cylcone I. **Figure 4.6** shows the part of the vector waveform used in Quartus II for the simulation for serial data input. Each serial data consist of 4 bytes control data given to RAM in table module.

Each bit of the serial data is only counted on negative change of the clock edge, where subsequent byte pushes a prior byte up the 16-bit shift register.

In **Figure 4.7 (a)**, when the pipeline accept data PACT is triggered, the pipeline busy PBSY and the pipeline read PREAD are triggered with PCLK temporarily disabled. Here, the buffer read is flagged 0 and the BCLK is temporarily disabled. **Figure 4.7 (b)**, gives a closer look at the sequence of pipeline and buffer triggers upon abort ABT signal by GFLT. On a negative edge of ABT from GFLT, the pipeline abort PABT triggers and pipeline accept PACT is flagged down to 0. During the abort trigger, the buffer is still flagged 0 and only changes to 1 about 0.07 ms later, resulting in unused data being taken by the buffer instead of rejecting it.

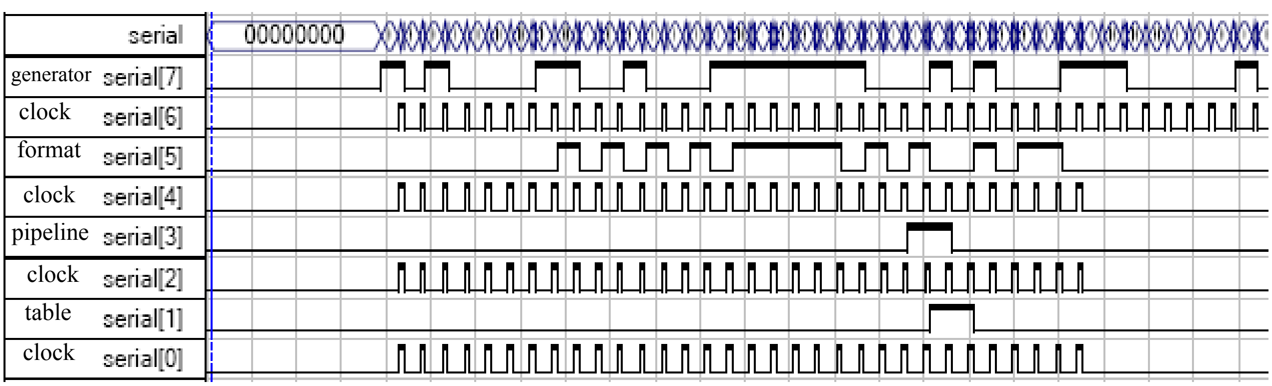

Figure 4.6 Serial data input to the FPGA-based readout control (serial[0] for table control, serial[3] for pipeline, serial[5] for format control, serial[7] for generator control; while serial[0],[2],[4].[6] were serial clock 10MHz)

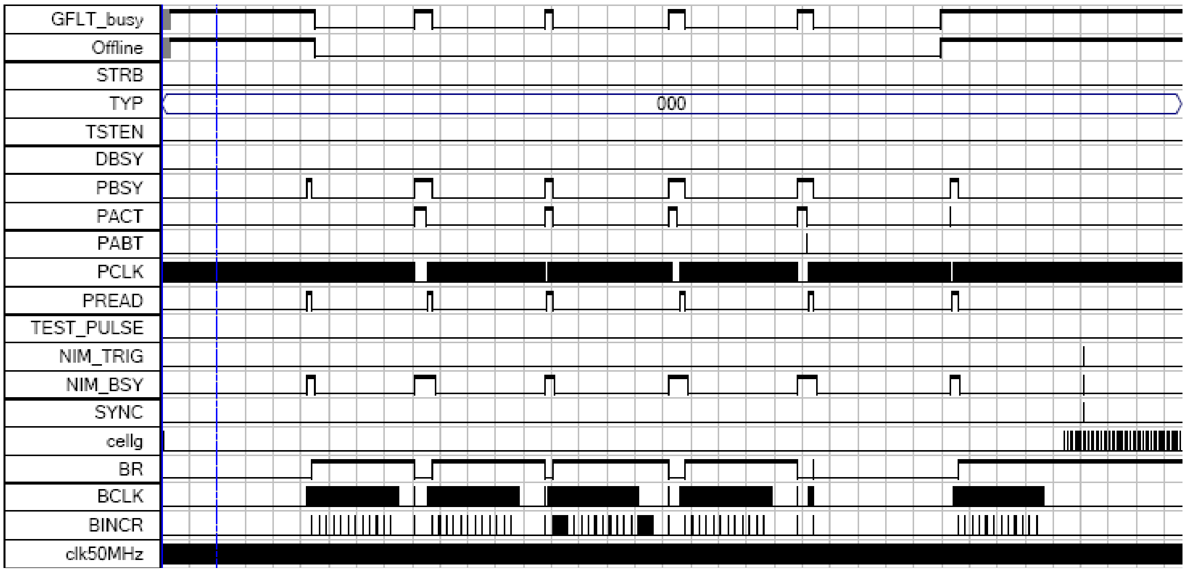

Figure 4.7a Output signals from the FPGA-based readout control

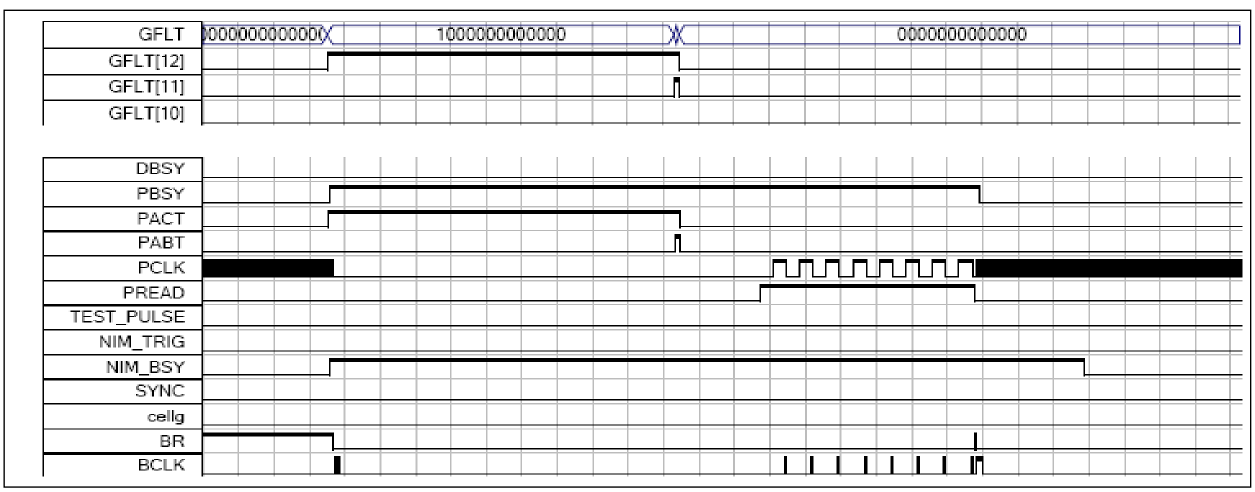

Figure 4.7b A close-up of the FPGA-based readout control showing the abort ABT signal from the pipeline control

Table 4.1 gives some of the output labels used the FPGA-based readout control (ROC) block, with the output waveform as given in **Figure 4.4 (a)** and **(b).**

Table 4.1 Some of the output label from FPGA-based readout control (ROC) as shown in Figure 4.4a and its status

Output label	Output Status	Flag
GFLT_busy	GFLT busy	1
Offline	System is off-line	1
STRB	Strobe signal	0
TYP	Type of event	000
TSTEN	Test mode enable	0
DBSY	Data busy	0
PBSY	Pipeline busy	1
PACT	Pipeline accept data	1
PABT	Pipeline abort data	1
PCLK	Pipeline clock	counter
PREAD	Pipeline read	1
cellg	Number of bunch crossing	1
BR	Buffer read	1

4.1.5 FPGA-based ROC Power consumption

With the design FPGA-based readout control (ROC), simulation on Quartus II resulted in a total number of 123 input/output pins and 7,010 of logic elements used. In **Table 4.2,** the dissipated power calculated for the FPGA-based ROC is given, with a total of 189.61 mW of dissipated power expected for the design ROC. Of the three components, the core static power dissipation contributed the highest at 71% of the total power loss.

Table 4.2 Thermal dissipation of readout control block

Component	Power dissipated	percentage
Core dynamic power dissipation	35.73 mW	19%
Core static power dissipation	134.79 mW	71%
I/O power dissipation	19.09 mW	10%
Total thermal power dissipation	189.61 mW	100%

4.1.6 Hardware Development

The hardware of the readout control was carried out using Proteus software to design the PCB layout using an Altera Cylone I FPGA chip, with a total of 37 chips i.e. 12 of the ECL-to-TTL type, 16 of the TTL-to-ECL type, 7 of the bus driver type and 2 of the for OR gate type.

In **Figure 4.8**, the fabricated printed circuit board (PCB) designed using Proteus software is shown. The figure, the FPGA kit with Altera Cylone I chip is mounted in the middle of the PCB. The board was tested in laboratory using a -5.2V for V_{EE} and initial current I_{EE} supply of 0.5A and, a 5.0V for V_{CC} and initial current I_{CC} of supply 0.63A.

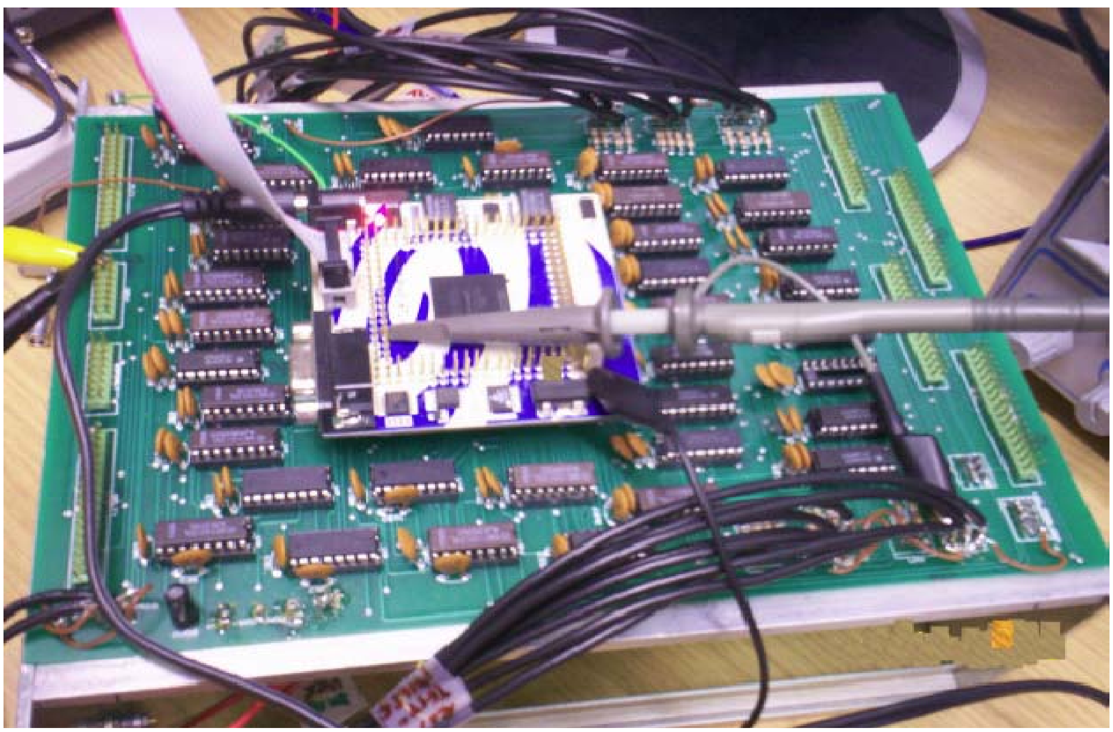

Figure 4.8 A 7inch by 11inch (17.5cm by 27.5cm) PCB designed using Proteus software, with the FPGA Altera Cyclone mounted in the middle and TTL-ECL, ECL-TTL and Quad Bus Driver chips mounted fully. The PCB was tested in laboratory using frequency generator and high current voltage supply

During laboratory test, the chips were mounted one by one on the PCB. Each time the voltage supply V_{EE} and V_{CC} dropped with mounted chips, the current adjusted again until the initial -5.2V and 5.0V respectively.

Figure 4.9 shows the plot of current I_{CC} (A) and I_{EE} (A) versus number of chips of TTL-ECL quad translator type, while **Figure 4.10** shows the same plot for quad bus driver type. In both figures, the currents increases I_{CC} and I_{EE} increased with the number of chips mounted on the PCB, after an initial plateau. For TTL-ECL quad translator type both I_{CC} and I_{EE} show the same trend, but in quad bus driver type chip the currents is higher with I_{CC} dropped lower before increasing.

In quad bus driver type chip, the power dissipation was 575 mW or a total of 6.9 Watt power dissipation produced by 12 chips, thus higher bias current was need than the TTL-ECL quad translator type .

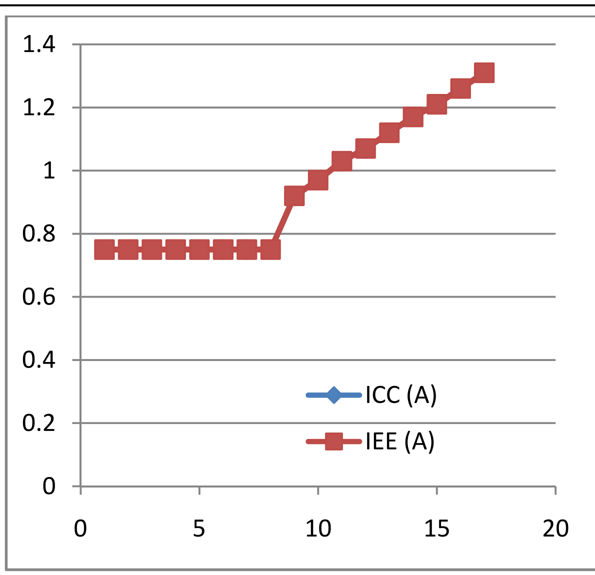

Figure 4.9 Plot of current I_{CC} (A) and I_{EE} (A) versus number of chips of TTL-ECL quad translator type (MC0124) showing the tendency the currents to increase with the number of chips

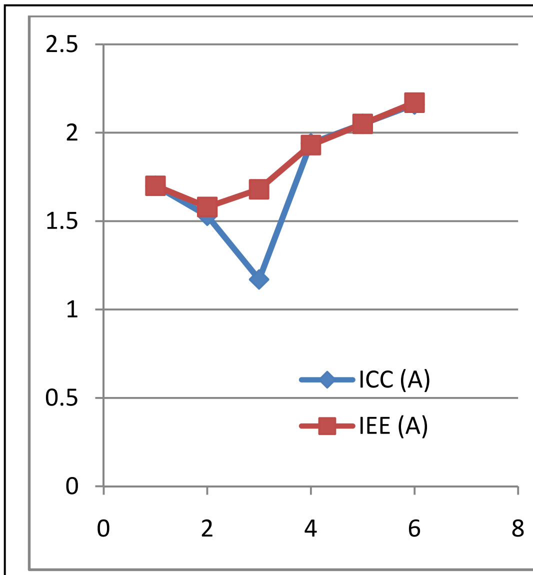

Figure 4.10 Plot of current I_{CC} (A) and I_{EE} (A) versus number of chips of quad bus driver type (MC0192) showing the tendency the currents to increase with the number of chips

In **Figure 4.11**, the plot of power (watt) from bias drain and emitter current and their total power versus number of chips for quad TTL-ECL quad translator driver is given, while **Figure 4.12** gives the same plot for quad bus driver. In both plots, the same trend as in **Figure 4.9** and **Figure 4.10** were observed. In these figures, the linear increase in bias currents and power after a certain number of chips mounted on the PCB indicates that improvisation of the PCB to remove excess heat dissipation is needed.

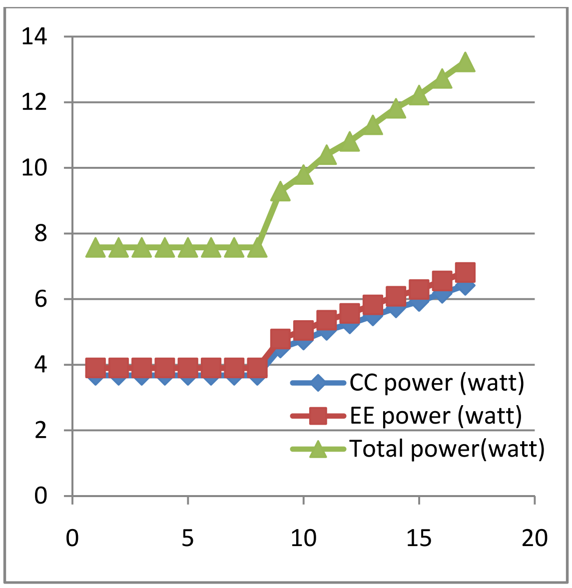

Figure 4.11 Plot of power (watt) from bias drain and emitter current and their total power versus number of chips of quad TTL-ECL quad translator type

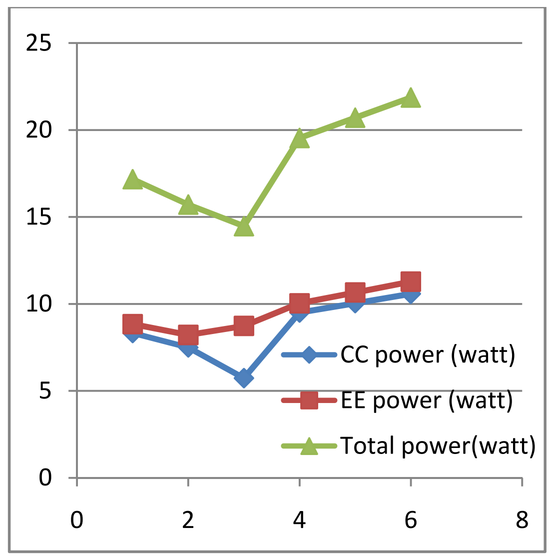

Figure 4.12 Plot of power (watt) from bias drain and emitter current and their total power versus number of chips of quad bus driver type

4.1.7 Summary

In this project, the four controlling modules of the analog readout control of the calorimeter of the ZEUS detector have been integrated into single FPGA-based readout controlling module on a single chip. The integrated FPGA-based module on a single chip besides compact is easier to modify in future. More work would have to be carried out to overcome glitches of the timing sequence of the present readout control

While the power consumption of the FPGA-based readout control on a single chip is quite high, nevertheless we have demonstrated that an FPGA-based readout control for at 96ns synchronized clock is feasible but needs more work to improve its performance especially on power dissipation.

4.2 The Halomuons in the ZEUS detector

In a high energy physics experiment, the cosmic muons and halomuons were normally used to calibrate the energy scale of the detector especially in the lower range. The properties of the halomuons that moves in a straight path i.e. from rear to the front end of the detector makes it a convenient entity to calibrate both ends of the detector in the range of 1GeV and for alignment purposes. The identification of halomuons will help to reduce background contamination during physics experiment, by its elimination from event selection.

In the ZEUS detector, the halomuons were produced upstream of the detector when the proton beam interacted with the rest gas during its acceleration prior to entering the detector, to produce π^+ (mean life of 2.6x10^{-8}s) that later decayed into μ^+. The hard muons μ^+ travelled along with proton beam accelerated towards the RCAL become soft when hitting the veto wall prior to entering the ZEUS detector.

While the transversing halomuons may contribute to the background signals, it is particularly useful for alignment and calibration of the endcap region of the detector [57], as compared with cosmic muons used for the energy calibration of the barrel region of the detector. The halomuons were also used to determine if the energy scale of the calorimeter was correct in absence of dead material in front of the calorimeter, where the measurement of electron and hadron deteriorated substantially [57]. It was also used to study the long-term stability of muon response in each longitudinal section of the FCAL and RCAL, relative to the UNO signal [58]l.

In this section, energies the soft muons traversing the ZEUS detector from RCAL to FCAL were identified using ORANGE and Fortran PAW routines.

4.2.1 Halomuons production upstream of ZEUS detector

Muon is the second heaviest charged lepton with electric charge of ± 1 and is 200 times more massive than electron (mass m =105.658369 $\pm$0.000009 MeV). It has mean life τ = 2.19703 $\pm$0.00004) x10^{-6}s. The halomuons crossed the ZUES detector almost horizontally from RCAL to FCAL, depositing some of its energy in the electromagnetic calorimeter (EMCs) and hadronic calorimeter (HACs) of the detector ZEUS. The halomuons might also gave higher pulse rate to a physics event and contribute to global muons sampling along its trajectory in the detector.

In the ZEUS detector, the veto wall located at 7.5 m upstream of the interaction point, protected the central detector against the particles from the beam halo accompanying the proton bunches [13]. The halomuons from the decayed pions, were absorbed by the iron wall in the Veto Wall. Halomuons which were not absorbed by the iron wall transverse through the RCAL to FCAL.

Figure 4.13 shows the transversing of halomuons from the pion decay and moving along with the proton beam right into the ZEUS detector. Previous study has shown that the mean value of pion momentum spectrum of was about 11 GeV became softer to a mean 8GeV after hitting the shield. Here, the mean muon energy decaying from the pion was about 6GeV. The halomuons mean energy 6 GeV became soft to about 1GeV after hitting the veto wall prior to entering the ZEUS detector [55].

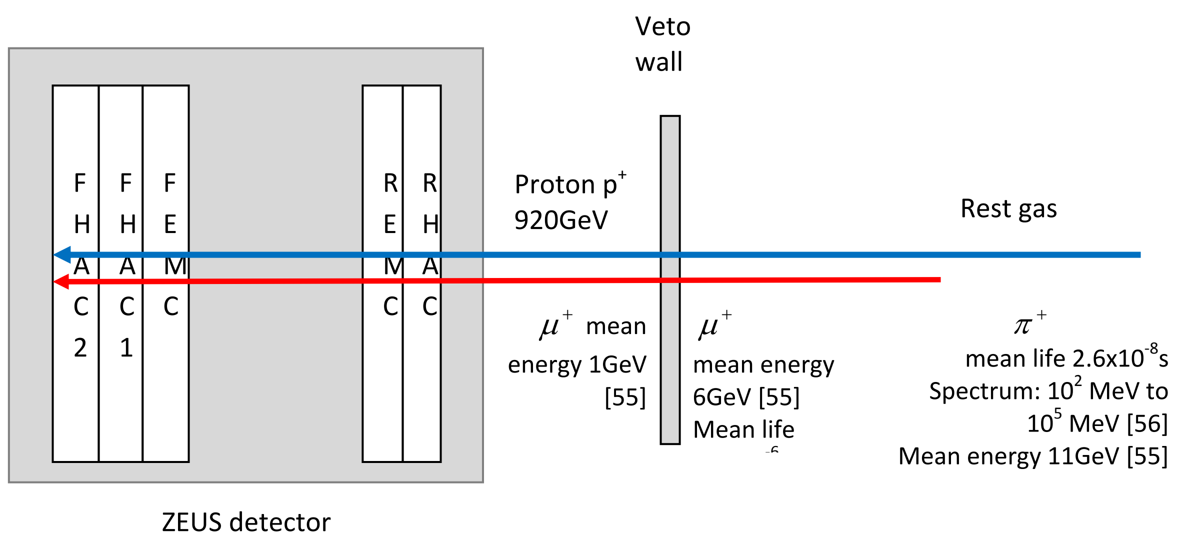

Figure 4.13 Halomuons upstream of the ZEUS detector. π^+ formed during proton beam interaction with rest gas, decayed into μ^+ that were carried by proton beam into the ZEUS detector. The veto wall blocked a fraction of the π^+ from entering the ZEUS detector

4.2.2 The EMCs and HACs in F/RCALs

Figure 3.9 in **Chapter 3** shows the layout of the electromagnetic calorimeter (EMC) and hadronic calorimeter (HAC) in the F/RCAL. In FCAL, there are two HACs i.e. HAC1 and HAC2, and one EMC i.e. FEMC. In RCAL, there is one EMC i.e. REMC and one HAC i.e. RHAC.

In **Figure 3.10a**, the direction of modules and towers of the RCAL as seen from the interaction point, is shown, with 23 modules in the i^{th} direction and 23 towers in the j^{th} direction. At position (12, 12) of RCAL, the beam hole will be visible.

As HERA tunnel was not centred with respect to the main detector, but shifted about +1 m in x-direction and +0.5 m in y-direction, more events in the upper-right corner of F/RCAL than lower left would be expected, where more low energy halomuons would be absorbed by a significantly bigger shielding material in front of the detector [59].

4.2.3 The Algorithm for halomuon analysis

In calorimeter reconstruction program, the identification of particles or group of particles is performed using the particular shower properties of the particle and the segmentation of the calorimeter. Here, the muons are defined as isolated tracks of minimum ionizing energy passing though the full depth of the calorimeter [9]. In case of the halomuons, its transverse path from RCAL to FCAL could be detected from the energy deposits in the HAC1, HAC2 and FEMC cells of the FCAL and the corresponding (origin) halomuons in HAC and RMEC cells of the RCAL.

In selecting the halomuon candidates from the F/R CAL cells, the following conditions were used [60]:

(i) Halomuon trigger bits should be fulfilled

In 2004, trigger logic bit FLT 37 was used to associate potential halomuon candidate's transversing the ZEUS detector. In 2006, the slot 56 is used to store trigger logics for halomuons. This GFLT slot was moved to 17 in 2007 (from run 62595 onwards).

(ii) There should be energy deposits above the background level, in both FCAL and RCAL cells

In selecting potential candidates from Caltru table, a minimum energy of 0.15GeV was required to eliminate background noise.

(iii) Time difference between FCAL and RCAL should be within 5-18 ns from interaction point

For each halomuon candidates reaching the RCAL a time of ~5ns from the interaction would be recorded and on reaching FCAL, a time of ~18ns be recorded. This would ensure that only candidates tranversing from RCAL to FCA would be selected.

(iv) The selected F/RCAL tower should be isolated, i.e

None of the neighboring eight towers should have an energy deposit higher than that of the selected tower. The energy sum of the eight neighboring towers should be less than 20% of the energy of the selected tower [63].

(v) The selected FCAL tower should have one matching tower in RCAL (and vice versa)

If there is an energy deposit in one FEMC and either or both HAC1 and HAC2 cells of the FCAL, then there should also be a (corresponding) energy deposits in REMC and HAC cells of the RCAL

For a given halomuon energy deposit in a FCAL cell, there should be a matching cell in RCAL. A matching of RCAL tower should be isolated i.e. it should have more than 80% of the sum of energy of its surrounding eight neighboring cells. The matched RCAL tower shall be one the nine selected towers with the same tower and module numbers of the selected FCAL tower and its neighboring towers. This cut would throw away halomuon events not parallel to the beam axis [61], [62].

Figure 4.14 shows the scheme for matching the halomuons in FCAL tower to RCAL tower.

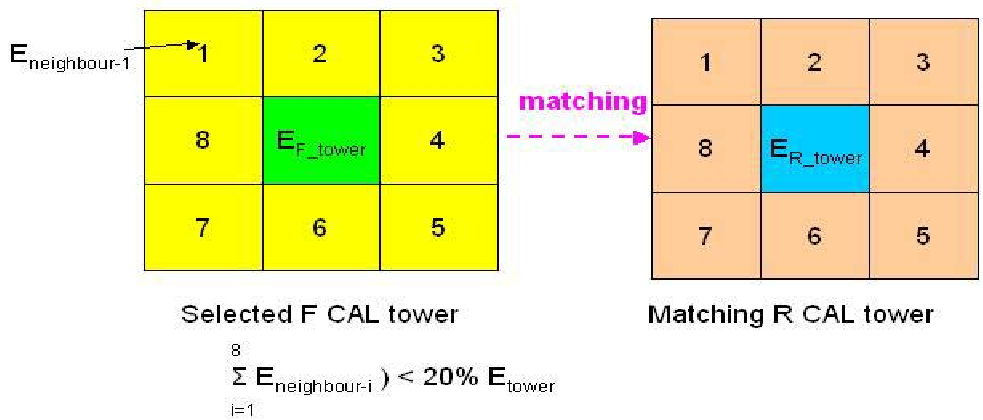

Figure 4.14 Halomuons energy cuts. Selected FCAL/RCAL tower should be isolated with none of the neighbouring towers has higher energy deposit

4.2.4 Results

Figure 4.15 shows the time difference (ns) between FCAL and RCAL for the halomuon candidate's transversing the detector, fulfilling time requirements between 8 and 15 ns from interaction point. These data were from the CALCAL files collected as background to the physics event in the ZUES detector. In this analysis, the magnetic effect of the detector was neglected (but in case of calibration with a precision at a few percent levels [58] the effect might be significant).

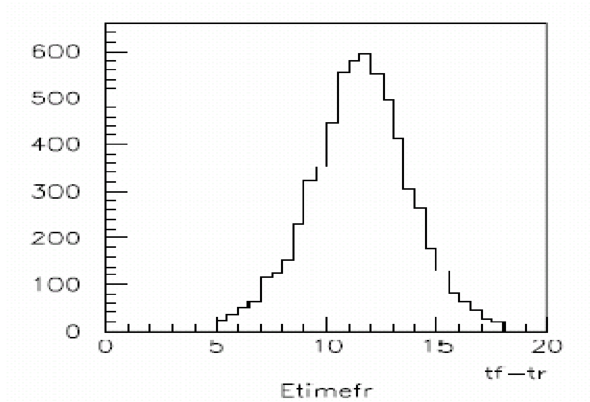

Figure 4.15 . Time difference (ns) between FCAL and RCAL of halomuon candidates

Figure 4.16 compares the halomuon hits before and after event selections and matching of towers for FCAL and RCAL towers with box plot of isoenergy. The size of the boxplots were significantly reduced before and after event selections and matching of towers in both the FCAL and RCAL towers. For both FCAL and RCAL, the isoenergy boxplots after event selections and matching of towers were more or less of the same size, indicating the success of the event selection and matching of towers for the halomuons.

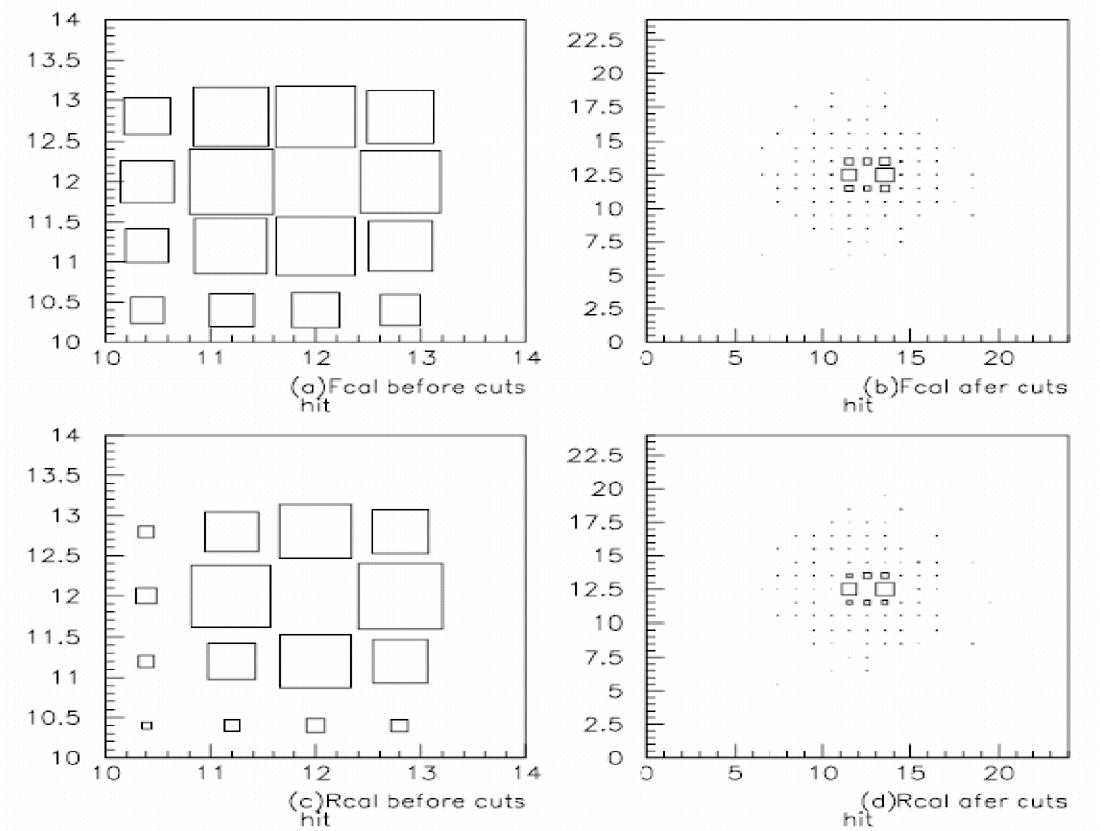

Figure 4.16 Box plots of halomuons isoenergy hits (a) before (b) after event selection and matching of towers in FCAL; (c) before (d) after event selection and matching of towers in RCAL

In **Figure 4.17**, the overall energy distribution (in GeV) in FCAL and RCAL towers after event selection and matching of towers is given. In the FCAL, there two overall energy peaks could be observed i.e. ~0.5GeV and ~1.8GeV. Similarly in RCAL but at peaks ~0.2GeV and ~2.5GeV. The difference in overall energy peaks between FCAL and RCAL might due to the energy loss as the halomuons transverse the ZEUS detector from RCAL to the FCAL, with small fraction of the energy being deposited in FEMC and REMC regions.

In **Figure 4.18, Figure 4.19** and **Figure 4.20,** the halomuons energy distributions for FHAC2, FHAC1 and FEMC are given for towers 11,12, 13 and modules 11,12, 13, with **Figure 4.21** giving the comparison between total halomuons energy (sum of energy both FCAL and RCAL) distributions and the energy distribution halomuons in FCAL (sum of FHAC2, FHAC1 and FEMC) . In **Figure 4.18** and **Figure 4.19,** the halomuons energy peaked at ~1 GeV in FHACs, while in **Figure 4.20** the halomouns energy peak at ~0.2 GeV in FEMC**.** But in RHAC the halomuons energy peaked at ~ 1.2 GeV showing that it loss ~0.2GeV of energy as it transverse to the FHACs.

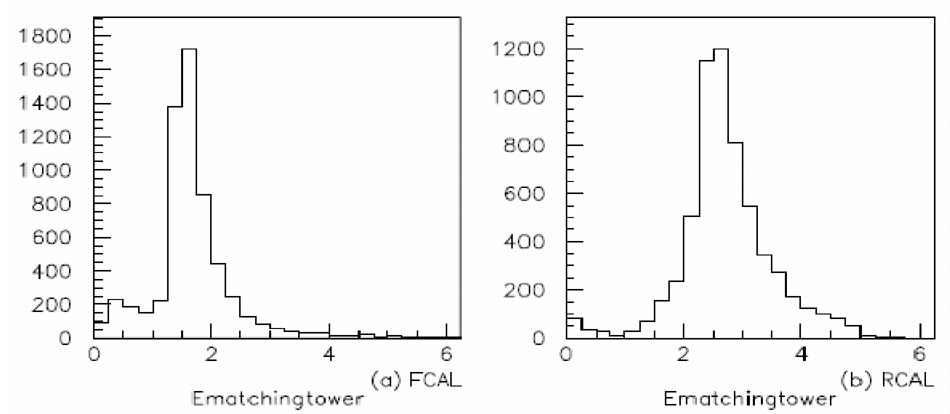

Figure 4.17. Overall energy distribution of halomuons (in GeV) in (a) FCAL (b) RCAL after matching and event selections

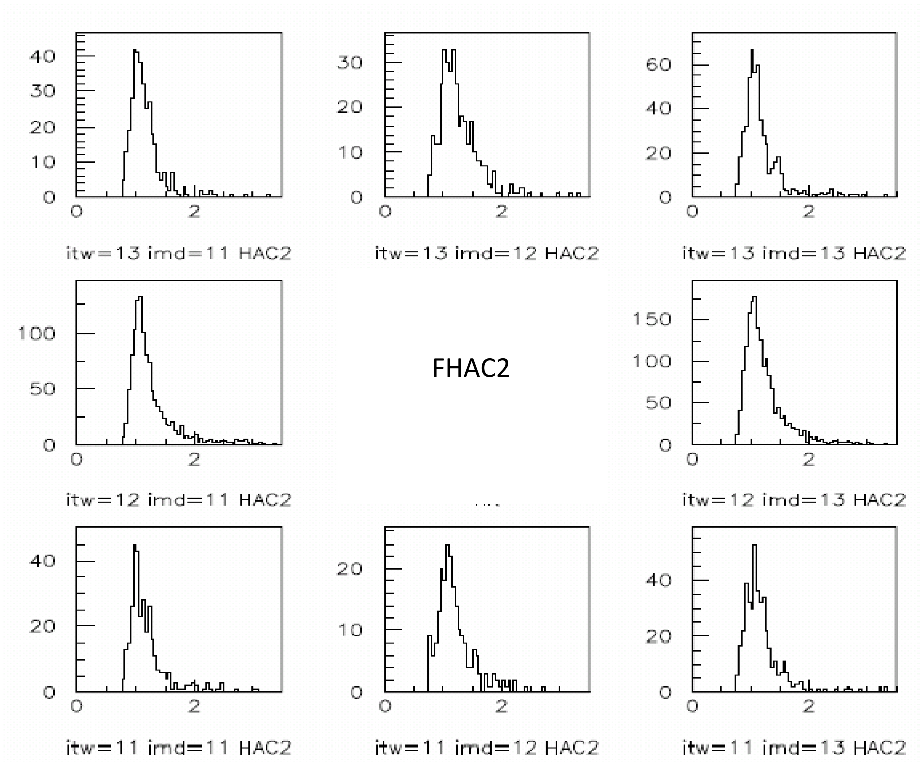

Figure 4.18 Distribution of halomuon energies (in GeV) in the first inner ring of FHAC2 of FCAL

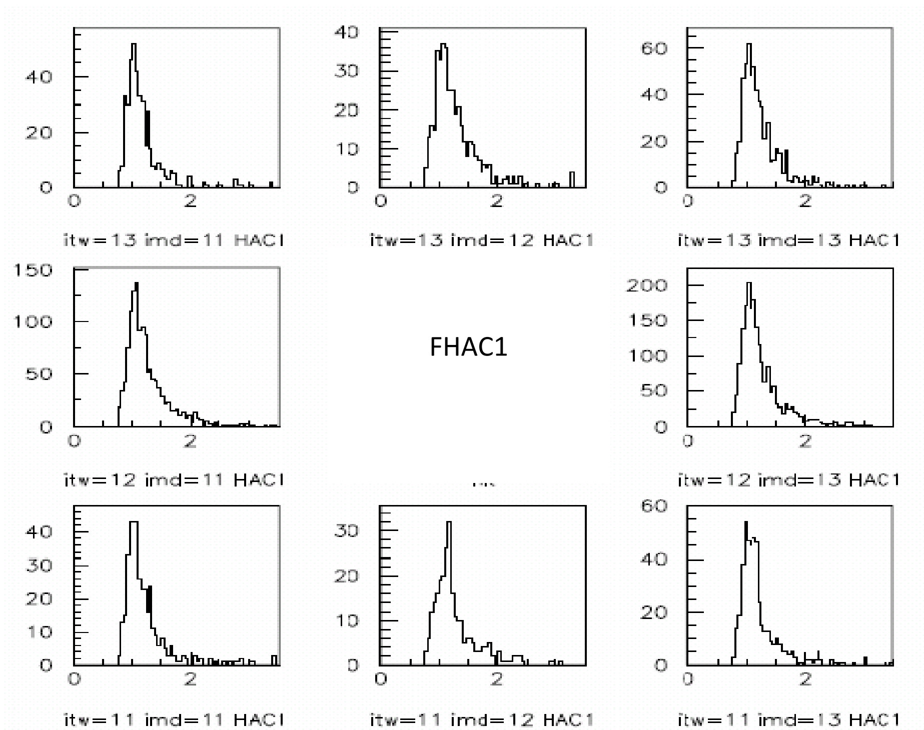

Figure 4.18 Distribution of halomuon energies (in GeV) in the first inner ring of FHAC1 of FCAL

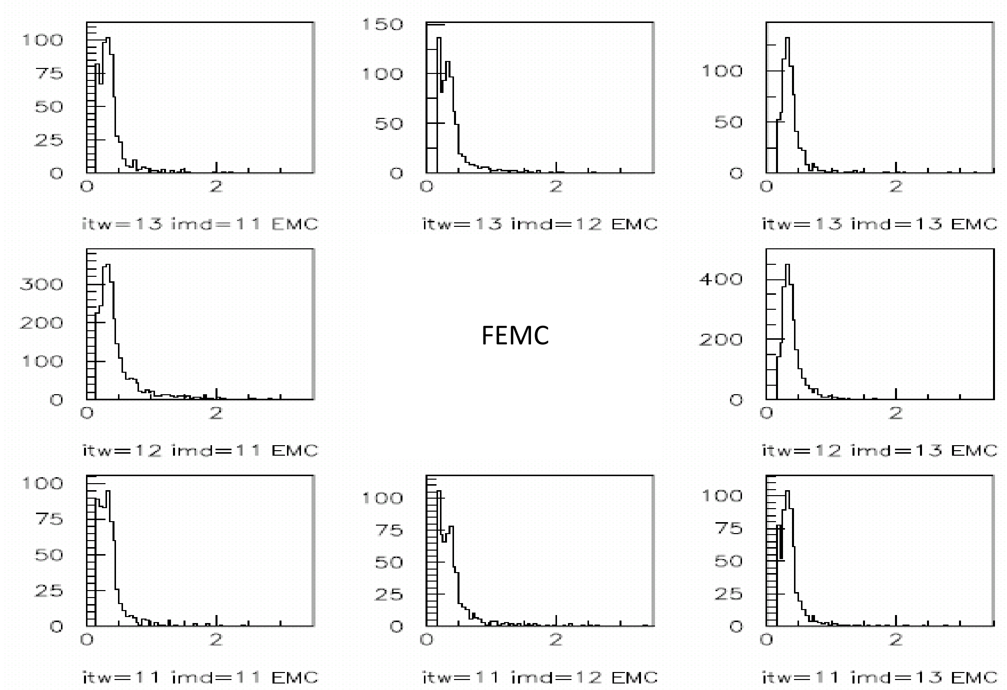

Figure 4.20 Distribution of halomuon energies (in GeV) in the first inner ring of FEMC of FCAL, using CALCAL data (file femc.ps)

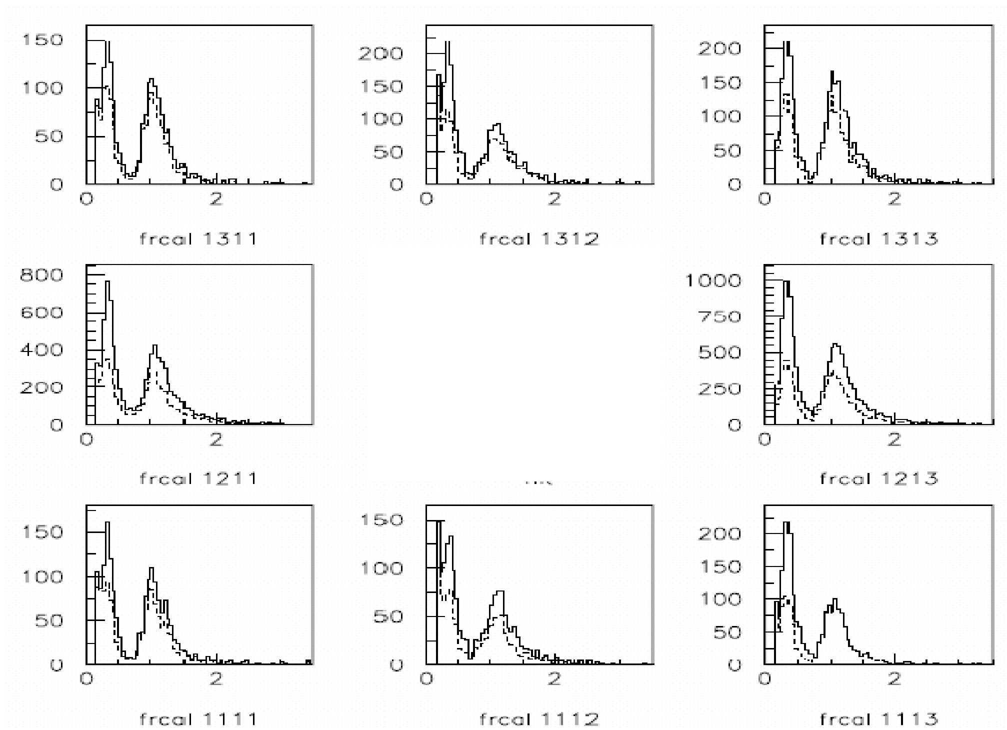

Figure 4.21 Total energy distribution of halomuons in FCAL and RCAL (solid line), in comparison with halomuon energy distribution in FCAL (dash line)

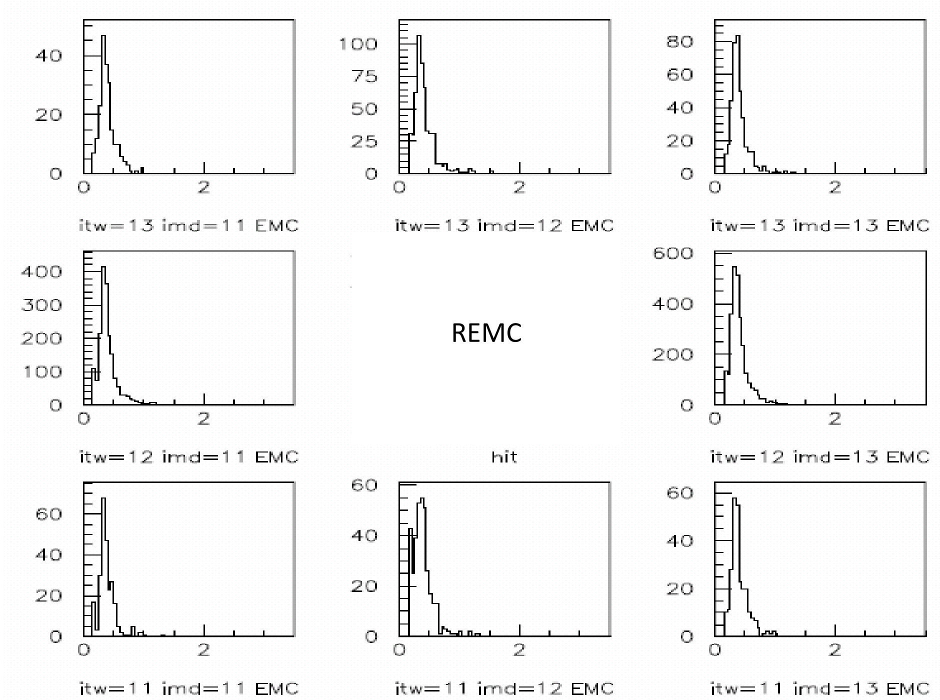

Figure 4.22 Distribution of halomuon energies (in GeV) in the first inner ring of REMC of RCAL, using CALCAL data

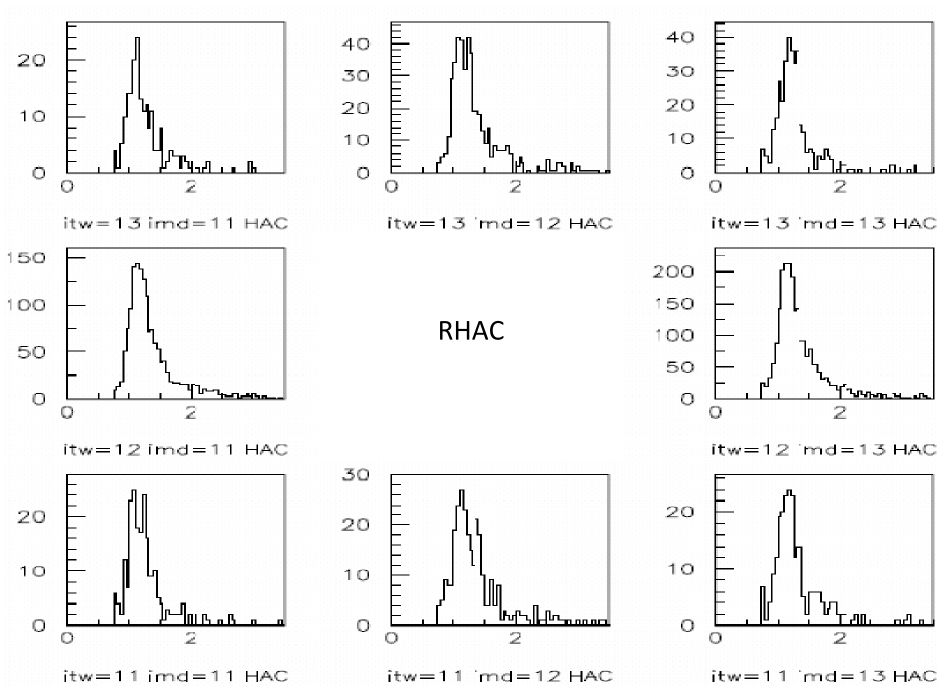

Figure 4.23. Distribution of halomuon energies (in GeV) in the first inner ring of RHAC of RCAL, using CALCAL data

4.2.5 Summary

In **Section 4.2**, the algorithm for identifying halomuons in the ZEUS detector has been described. The halomuons which transverse the ZUES detector from the RCAL to the FCAL show reasonably good Landau distribution in the first inner ring (FIR) of the F/RCAL as part of physics event, with energy range of ~1GeV in the hadronic calorimeter and ~0.5 GeV in the EMC. As muons decay length is large (658.654 m), the halomuons retains most of its energy as its travels from rear to the front end of the ZEUS detector.

CHAPTER 5

EVENT SELECTION AND RECONSTRUCTION

In **Section 3.3** of **Chapter 3**, the particles that emerged from the electron-proton collision in the ZEUS detector and traveled through the detector to deposit their energies in the hadronic and electromagnetic calorimeter of the ZEUS detector and labeled as the ZUFOs (Zeus Unidentified Flow Objects) i.e. objects identified with track type and island information in the CAL (Calorimeter) of the ZEUS detector, has been described.

The kinematic variables of the ZUFO objects reaching the EMC (electronic calorimeter) and hadronic calorimeter (HAC) were reconstructed using the data from energy deposits.

In the following sections, the selection criteria for long-live neutral hadrons in the final states that traveled from in interaction point in the ZEUS detector to deposit their energies in the calorimeter, will be described.

The selection criteria for the potential candidates for the mother of these long-live neutral hadrons were also given. In all cases, the background energy cuts were carried on the ZUFOs energy using curve fit $\exp(a+bx)$, where a and b were the constants determined from the curve fit, and x the energy of ZUFO object-i

5.1 Selection of K_L^0 and n candidates

In **Figure 3.2** of Chapter 3, the longitudinal cross section of the ZEUS detector showed the distance between the centre of the detector and the mid section of the barrel calorimeter (BHAC) was about 2 meters. The distance were the about the same between the centre of the ZEUS detector and the mid section of the forward and rear calorimeters (FHAC and RHAC respectively).

Table 5.1 gives the decay length and mean life of neutron and K_L^0. With the decay length of 2.655×10^8 *km* and mean life of 885.7 *s* neutrons originating from the interaction point would be able to reach the hadronic calorimeter of the ZEUS detector in without much decaying, while K_L^0 with decay length of 15.33 *m* and mean life $5.114\times10^{-8}\,s$ could also reach the hadronic calorimeter in its final state.

Table 5.1 Properties of Neutral hadrons and their decay products

hadron	Invariant mass	Mean life τ	Decay length $c\tau$	Fraction Γ_j / Γ
μ	0.106GeV	20.19703 $\times 10^{-6} s$	658.654m	
$\pi \pm$	0.139GeV	$2.6033 \times 10^{-8} s$	7.8045m	
$\pi^0 \to \gamma\gamma$	0.135GeV	$8.4 \times 10^{-17} s$	25.1 *nm*	98.8%
K^0	0.497GeV			
$K_S^0 \to \pi^+\pi^-$		$0.8958 \times 10^{-10} s$	2.6842 *cm*	69.2%
K_L^0	$m_{K_l} - m_{K_S} = 3.483 \times 10^{-12}\ MeV$	$5.114 \times 10^{-8} s$	15.33 *m*	50% K_S, 50% K_L
n	0.939GeV	885.7 *s*	2.655×10^{8} *km*	
$\phi(1020) \to K_L^0 K_S^0$	1.019GeV			34.0%
$\Lambda^0 \to n\, \pi^0$	1.115GeV	$2.631 \times 10^{-10} s$	7.89*cm*	35.5%

In selecting potential candidates for K_L^0, the ZUFOs entries associated with potential neutral hadrons in the final states were chosen, with following cuts:

(i) Tufo(4,Nzufos)=31: 0 track, 1 island , use CAL

The objects not associated with any tracks i.e. non-charge particles, and form an island in the CAL cells should be selected as potential neutral hadrons in the final states. (If CTD were selected, then object will be tracked using CTD for charged particles).

(ii) $\theta > 17^{\ 0}$ *or* $\theta < 163^0$ and pseudo rapidity $-2 < \eta$ *or* $\eta < 2$)

This removes signal near the beam pipes, especially in near the rear end of the calorimeter. Pseudorapidity $\eta_i = -\ln\left(\tan\frac{\theta_i}{2}\right)$ i.e. Lorentz transformation of θ_i that would give invariant values along the z-axis, particularly useful when photons were involved during the interaction.

(iii) More than 30% of the ZUFOs energy should be deposited in HACs

For potential neutral hadrons candidates in the final states (not associated with electromagnetic radiation) reaching the ZEUs calorimeter, at least 70% of its energy deposited should be deposited in the HACs regions, while the remaining 30% could be deposited in the EMC region as the neutral hadrons passed through it [3].

(iv) $38\,GeV < \delta < 65\,GeV$.

The above cut will ensure that the potential hadron candidates were not from events with large initial-state radioactive corrections and further reduce the background photon contamination. [7], [28], [64]. Here, $\delta = E_i - p_{z_i} = E_i(1-\cos\theta)$ is energy of object-i in z-direction.

(v) Background cuts on energy selection were applied, when less than 1% of the ZUFOs energy deposited in HACs region.

Background fits were carried out using $\exp(a+bx)$, where a and b were the constants determined from the curve fit and x as the energy of ZUFOs object-i. The above (i) to (iv) cuts were applied after background cut on energy entries were carried out.

For neutron event selection, the cuts (i) to (v) were used, but in cut (iv) **only** the first part of i.e. $\theta > 17^{0}$ *or* $\theta < 163^{0}$, was used to ensure that potential neutron candidates in the forward direction were not totally eliminated from event selection, as neutrons has low transverse momentum but high in the z-component.

5.2 Selection of K_S^0 candidates

The selection of K_S^0 candidates were carried out using the $K_S^0 \to \pi^+\pi^-$ channel using the entries in the V0 block. With mean life of $0.8953 \times 10^{-10}\,s$ and decay length of 2.6842cm, measurement of K_s^0 momentum directly is difficult, as it would decay before reaching the any superlayers of the CTD. But the decay products of K_s^0, i.e. $\pi^\pm$ with mean life of $\pi^\pm$ of $2.6033 \times 10^{-8}\,s$ and decay length of 7.8045m, would be more suitable as CTD hit candidates. **Table 5.1** gives the properties of production $\pi^+\pi^-$ production from the $K_S^0 \to \pi^+\pi^-$ channel.

Momentum of π^+ and π^- (with invariant mass =0.139GeV) candidates of pions selected should fulfill certain criteria [31], one of them being that the candidate should at least reach superlayer 3 outwards to fulfill the decay length of $\pi^\pm$. **Table 3.1** of Chapter 3 gave the centre radius of superlayers in the CTD of ZEUS detector, while **Figure 3.8** gave the radial layout of the CTD. Assuming that pions should reach at least superlayer 3 of the CTD, candidates are selected such it should reach superlayer 3, 5,7 and 9 [41].

The selected $\pi^+\pi^-$ pair should have the following criteria:

(i) The V0 candidates should be exclusive i.e. it should only be associated with only one lone hadron

(ii) The V0 candidate associated with $\pi^+\pi^-$ pair should be associated with only two tracks of ZTT type, to reduce multiplicity of tracks from other sources than $K_S^0 \to \pi^+\pi^-$ from the vertex

(iii) The $\pi^\pm$ pair should reach at least superlayer 3 of the central tracking detector (CTD)

(iv) The separation Δz of the two tracks at their xy intersection point, should be $|\Delta z| < 2.cm$ [16]. As an approximation $|(\sin\theta_{p\pi^+} - \sin\theta_{p\pi^-})| < 2.5$ were used, this cut would ensure that $\pi^+\pi^-$ pair lays within the decay length range of K_S^0.

(v) The angle α_{XY} between the transverse plane of the K_S^0 candidate and its reconstruction momentum direction, should in the same direction i.e. $Cos(\alpha_{XY}) > 0.9$ [16].

(vi) The decay length of K_S^0 candidate should be less than 10cm [16]. (Mean life of K_S^0 $\approx c\tau(M\ c)/p$, with p as the momentum of $K_S^0\cdot$ candidate, M its invariant mass and $c\tau$ as its mean life, and c as the speed of light.

(vii) The transverse momentum p_T of K_S^0 candidate should be greater than 0.15GeV for daughter –track [16].

(viii) $38\,GeV < \delta < 65\,GeV$ cut for K_S^0 was applied to reduce events from large initial-state radiative corrections and further reduces the background photon contamination [7], [28], [64], with $\delta = E_i - p_{z_i} = E_i(1-\cos\theta)$ as the energy of K_S^0 candidates in z-direction.

(ix) Cuts $abs(Mass(\pi^+\pi^-) - Mass(K_S^0)) < 0.02GeV$ was applied to narrow down mass selection of $\pi^+\pi^-$ candidates that contributed to actual K_S^0 mass.

(x) The acollinearity angle of the $\pi^+\pi^-$ candidates should be less than 3.0 [65]

5.3 Selection of scattered electrons and photons in $e(k)\ p(P) \rightarrow e'(k')\ p'(P')\ X\gamma$ interaction

During the electron-proton collision in the ZEUS detector, the incoming electron would transfer some of its initial momentum in deep inelastic scattering (DIS) and scattered off towards the rear calorimeter, as shown in **Figure 2.3** through VDM or **Figure 2.4** through pQCD model**.** The magnitude of electron's momentum loss from its initial state during DIS would give an indication of the DIS process through the variable Q^2 given by **Equation (2.19)** in **Section 2.7.1.**

In the following **Section 5.3.1,** the selection of electrons that scattered off from the DIS interaction using the ZUFOs entries is described, while **Section 5.3.2** describes the selection of photons in the direction of the scattered electron.

5.3.1 Selection of scattered electrons

The following cuts were applied to select electron candidates that scattered off from the DIS interaction using the ZUFOs entry:

(i) Tufo(4,Nzufos)=1: 1 track, 1 island , use CTD

The ZUFO objects associated with one track charge particles, and form an island in the CAL cells should be selected as potential electron candidates using CTD.

(ii) More than 95% of the ZUFOs energy should be deposited in EMC

For potential electron candidates (associated with electromagnetic radiation) reaching the EMC, majority 95% of its energy deposited should be deposited in the EMC regions, while the remaining 5% could be loss throughout its trajectory from the interaction point.

(iii) The scattered electron should be in 1.2 rad and 3.1 rad region for K_L^0 event selection i.e. in backward region of the detector.

Electron candidate should be in the rear region of the calorimeter, but not in near the beampipe region

(iv) $38\,GeV < \delta < 65\,GeV$ cut was applied to reduce events from large initial-state radiative corrections and further reduces the background photon contamination [7],[28],[64], with $\delta = E_i - p_{z_i} = E_i(1-\cos\theta)$ as the energy of scattered electron candidates in z-direction

(v) The scattered electron candidates should be associated with only two tracks of ZTT type.

(vi) Electron candidates should be also in the same direction of electrons from SIRA finder, as SIRA finder has the necessary algorithm for finding electrons in the ZEUS detector

5.4 Selection of Double Photon candidates from $\pi^0 \to \gamma\gamma$ decay

To reconstruct Λ^0 mass from the $\Lambda^0 \to n\,\pi^0$ channel, double photon candidates in the direction of neutron production would have to be selected. The following cuts were applied on the neutral ZUFOs object to select potential $\gamma\gamma$ candidates for the $\pi^0 \to \gamma\gamma$ reconstruction:

(i) Tufo(4,Nzufos)=31: 0 track, 1 island , use CAL

The photon candidates should not be associated with any track i.e. non-charge particles, and form an island in the CAL

(ii) $38\,GeV < \delta < 65\,GeV$

The photons selected should be clear from contamination of photons from background events and large initial-state radiative corrections events [7], [28],[64], with $\delta = E_i - p_{z_i} = E_i(1-\cos\theta)$ as energy of selected photons in z-direction.

(iii) More than 90% of the ZUFOs energy should be deposited in EMC [50]

For potential photon candidates more than 90% of its energy should be deposited EMC regions .

(iv) Momentum component in the z-direction of selected candidates should be greater than 0.9GeV, to ensure that the selected photon candidates moved in the forward direction

(v) Pseudorapidity $-1.25 < \eta < 2.0$

The above cut ensure that the photon candidates would be in the 'forward' region in the laboratory mass, or in the central region in the hadron centre-of-mass frame [50]

(vi) The angle α_{XY} between the transverse plane of the neutron from $\Lambda \to n\pi^0$ and the photons candidates from $\pi^0 \to \gamma\gamma$ decay and the photon's reconstruction momentum direction, should in the same direction i.e. $Cos(\alpha_{XY}) > 0.9$

(vii) The distance between two photon candidates should be between 1.5cm and 4cm

The above cuts was to ensure that the double photon was sufficiently separated from the decay of 50GeV π^0 and, the minimal separation in the very low Q^2 of 4cm for the two photons from the decays of π^0 mesons with actual minimum energy of 20GeV [51]

(viii) The reconstructed π^0 mass should be between $0.133 < \sqrt{E_{\gamma\gamma}^2 - p_{\gamma\gamma}^2} < 0.137\ GeV/c^2$ to narrow down the photon candidates that actually contributed to π^0 mass.

5.5 Reconstruction of $\phi(1020)$ from $\phi(1020) \rightarrow K_L^0 K_S^0$ channel

In the **Section 5.1** to **Section 5.3**, the selection of long-lived neutral hadrons K_L^0 candidates reaching the hadronic calorimeter of the ZEUS detector were described. The kinematic variables of K_L^0 candidates as given in **equations (2.14) to (2.28) of Section 2.7 in Chapter 2**, were reconstructed.

The mass of $\phi(1020)$ i.e. $M(\phi(1020)) = M(K_L^0 \; K_S^0)$, were reconstructed from the reconstructed masses of K_L^0 and K_S^0 respectively. Results from the reconstructed events were given in **Chapter 6** of this thesis.

5.6 Reconstruction of Λ^0 from $\Lambda \rightarrow n\pi^0$ channel

In **Sections 5.1** the selection of neutron candidates has been described, while in **Sections 5.4** the selection of double photon from $\pi^0 \rightarrow \gamma\gamma$ decay were given. With both masses, the mass of Λ^0 i.e. $M(\Lambda) = M(n\,\pi^0)$, were reconstructed. Results from the reconstructed events were given in **Chapter 6** of this thesis.

5.7 Comparison with Monte Carlo Simulation

To compensate deficiencies of the detector during measurements, factors efficiency and purity would be used to correct for actual measurements. The efficiency is defined as [9],

$$Efficiency(i) = \frac{n^{\det.and.had}(i)}{n^{had}(i)} \tag{5.1}$$

where $n^{had}(i)$ is the number of Monte Carlo events simulated in at the hadron level after passing selection criteria in bin-i, and $n^{\det}(i)$ is the number of events measured at the detector level after passing all cuts in bin-i.

Purity is defined as [9],

$$Purity(i) = \frac{n^{\det.and.had}(i)}{n^{\det}(i)} \tag{5.2}$$

Acceptance is the ratio of the number of events generated in a bin and passed event selection to the number of events generated in the selected bin [2]. It takes into account the geometric effect of the detector and is with is defined as [9],

$$Acceptance(i) = \frac{Efficiency(i)}{Purity(i)} \tag{5.3}$$

To correct for the deficiency of the detector, the correction factor is defined as,

$$Correction(i) = \frac{1}{Acceptance(i)} \tag{5.4}$$

The corrected variable is determined by [9],

$$P^{cor}(i) = Correction(i) \cdot P^{CAL} \tag{5.5}$$

with P^{CAL} as the measured parameter from the calorimeter of the ZEUS detector.

Equations (5.1) to (5.5) above would be used to correct the measurements of the ZUFOs objects in the calorimeter of the ZEUS detector.

In efficiency selection, the momentum of potential hadron candidates from the ZUFOs objects not associated with any tracks but form islands in the ZEUS calorimeter were matched against simulation data from generated Monte Carlo. These momentums were then matched in magnitude and direction of the measured hadrons that has passed selection criteria.

In purity selection, the momentum of potential hadron candidates after passing event selection was matched in magnitude and direction against the momentum simulated by Monte Carlo.

5.8 Differential Cross Section

The differential cross section σ of the variable momentum p of hadron candidates, calculated using a standard by bin correction is given by [28],[64],

$$\frac{d\sigma}{dp} = \frac{N}{A \cdot L \cdot B \cdot \Delta Y.} \tag{5.6}$$

where N is the number of events hadron candidates in a bin of size ΔY, A is the acceptance, L is the integrated luminosity (2006/2007) of 145.90pb^{-1} and B is the branching ratio taken to be 34.0% for $\phi(1020) \rightarrow K_L^0 \; K_S^0$ decay channel and 35.5% for $\Lambda \rightarrow n \; \pi^0$ decay channel.

5.9 Summary

In this chapter, the event selections for the reconstruction of $\phi(1020)$ from decay channel $\phi(1020) \rightarrow K_L^0\ K_S^0$ and Λ from decay channel $\Lambda \rightarrow n\ \pi^0$ were described using the ZUFOs objects in the calorimeter of the ZEUS detector were described.

The selection of K_L^0 and neutron n candidates using ZUFOs objects not associated with any track is limited to only four variables (azimuthal and polar angle, CAL energy, EMC energy of the ZUFOs object) may reduce the resolution of the K_L^0 and neutron n mass peak and consequently the mass peak of $\phi(1020)$ and Λ .

The differential cross section of $K_L^0, \phi(1020)$, neutron and Λ with respect to its momentum would be compared with its respective momentum from Monte Carlo simulation in the next section.

CHAPTER 6

RESULT AND DICUSSION

In **Section 5.1** of **Chapter 5**, the event selections for long-lived neutral hadrons in the final states candidates found in the calorimeter of the ZEUS detector were described. The cuts applied on potential candidates for $K_L^0, K_S^0, n, \gamma, e$ particles to narrow down to the most probable ones were carried out, to reconstruct the invariant mass of light unflavored meson $\phi(1020)$ through $\phi(1020) \rightarrow K_L^0 K_S^0$ channel and baryon Λ through $\Lambda \rightarrow n\pi^0$ channel, and its associated kinematics variables as described in **Chapter 3**.

Selection criteria for electrons scattered from the electron-proton collision were also given in **Section 5.3.1** of **Chapter 5** to find associations between the scattered electrons and the particles $\phi(1020)$ produced during the interaction. The selection criteria for photons scattered of from the scattered electron were also given. This category of photons was different from the ones originating from $\pi^0 \rightarrow \gamma\gamma$ decay through $\Lambda \rightarrow n\pi^0$ channel.

In this chapter, we present the results from cuts applied from **Chapter 5**, including the reconstructed variables associated with $\phi(1020) \to K_L^0 K_S^0$ as given in **Section 6.1)**, and $\Lambda \to n\pi^0$ decay channels given in **Section 6.2**.

6. 1 Reconstruction of $\phi(1020)$ mass from $\phi(1020) \to K_L^0 K_S^0$ channel

In **Section 5.2**, the selection criteria for candidates long lived neutral hadrons reaching the hadronic calorimeter of the ZEUS detector was given. In the following sections, the results from event selections of K_L^0 and K_S^0 candidates were given, with the former from the ZEUS Unidentified Flow Objects (ZUFOs) not associated with any tracks, while the latter from V0lite entries of $\pi^+\pi^-$ candidates for the reconstruction of K_S^0 through $K_S^0 \to \pi^+\pi^-$ decay channel. The potential $\phi(1020)$ candidates were constructed from the K_L^0 and K_S^0 candidates from decay channel $\phi(1020) \to K_L^0 K_S^0$ using the invariant mass $m(\phi(1020)) \to m(K_L^0\ K_S^0)$.

The results of the reconstructed scattered electrons $e(k')$ from $e(k)\ p(P) \to e(k')\ p(P')\ X\gamma$ interaction are also given the following section.

In this section, the result from grand reprocessing Monte Carlo data from Ariadne simulation data (Ariadne067p_GR) was used with the results given and discussed in the following sections.

6.1.1 Reconstruction of K_L^0 kinematic variables

In this thesis, the reconstruction of kinematic variables for K_L^0 was based on the energy of ZEUS Unidentified Flow Objects (ZUFOs) in hadronic calorimeter that was not associated with any tracks and identified as neutral energy. Conventionally, the ZUFOs energy tracks were determined by assuming the associated particles were pions [11].

Thus the reconstruction of neutral ZUFO object K_L^0 were limited to only four variables, i.e. firstly the of azimuthal and polar angles of the K_L^0 candidates from the ZUFOs momenta as given in **Equations (2.14)** and **(2.15)** of **Section 2.9** in **Chapter 2** of this thesis, secondly the energy zufo(4,Nzufos) of object-i in the ZUFOs four-momenta, thirdly the CAL energy zufoEcal(Nzufos) and finally the CAL EMC energy zufoEemc(Nzufos).

The following results were reconstructed based on the kinematic variables as described in **Section 2.9** in **Chapter 2.**

6.1.2 Background cuts

Figure 6.1a shows slight "bump" shape on the plot of energy of potential K_L^0 candidates (solid line) after undergoing selections as given in **Section 5.1**, as compared with the background signal (dash line) i.e. when the ratio of electromagnetic to hadronic energy of potential K_L^0 candidates was less than 1 % .To eliminate the background signal, the background was fitted with function $e^{a+b*zufo(4,i)}$ (refer to **Figure 6.1b**, with *a* and *b* constants and Zufo(4,i) as the energy of object-*i*) and later subtracted from the solid line **Figure 6.1a.**

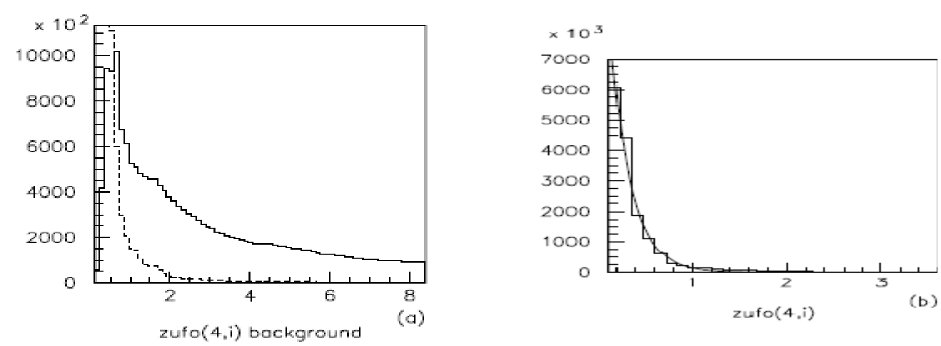

Figure 6.1a Comparison of ZUFOs energy $zufo(4,i)$ for object-*i* not associated with any track (solid line) against its background signal (dash line); (b) the background signal is curve fitted using function $e^{(a+b*zufo(4,i))}$ and is then used to isolate the ZUFOs energy of K_L^0 candidates from its background signal.

6.1.3 The four-momenta of K_L^0 candidates

In **Section 2.9** of this thesis, the kinematic variables of the ZUFO objects in the calorimeter of the ZEUS detector were described, with the momentum components in x, y, z direction, in terms of energy E azimuthal angle θ and polar angle ϕ, as given in **Equations (2.17), (2.18)** and **(2.9)**.

In **Figure 6.2**, the four-momenta of the hadronic ZUFOs momentum that was not associated with any tracks is given. **Figure 6.2(a)** shows the energy of potential K_L^0 candidates after undergoing background cut as described in **Section 6.1.1.1,** peak at 5GeV. The energy gap around 10GeV in **Figure 6.2(a)** might due to the supercrack i.e. a gap between the RCAL and BCAL region in the ZEUS detector.

Of the four-components, the x, y and z momentum components were used only to calculate cosine polar angle $\cos\theta$ and cosine azimuthal angle $\cos\phi$ of K_L^0, as candidates as the ZUFOs energy tracks were determined by assuming the associated particles were pions [11].

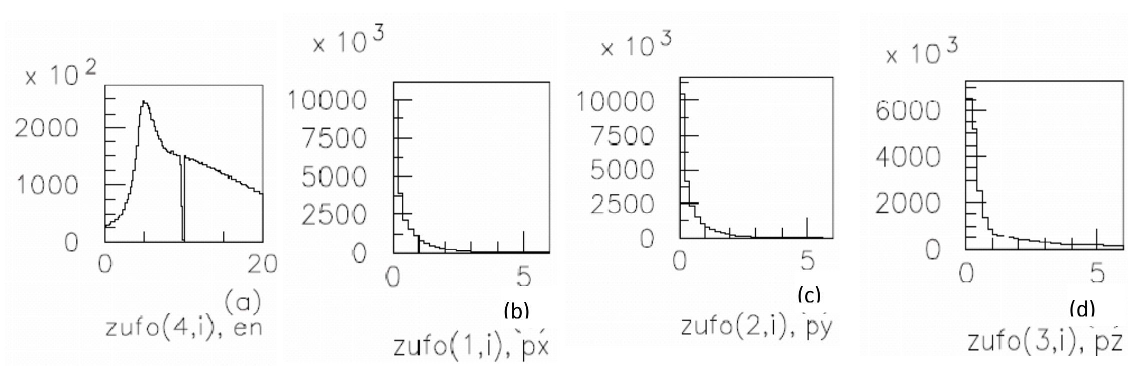

Figure 6.2 The four-momenta from ZUFOs entry for object-i not associated with any track (a) energy (GeV) of K_L^0 candidates and its associated momentum components (in GeV) (b) in x-direction (c) in y-direction (d) in z-direction assuming the particles as pions.

Figure 6.3(a) shows the measured cosine azimuthal angle $\cos\phi$ of K_L^0 candidates with the maxima appears to be at ~ 1 (0^0) and 0.75 (41^0). **Figure 6.3(b)** shows $\cos\phi$ of K_L^0 candidates, obtained from Monte Carlo simulation, with the momentum matched against its measured value. Both **Figure 6.3(a)** and **Figure 6.3(b)** showed similar trend but in the former there is additional peak at 0.75 (41^0).

Figure 6.4 shows cosine polar angles of K_L^0 candidates with $\cos\phi$ seemed to be oscillating with peaks at 0.15 (81^0), 0.35 (69^0), 0.575 (55^0), 0.725 (43.5^0), 0.65 (49^0). The effect in the latter could b attributed to the calorimeter segmentation of the calorimeters into modules and towers with front face of $25cm \times 21cm$.

The energy component as given in **Figure 6.2(a)** and the azimuthal from **Figure 6.3(a)** and polar angles as in **Figure 6.4** would be later used to reconstruct of kinematic variables of K_L^0 with the results as given in the following sections.

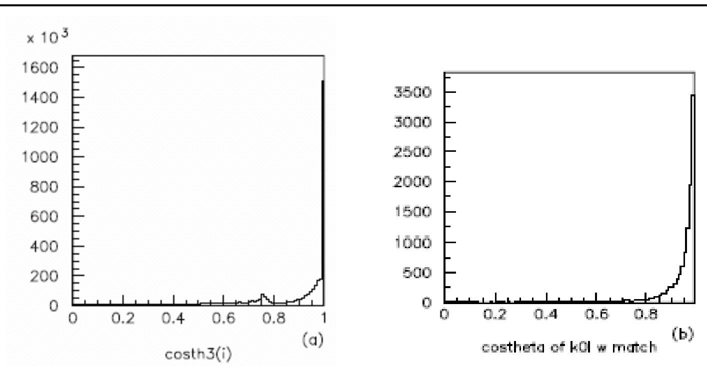

Figure 6.3 Cosine polar angles of K_L^0 candidates (a) measured $\cos\theta$ and (b) $\cos\theta$ from Monte Carlo simulation

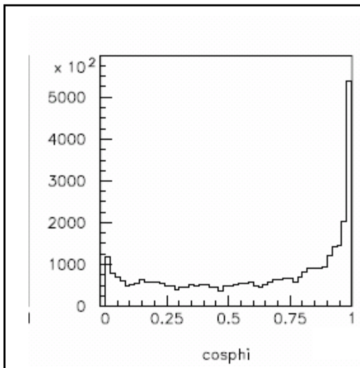

Figure 6.4 Azimuthal angles $\cos\phi$ of K_L^0 candidates

Figure 6.5 shows **,** the momentum of K_L^0 candidates calculated using **Equations (2.17), (2.18)** and **(2.19)** (of **Section 2.9 in Chapter 2),** assuming that neural hadron dissipated its energy in the same manner as photon and, using event selections as given in **Section 5.1 of Chapter 5**. The momentum of K_L^0 candidates in **Figure 6.5(a)** shows a maximum at 6GeV, similarly with the z-component in **Figure 6.5 (d),** as compared with the x and y-components. This indicates that the tendency of movement of K_L^0 candidates is more towards the front region of the calorimeter than the barrel region, and in contrast to **Figure 6.2(d)** that indicate significant transverse momentum from the ZUFOs object-i not associated with any track was treated as a pion.

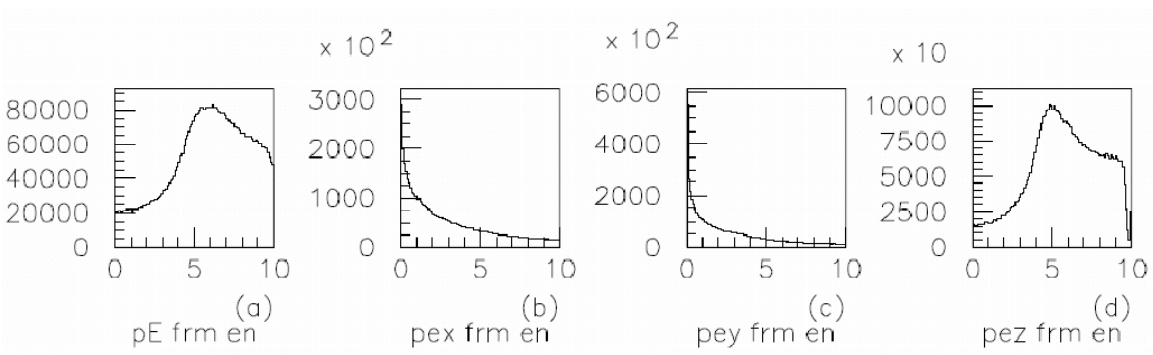

Figure 6.5 Reconstructed momentum distribution of K_L^0 candidates (a) momentum of K_L^0 candidates (b) momentum in x-direction (c) momentum in y-direction (d) momentum in z-direction

6.1.4 Kinematic variables of K_L^0

Figure 6.6 gives the transverse properties of K_L^0 candidates, with **Figure 6.6(a)** showing the transverse energy of the candidates, **Figure 6.6(b)** the transverse momentum of K_L^0 candidates, and in **Figure 6.6(c)** the $\delta_i = E_i - p_{zi}$ for K_L^0 candidates.

From **Figure 6.6c**, it appears that difference between the energy of K_L^0 candidates and its momentum in the z-direction is small. In **Figure 6.6a,** the transverse energy peak of K_L^0 candidates at about 0.5GeV, while **Figure 6.6b** shows the almost linear transverse momentum of the K_L^0 candidates.

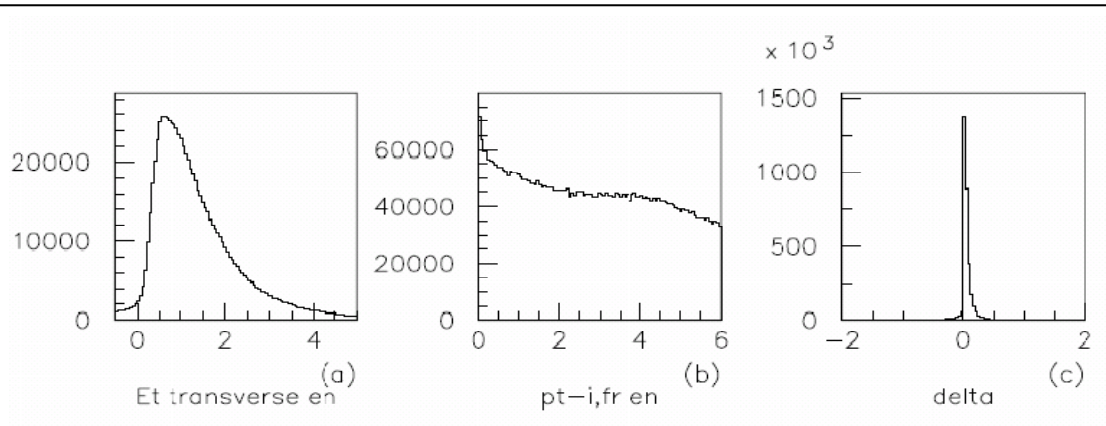

Figure 6.6 Transverse properties of K_L^0 candidates: (a) transverse energy (in GeV) (b) transverse momentum (in GeV) (c) $\delta_i = E_i - p_{zi}$ (in GeV)

Figure 6.7 shows the rapidity *y* and pseudorapidity η of K_L^0 candidates. In **Figure 6.7a,** the entries are given only in the forward region of the detector, while in **Figure 6.7b** the entries are given in both the forward and rear region of the detector, with $-2 < \eta < 2$ in barrel direction of the ZEUS detector when the Lorentz transformation in almost linear, while outside this region (close to the beam pipe in the forward and rear region of the detector) η values would most probably include reactions near the beampipe region. In both **Figure 6.7a** and **Figure 6.7b,** the highest entries is at $\eta \sim 0.8$, indicating the production region of K_L^0 highest around this region.

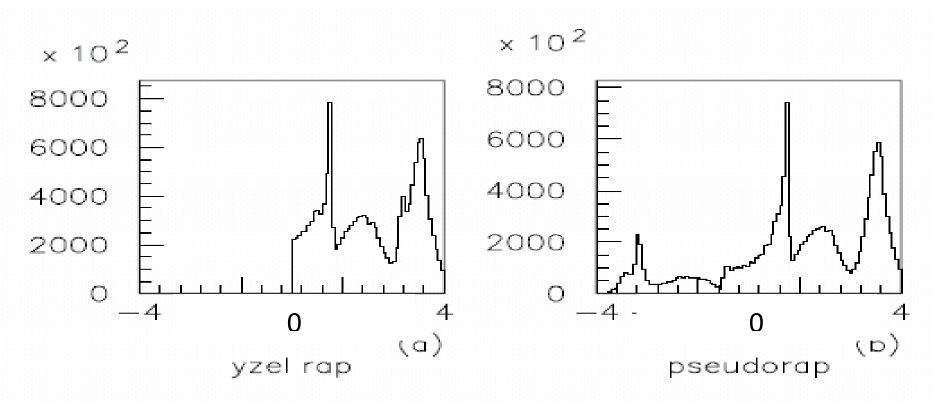

Figure 6.7 (a) Rapidity and (b) pseudorapidity of K_L^0 candidates

Figure 6.8a gives the momentum gain $Q^2 = -(k-k')^2$ from incoming electron during the DIS, showing Q^2 from the Jacquet-Blondel method to be in the range from 0 to 100GeV, as compared with **Figure 6.10d** (see the following **Section 6.15**) that shows $Q^2 = -(k-k')^2$ to be in slightly higher range of 0 to 150GeV from the electron method. For relatively low Q^2, the electron method is more preferable for its higher resolution [28] as given in **Section 2.9.1** of **Chapter 2**.

Figure 6.6c shows fraction $x_{JB} = \frac{Q^2}{sy_{JB}}$ of transferred proton momentum to a struck quark from Jacquet-Blondel method, while **Figure 6.6 (d)** gives the centre-of-mass $W_{JB} = \sqrt{y_{JB}\, s}$, for the intermediate boson-proton interaction during DIS, with peak at about 25GeV.

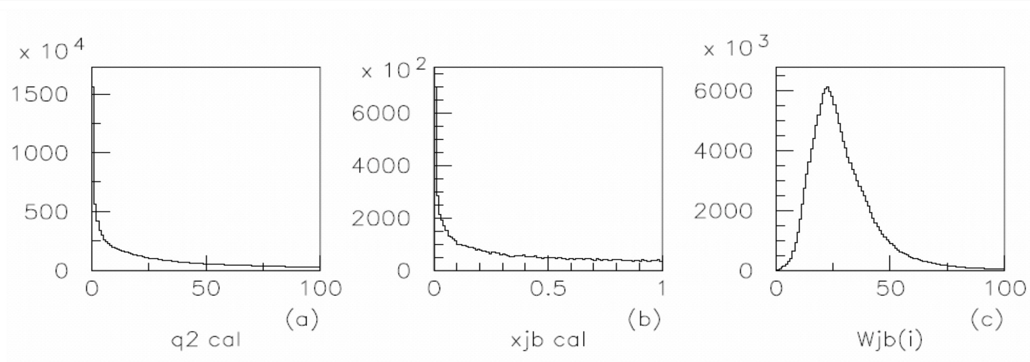

Figure 6.8 Properties of reconstructed K_L^0 reconstructed candidates (a) Momentum gain from incoming electron $Q^2 = -(k-k')^2$;(b) $x_{JB} = \frac{Q^2}{sy_{JB}}$ as fraction of transferred proton momentum to a struck quark ;(c) centre-of-mass $W_{JB} = \sqrt{y_{JB}\, s}$, for the intermediate boson-proton

6.1.5 Reconstruction of Scattered electrons in $e(k)\ p(P) \rightarrow e'(k')\ p'(P')\ X\gamma$ interaction

In the Deep Inelastic Scattering (DIS), the electron remnant $e'(k')$ from the electron-proton collision carries with it the leftover of momentum transferred to the real photon during the DIS to produce $\phi(1020)$.

Figure 6.9 gives the reconstructed momentum of the scattered electron $e'(k')$ candidates from DIS interaction, using ZUFOs associated with charge tracks in EMC of ZEUS detector, with event selection as given in **Section 5.3.1** of **Chapter 5**. The scattered electrons from DIS interaction were selected to be the rear region i.e. 1.2 rad and 3.1 rad of the calorimeter.

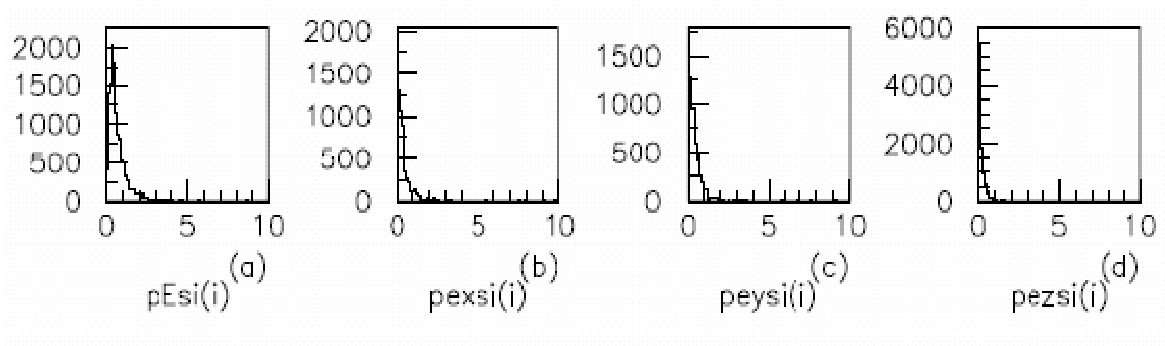

Figure 6.9 Reconstructed momentum of scattered electron candidates from DIS (a) momentum of scattered electron with (b) in x-direction; (b) y-direction (c) in z-direction, using ZUFOs charge tracks in EMC of ZEUS detector

In **Figure 6.10a** the polar angle θ_e at ~ 1.3 radian shows that the remnant electron $e'(k')$ was in the rear region of the calorimeter. **Figure 6.10b** shows the azimuthal angle ϕ_e of scattered electron, while **Figure 6.10c** the energy remnant the scattered electron $e'(k')$ after DIS the to be in the range of 0 to 2GeV.

Figure 6.10d, shows the virtual photon gain $Q^2 = -(k-k')^2$ to be in the range of 0 to 150GeV using the electron method, , indicating "hard" interaction involved during DIS.This gain is comparable to the Q^2 from the Jacquet-Blondel method as given in **Figure 6.8(a)** of **Section 6.1.4,** and is higher in resolution for relatively low Q^2.

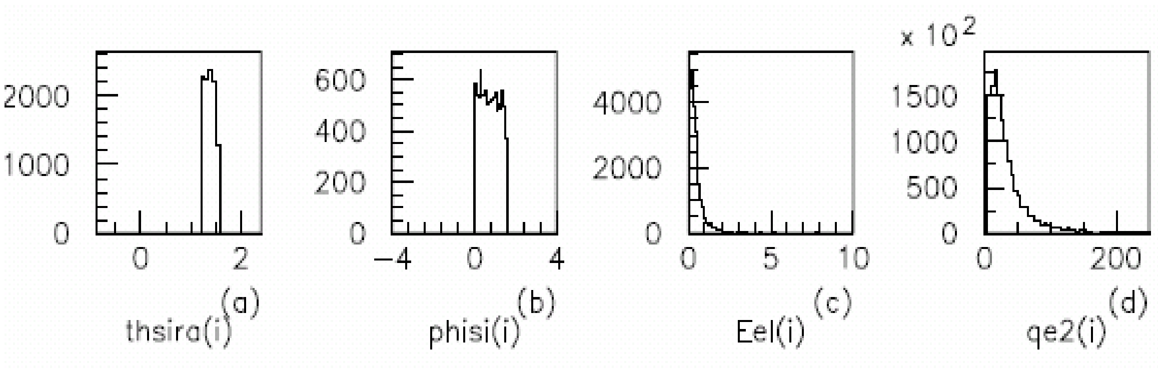

Figure 6.10 Properties of reconstructed scattered electron candidates from DIS (a) polar angle θ in radian; (b) azimutal angle ϕ in radian (c) energy (GeV); (d) virtual photon gain $Q^2 = -(k-k')^2$, using ZUFOs charge tracks in EMC of ZEUS detector

Figure 6.11 shows two dimensional plot of energy (from **Figure 10(b)**) of remnant electron $e'(k')$ from DIS (in direction 1.3 radian) versus the photon momentum gain $Q^2 = -(k-k')^2$. The linear correlation between both variable in this plot indicates the linear dependency of Q^2 on the scattered electron's energy or as $Q_i^2 = 2E_{ei}E_{ei}^{'}(1+\cos\theta_{ei})$ from the electron method as given in **Equation (2.30)** in **Section 2.9.1**

In **Figure 6.12**, the two dimensional plot of $Q^2 = -(k-k')^2$ versus centre-of-mass $W_{JB} = \sqrt{y_{JB}\ s}$ for the intermediate boson-proton W_{JB} shows that the photon momentum gain Q^2 dependency on W_{JB} is almost cluster-like, with the highest around (W_{JB}, Q^2) ~ (20GeV, 15GeV^2)

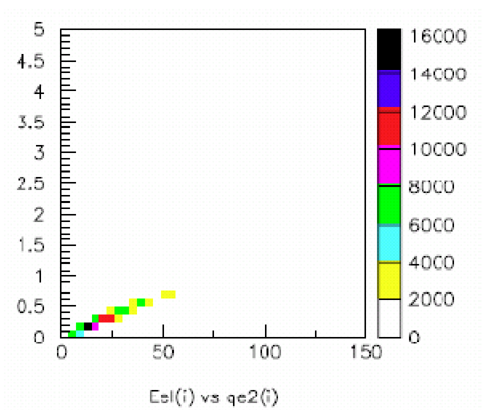

Figure 6.11 Two dimensional plot of energy (GeV) of scattered electron candidates from DIS vs. $Q^2 = -(k-k')^2$.(GeV)^2

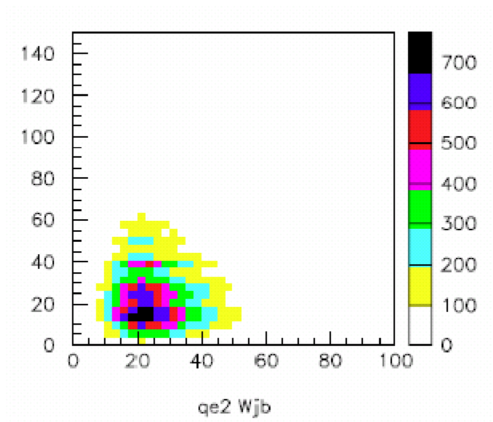

Figure 6.12 Two dimensional plot of $Q^2 = -(k-k')^2$ vs centre-of-mass $W_{JB} = \sqrt{y_{JB}\ s}$ for the intermediate boson-proton

6.1.6 Reconstructed mass of K_L^0

In the deep inelastic scattering (DIS) during electron-proton collision, the virtual photons emitted by the incoming electron behave in point-like manner to fluctuate into the proton via an exchange of pomeron to produce vector meson ϕ that decays into K_L^0 and K_S^0.

In **Section 2.9** of this thesis, the kinematic variable of ZUFO object-i in the calorimeter of the ZEUS detector has been described. By assuming that neutral hadrons dissipate its energy in the same manner as photon (i.e. $E^2 = p^2$ [27]), **Equations (2.17), (2.18) and (2.19)** were used to approximate the momentum of neutral ZUFO object in the calorimeter of ZEUS detector.

In **Equation 2.22** of **Section 2.9**, the mass of neutral ZUFO object-*i* (assuming that neutral hadrons dissipated its energy in the same manner as photon), is approximated by,

$$mass_i = \sqrt{E_i^2 - (E_i \sin\theta_i \cos\phi_i)^2 - (E_i \sin\theta_i \sin\phi_i\ )^2 - (E_i \cos\theta_i)^2} \qquad (2.22)$$

However, the use of **Equations (2.17), (2.18), (2.19)** to estimate the four-momentum of hadrons in neutral and charge current (NCC) in the final state in the calorimeter of the ZEUS detector [17] and, to calculate the momentum of the scattered positron in a leading neutron in photoproduction [9] and the electron in diffractive DIS tagged with leading proton spectrometer [13] shows that the mass in approximated by **Equation (2.22)** would have significant value especially for neutral hadron in the final state.

In F**igure 6.13** invariant mass of K_L^0 candidates reconstructed from ZUFOs objects not associated with any track but forming islands of energy deposit in the calorimeter of the ZEUS detector, using the **Equation (2.22)**. **Figure 6.7(a)** shows the mass peak around 0.5GeV, which is in good agreement with the invariant K_L^0 mass of 0.498GeV [35].

From F**igure 6.13**, it can be observed that the width peak is quite wide. This is due to the limited variables available for K_L^0 candidate selection i.e. the polar angle θ of ZUFO object-*i*, the ZUFO object-*i* energy , the ZUFOs CAL energy and finally the CAL EMC energy for neutral ZUFOs objects in the calorimeter that were not associated with any track.

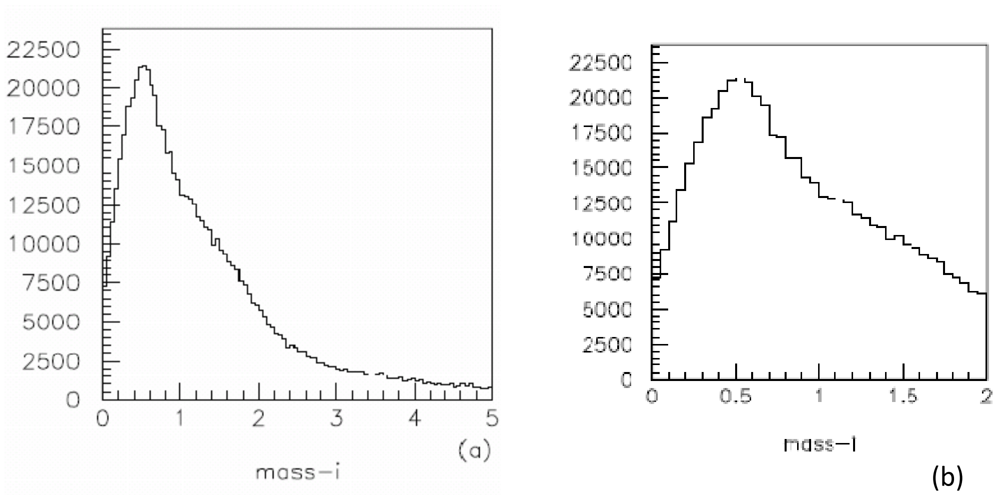

Figure 6.13 (a) Reconstructed mass in GeV of K_L^0 candidates, from ZUFO objects not associated with any tracks (b) an expansion of Figure (a) . The invariant mass of K^0 is 0.498GeV [35]

Figure 6.14 shows invariant mass of K_L^0 candidates with small standard deviation, indicating good statistical sample numbers,

Figure 6.14 gives standard deviation of invariant mass of K_L^0 candidates, showing small error for the reconstructed K_L^0 invariant mass. **Figure 6.15** gives comparison of mass of K_L^0 from Monte Carlo simulation (solid line) against the reconstructed mass (dash line) in GeV on log scale, showing good agreements between both simulated and reconstructed values.

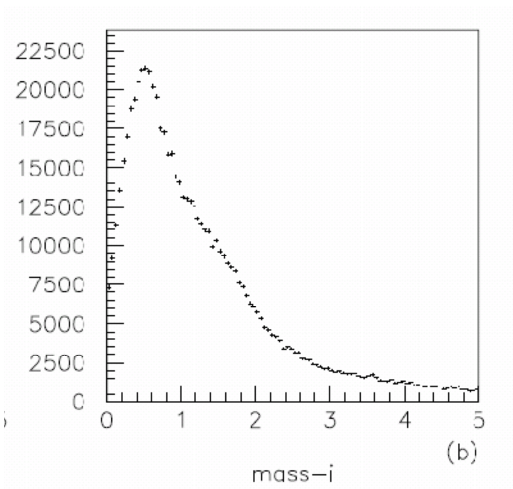

Figure 6.14 Reconstructed mass (in GeV) of K_L^0 candidates with errors. The invariant mass of K^0 is 0.498GeV

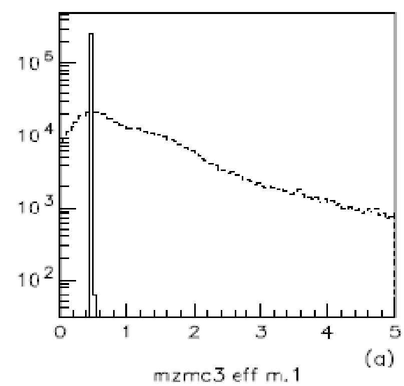

Figure 6.15 Comparison of mass of K_L^0 from Monte Carlo simulation (solid line) against reconstructed mass of K_L^0 candidates (dash line) in GeV on log scale.

Figure 6.16 gives two dimensional plot of mass versus $\cos\vartheta$ of K_L^0 at pseudorapidity $-2 < \eta < 2$, with ϑ as the polar angle of K_L^0, From this figure, it can be seen that the mass K_L^0 came from direction $\cos\vartheta$=0.95 or ϑ=18.2^0.

The pseudorapidity $-2 < \eta < 2$ gave Lorentz transformation of K_L^0 mass in the barrel direction of ZEUS calorimeter, where the mass transformation along the z-axis was invariant.

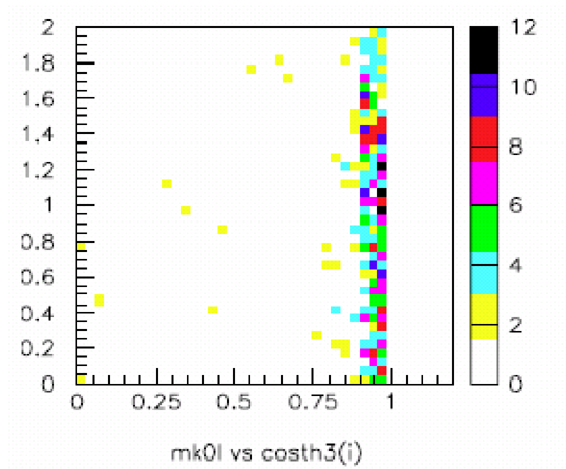

Figure 6.16 (a) Two dimensional plot of mass (GeV) vs $\cos\vartheta$ of K_L^0 at pseudorapidity $-2 < \eta < 2$ (ϑ **as the** polar angle of K_L^0)

6.1.6.1 Cross section of K_L^0

The differential cross section σ of the variable momentum p of K_L^0 candidates, calculated using Equation (5.6) of Section 5.7 in Chapter 5, using integrated luminosity (2006/2007) of 145.90pb^{-1} and branching ratio taken of 34.0% for $\phi(1020) \rightarrow K_L^0\ K_S^0$ decay channel.

Figure 6.17 (a) gives measured momentum of K_L^0 candidates with **Figure 6.17 (b)** giving the measured momentum of K_L^0 candidates that matched in magnitude and direction against the ones from generated from Monte Carlo, while **Figure 6.17 (c)** shows the corrected K_L^0 momentum, with the acceptance as given in **Figure 6.18 (c).**

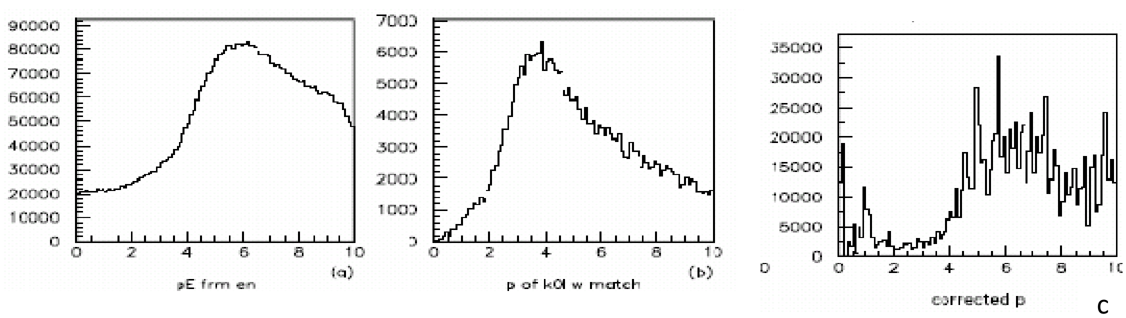

Figure 6.17 Comparison of momentum (in GeV) of K_L^0 candidates (a) measured (b) matched against the ones generated from Monte Carlo and matched against measured momentum; (c) corrected

Figure 6.18(a) and **(b)** give efficiency and the purity of the momentum of K_L^0 candidates with the former peak at ~4GeV while in the latter peak at ~ 5.5GeV. In **Figure 6.19**, the differential cross section with respect to momentum of K_L^0 is given with maximum ~5GeV.

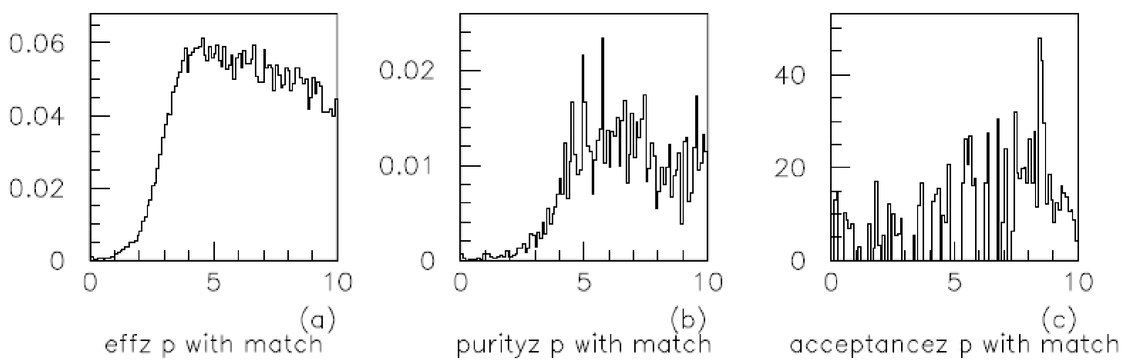

Figure 6.18 Comparison of (a) efficiency vs. energy (in GeV); (b) purity vs. energy (GeV); (c) acceptance vs. energy (GeV) of momentum of K_L^0 candidates

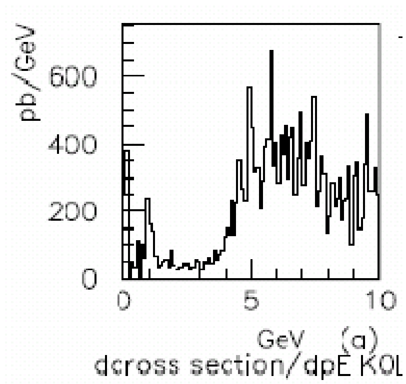

Figure 6.19 Differential cross section (in pb/GeV) of K_L^0 candidates with respect to its measured momentum vs. its energy (in GeV)

6.1.7 Reconstruction of K_S^0 momentum

Figure 6.24 shows the reconstructed momentum of K_S^0 candidates using selection criteria as given in **Section 5.2** of **Chapter 5** for lone hadron from the V0 entries that identified a pair of $\pi^+\pi^-$ potential candidates that decayed from a $K_s^0 \rightarrow \pi^+\pi^-$ channel. In **Figure 6.20a,** the momentum of momentum of K_S^0 from $K_s^0 \rightarrow \pi^+\pi^-$ channel is given, showing a peak ~1GeV, while **Figures 6.20b** to **6.20d** give the momentum components in the direction x, y and z respectively.

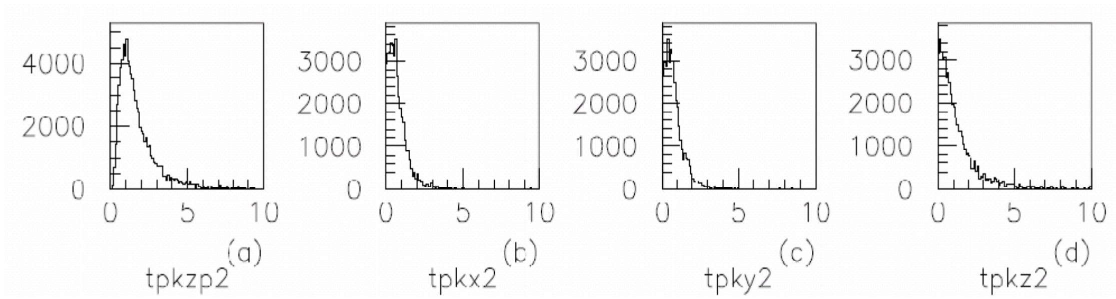

Figure 6.20 Reconstructed momentum (in GeV) of K_S^0 candidates (a) momentum of K_S^0 with (b) in x-direction; (b) y-direction (c) in z-direction

In **Figure 6.21,** two dimensional plot of mass (GeV) versus polar angle $\cos\vartheta$ of K_S^0 at pseudorapidity $-2<\eta<2$ is given, showing polar angle of K_S^0 at 18.2^0 $(Cos\theta = 0.95)$**,** which is in the same direction of K_L^0 as shown previously in **Figure 6.16a.**

These observations indicate that K_S^0 and K_L^0 may not be an exclusive ϕ decay as depicted in **Figure 2.11** of **Chapter 2** in this thesis.

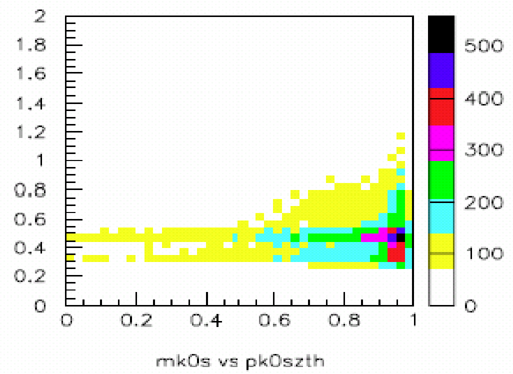

Figure 6.21 Two dimensional plot of mass (GeV) vs $\cos\vartheta$ of K_S^0 at pseudorapidity $-2<\eta<2$ **(**ϑ as the polar angle of K_S^0)

6.1.8 Reconstruction of $\phi(1020)$

In this section, the reconstruction of $\phi(1020)$ mass from the decay channel $\phi(1020) \to K_L^0 K_S^0$ i.e. $m(\phi(1020)) \to m(K_L^0\ K_S^0)$, was carried out by using the reconstructed mass of from K_L^0 from **Section 6.1.6** and the reconstructed mass of K_S^0 from $K_s^0 \to \pi^+\pi^-$ decay channel from lone hadron from the V0 entries of **Section 6.1.7**. The result is given in **Figure 6.22a**.

In **Figure 6.22 (a)** and **(b)**, the reconstruction of $\phi(1020)$ from $m(\phi(1020)) \to m(K_L^0\ K_S^0)$ shows a maximum entries of about 1300 at 1.05GeV, this is in good agreement with the invariant mass of 1.019 GeV [35]. The standard deviation of the reconstructed $\phi(1020)$ mass is small, as indicated by the error bars in the plot in **Figure 6.22c.** However, the limitation of event selection of K_L^0 candidates as described in **Section 6.1.6** contributed to the relatively wide width of the peak in **Figure 6.22a.**

For comparison purposes, the reconstructed masses of K_L^0 and K_S^0 are also given in **Figure 6.23a** and **Figure 6.23b,** while the reconstructed K_S^0 mass narrowed down to $abs(Mass(\pi^+\pi^-) - Mass(K_S^0)) < 0.02\ GeV/c^2$ as given **Section 5.2** of this thesis.

In **Figure 6.24 (a)**, comparison of reconstructed $\phi(1020)$ mass in GeV (dash line) with the mass from Monte Carlo simulation (solid line) is given, showing good agreements between both reconstructed and simulated values.

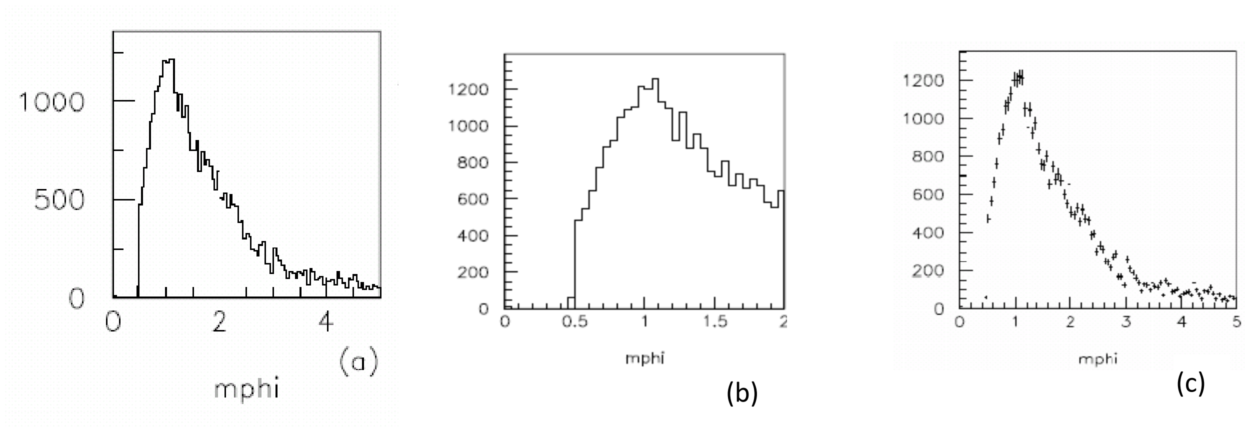

Figure 6.22 Reconstructed mass of $\phi(1020)$ from $\phi(1020) \rightarrow K_L^0 K_S^0$ channel (a) $\phi(1020)$ mass from $m(\phi(1020)) \rightarrow m(K_L^0\ K_S^0)$; (b) an expansion of Figure (a); (c) Statistical error of the reconstructed $\phi(1020)$ mass from $\phi(1020) \rightarrow K_L^0 K_S^0$ channel. The invariant mass of $\phi(1020)$ is 1.019 GeV [35]

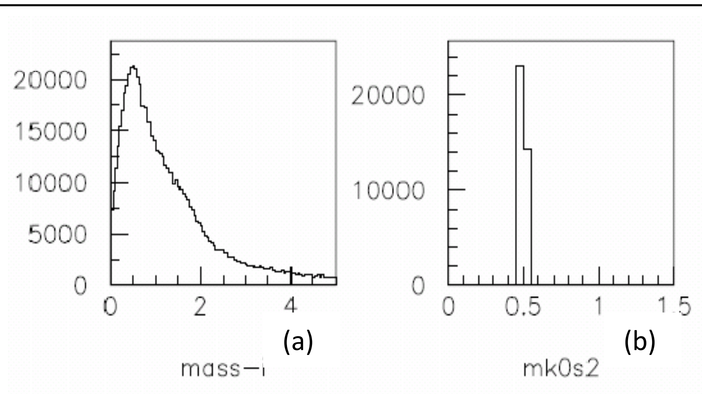

Figure 6.23 Reconstructed masses (in GeV) of (a) K_L^0 candidates using the ZUFOs entries; (b) mass K_S^0 candidates from V0 entries narrowed to $abs(Mass(\pi^+\pi^-) - Mass(K_S^0)) < 0.02$.

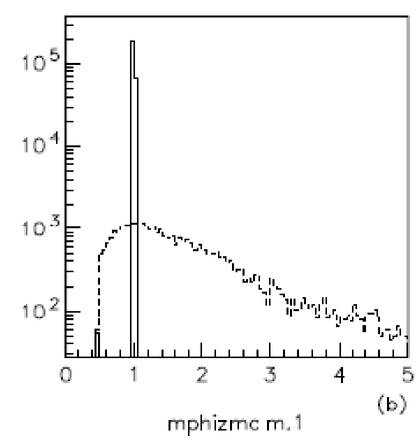

Figure 6.24 Comparison of mass of $\phi(1020)$ reconstructed mass in GeV (dash line) against its mass from Monte Carlo simulation (solid line)

The works by Chekanov et. al. (2001) on inclusive $\phi(1020)$ meson production in neutral deep inelastic scattering at HERA using $\phi(1020)$ reconstructed from $\phi(1020) \rightarrow K^{+}K^{-}$ channel in Breit frame with $10 < Q^{2} < 100 GeV^{2}$ gave $\phi(1020)$ mass 1.016GeV with maximum ~ 4500 entries, which is comparable to the measured mass of $\phi(1020)$ **Figure 6.22** from $\phi(1020) \rightarrow K_{L}^{0}K_{S}^{0}$ channel.

Measurements of $\phi(1020)$ using $\phi(1020) \rightarrow K^{+}K^{-}$ channel from $e^{+}e^{-} \rightarrow K_{L}^{0}K_{S}^{0}$ process from heavy ion collisions by Abelev et. al. (2008) gave invariant mass of $\phi(1020)$ of 1.02GeV/c with $0.8 < p_{T} < 1.2 GeV/c$.

6.1.8.1 Cross section of $\phi(1020)$

Figure 6.25 compares momentum (in GeV) of $\phi(1020)$ candidates, with the **Figure 6.25a** giving the measured momentum ; (b) corrected; (c) simulated from Monte Carlo and matched against measured momentum (in GeV) of $\phi(1020)$ candidates, with **Figure 6.25a** showing the momentum maximum entries ~500. After correction, the entries gain by a factor of 4 as shown in **Figure 6.25b,** with the simulated momentum matched in magnitude and direction against measured momentum showing entries 20 times higher with maximum ~5GeV as in **Figure 6.25c**.

In **Figure 6.26,** the efficiency, purity and acceptance of momentum of $\phi(1020)$ candidates versus its energy (in GeV) are shown. The differential cross section σ with respect to the momentum p of $\phi(1020)$ candidates is given in **Figure 6.27**, calculated using a standard bin-by-bin correction is given in **Equation (6.1).**

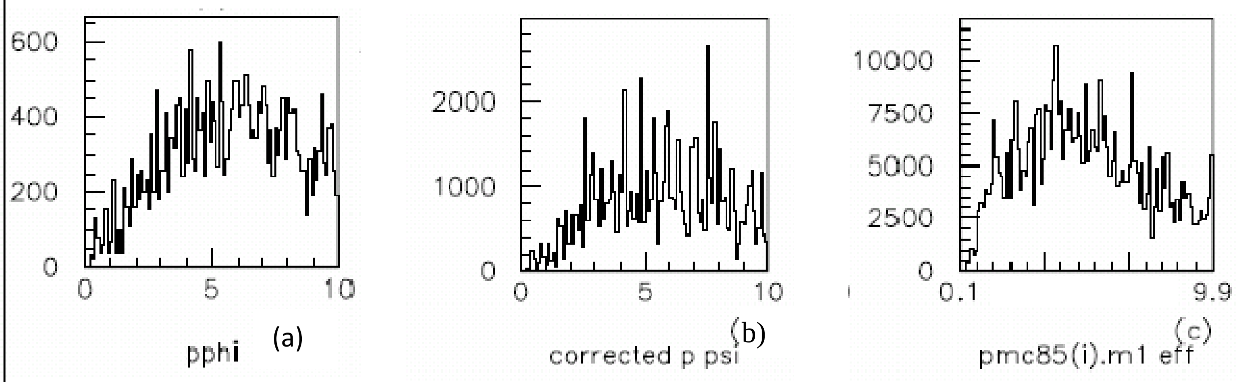

Figure 6.25 Comparison $\phi(1020)$ momentum (in GeV) (a) measured; (b) corrected; (c) simulated from Monte Carlo and matched in against measured momentum

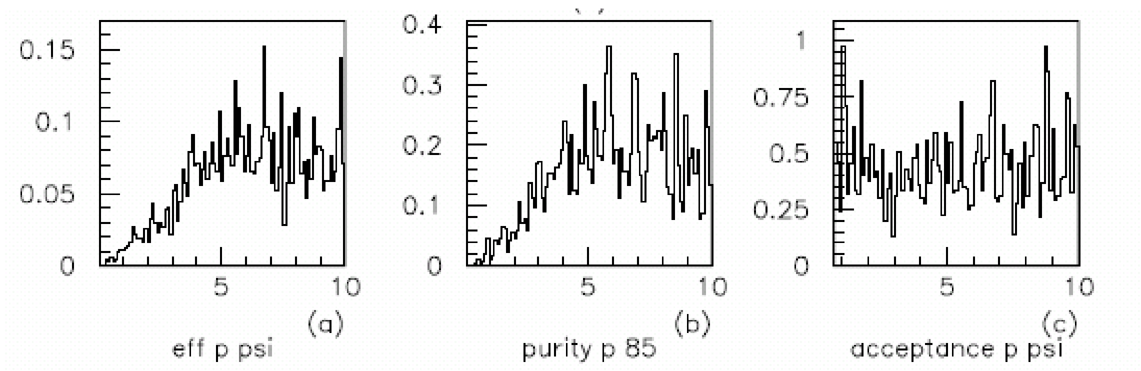

Figure 6.26 Comparison of (a) efficiency; (b) purity; (c) acceptance of momentum of $\phi(1020)$ candidates versus energy (in GeV)

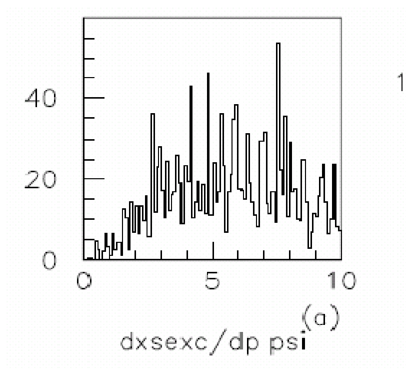

Figure 6.27 Differential cross section (in pb/GeV) of $\phi(1020)$ candidates with respect to its measured momentum vs its energy (in GeV)

6.1.8.2 Correlation of $\phi(1020)$ with polar angles with K_L^0 and K_S^0

In the exclusive ϕ production with decay channel $\phi \to K_L^0 K_S^0$, the momentum conservation requires that K_L^0 and K_S^0 to be in the opposite direction, as shown in **Figure 2.11** of **Chapter 2.** But **Figure 6.16** and **Figure 6.21** show that both K_L^0 and K_S^0 moving in the same direction at $\cos\vartheta$ = 0.95 or $\theta = 18.2^0$, thus indicating the measured ϕ an inclusive event .

Figure 6.28 shows cosine azimuthal angle $\cos\vartheta$ of $\phi(1020)$ peaking at $\cos\vartheta$ = 0.7 $(\theta = 45.6^0)$ and near $\cos\vartheta$ ~ 1. **Figure 6.29** shows two dimensional plot of mass $\phi(1020)$ (GeV) versus $\cos\vartheta$ of K_L^0 of at pseudorapidity $-2 < \eta < 2$, while **Figure 6.30** shows the similar plot for mass $\phi(1020)$ (GeV) versus $\cos\vartheta$ of K_L^0.

In **Figure 6.29**, the peaks occur at azimuthal angle of K_L^0 at $\cos\vartheta$=0.75 and $\cos\vartheta$ =0.95 indicating possible correlation between $\phi(1020)$ and K_L^0 in the direction of $\cos\vartheta$ = 0.7 $(\theta = 45.6^0)$.

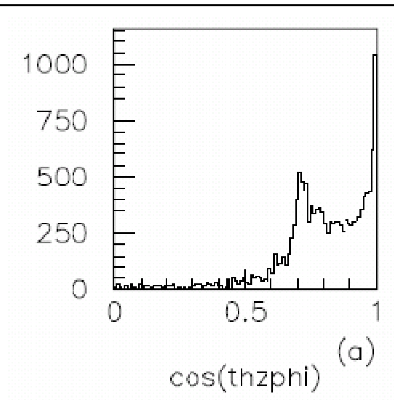

Figure 6.28 Cosine polar angle $\cos\vartheta$ of $\phi(1020)$

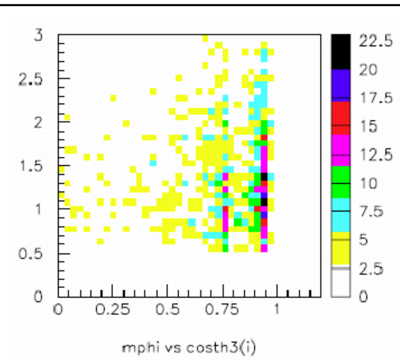

Figure 6.29 Two dimensional plot of mass $\phi(1020)$ (GeV) vs $\cos\vartheta$ of K_L^0 at pseudorapidity $-2 < \eta < 2$ (ϑ as the polar angle K_L^0)

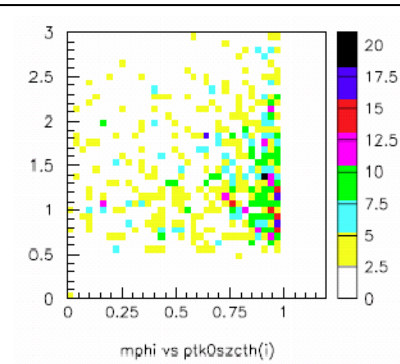

Figure 6.30 Two dimensional plot of mass $\phi(1020)$ (GeV) vs $\cos\vartheta$ of K_S^0 at pseudorapidity $-2 < \eta < 2$ (ϑ as the polar angle of K_S^0)

Figure 6.31 shows projection of K_L^0 mass (in GeV) versus $\phi(1020)$ mass (in GeV) using the ZUFOs method that uses islands of energies that was not associated with any track, while **Figure 6.32** shows projection of K_L^0 mass (in GeV) versus $\phi(1020)$ mass (in GeV) using the tracking method from CTD entries [27].

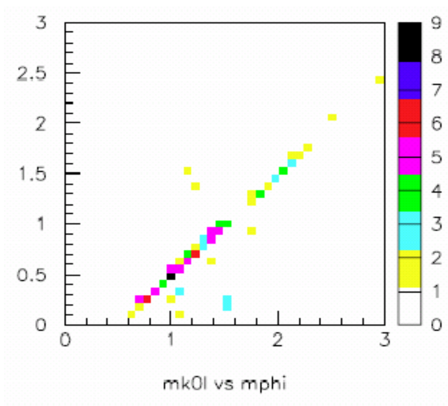

Figure 6.31 Two dimensional plot of K_L^0 mass (in GeV) vs. $\phi(1020)$ mass (in GeV)

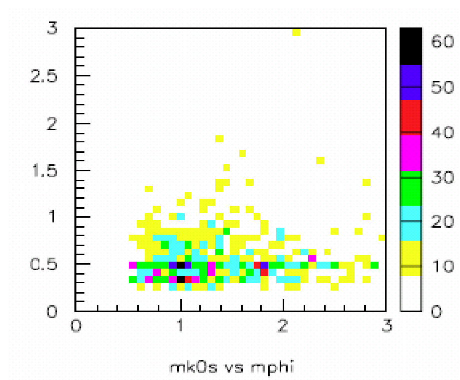

Figure 6.32 Two dimensional plot of K_S^0 mass (in GeV) vs. $\phi(1020)$ mass (in GeV)

6.2 Production of Λ from $\Lambda \rightarrow n\pi^0$ channel

In **Section 5.6**, the selections of n and $\gamma\gamma$ from π^0 decay and the reconstruction of Λ^0 mass from n and π^0 masses have been described. In this section, the result from these cuts that gave kinematic variables of n and $\gamma\gamma$, finally the reconstructed mass of Λ^0 from n and π^0 masses.

In this section, the result from grand reprocessing Monte Carlo from Pythia simulation data (DijetLF067p_GR**)** was used with the results given and discussed in the following sections.

6.2.2 Background cuts

As in **Section 6.1.2**, the background cuts was carried out energy plot after undergoing event selections as given in **Section 5.1,** with the background signal (dash line) i.e. when the ratio of electromagnetic to hadronic energy of potential neutron candidates was less than 1 % . **Figure 6.33** shows out energy plots of potential neutron candidates mixed with background (solid line) and the background alone (dash line). **Figure 6.33b** shows the background fitted with function $e^{a+b*zufo(4,i)}$ (*a* and *b* as constants and Zufo(4,*i*) as the energy of object-*i*) and later subtracted from mixed plot in **Figure 6.33a.**

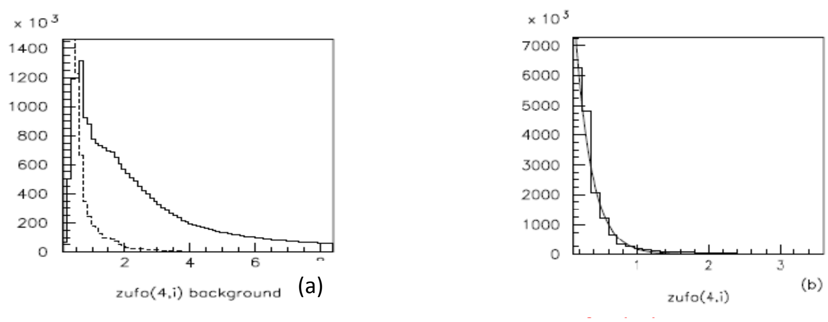

Figure 6.33 Comparison of ZUFOs energy $zufo(4,i)$ (in GeV) for object-*i* not associated with any track (solid line) against its background signal (dash line) for neutron candidates; (b) the background signal is curve fitted using function $e^{(a+b*zufo(4,i))}$ and is then used to isolate the ZUfOs energy of K_L^0 candidates from its background signal.

6.2.3 The four-momenta of neutron candidates

After background cut using the curve fit as given in **Figure 6.33 (b)**, the energy of the neutron candidates from ZUFOs object not associated with any track is given in **Figure 6.34(a)**, showing a peak at 6GeV. As with in **Section 6.1.3**, the momentum in x, y, z components as in **Figure 6.34(b), (c)** and **(d)** would only be used to calculate cosine polar angle $\cos\theta$ and cosine azimuthal angle $\cos\phi$ for neutron candidates as these values were calculated using pion mass.

was used with the results given and discussed in the following sections

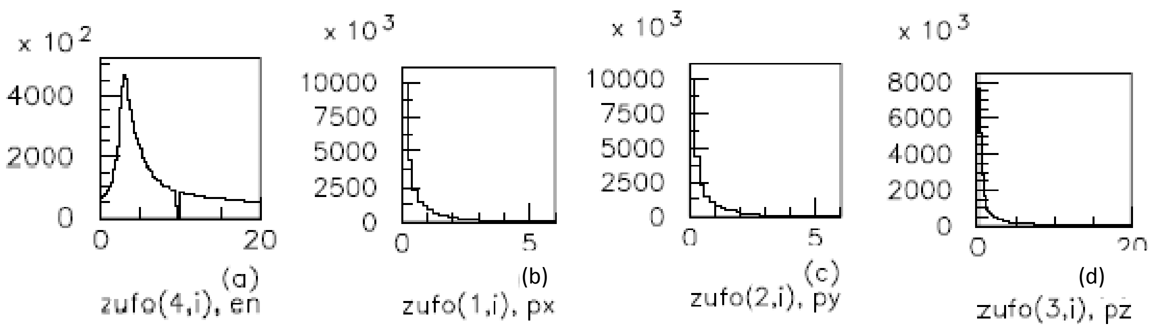

Figure 6.34 Four-momentum (in GeV) from ZUFOs entry for object-i not associated with any track used in neutron reconstruction (a) Energy component (b) x-component (c) y-component (d) z-component

In **Section 2.9** of this thesis, the kinematic variables of the ZUFO objects in the calorimeter of the ZEUS detector were described, with the momentum components in x, y, z direction, in terms of energy E azimuthal angle θ and polar angle ϕ, as given in **Equations (2.17), (2.18) and (2.9)**.

Figure 6.35 shows the momentum of neutron candidates from ZUFOs object-i that was not associated with any track in the calorimeter of the ZEUS detector, calculated using **Equations (2.17),(2.18)** and **(2.19)** after event selection as given in **Section 2.9** of **Chapter 2**. The neutron momentum in **Figure 6.35a** shows a peak at 3.5GeV while its z-component peaks at 3GeV **Figure 6.35d,** with no significant x and y components**.** This indicates the tendency of neutron candidates to move in the forward direction.

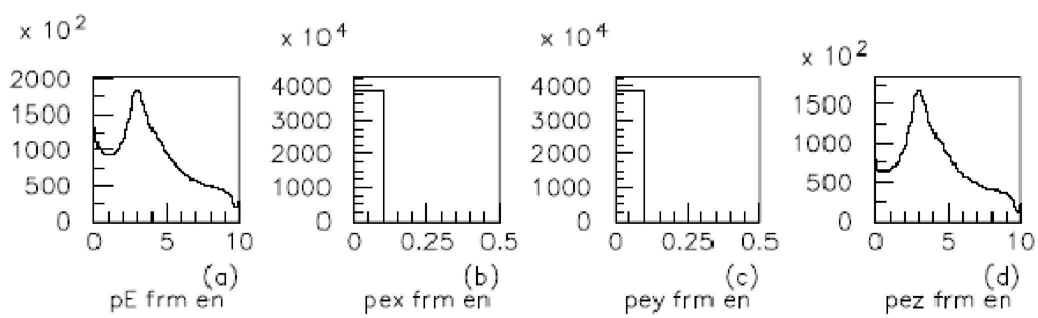

Figure 6.35 Reconstructed four-momentum (in GeV) of neutron candidates (a) Energy component (b) x-component (c) y-component (d) z-component

In **Figure 6.36a,** the measured cosine polar angle $\cos\theta$ of neutron candidates is given, with the maxima appears to be at ~ 1 (0^0) and 0.75 (41^0). **Figure 6.36b** shows $\cos\theta$ of neutron candidates from Monte Carlo simulation with the momentum matched against its measured value. Both **Figure 6.36a** and **Figure 6.36b** show similar trend but in the former there is additional peak at 0.75 (41^0).

As in **Section 6.1** of this chapter, energy component as given in **Figure 6.34a** and the polar angle from **Figure 6.36a** would be later used to reconstruct of kinematic variables of K_L^0 with the results as given in the following sections.

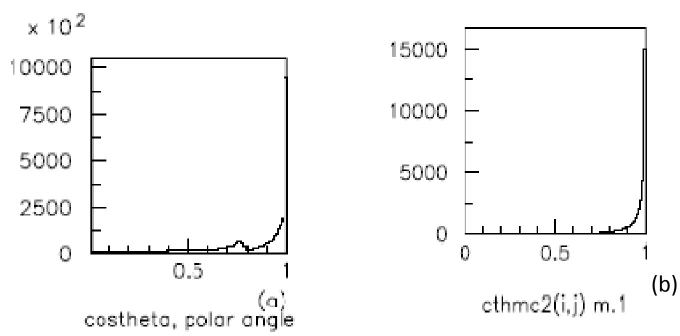

Figure 6.36 Cosine polar angles of K_L^0 candidates
(a) measured $\cos\theta$ and (b) $\cos\theta$ from Monte Carlo simulation.

6.2.4 Kinematic variables of neutron

Figure 6.37 gives the properties of reconstructed neutron candidates, with **Figure 6.37a** showing narrow width of $\delta_i = E_i - p_{zi}$ distribution for neutron candidates, indicating small difference between its energy and momentum in the z-component.

The centre of mass $W_{JB} = \sqrt{y_{JB}\ s}$, for the intermediate boson-proton for neutron candidates as in **Figure 6.37b** has a peak at about 25 GeV while the pseudorapidity is as in **Figure 6.37c**, indicating the highest production of neutron in the region $0 < \eta < 0.8$ in the forward region, as indicated by its momentum in z-component as in **Figure 6.35d.**

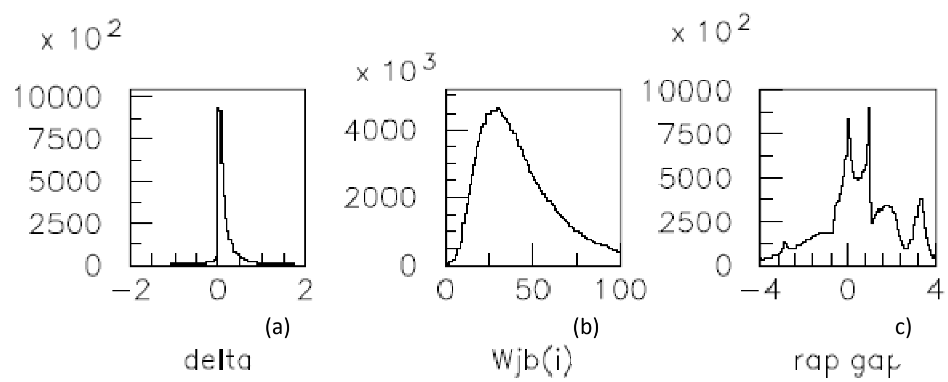

Figure 6.37 Properties of reconstructed neutron candidates (a) $\delta_i = E_i - p_{zi}$ (in GeV); (b) centre-of-mass $W_{JB} = \sqrt{y_{JB}\ s}$ for the intermediate boson-proton; (c) pseudorapidity η

6.2.5 Reconstructed mass of neutron

Figures 6.38a and **6.38b** gives the neutron mass constructed using selection criteria as described in **Section 5.1** of **Chapter 5**. The mass neutron candidates peak at 0.9GeV, which is in good agreement the invariant neutron mass of 0.939 GeV [35]. As in **Section 6.1.6**, the observed wide width peak is due to limited to only four variables available for neutron candidate selections i.e. polar angle θ, energy of object-*i* Zufos(4,i), and CAL and CAL EMC energies for neutral ZUFOs objects in the calorimeter that were not associated with any track.

Figure 6.38c gives the statistical error for the mass of neutron candidates, showing good standard deviation. In **Figure 6.38d,** the neutrons from Monte Carlo simulation is given, showing lower events then measured ones, perhaps to due to existence of background signals (and other neutron source from direct interactions) near the beampipe of the ZEUS detector.

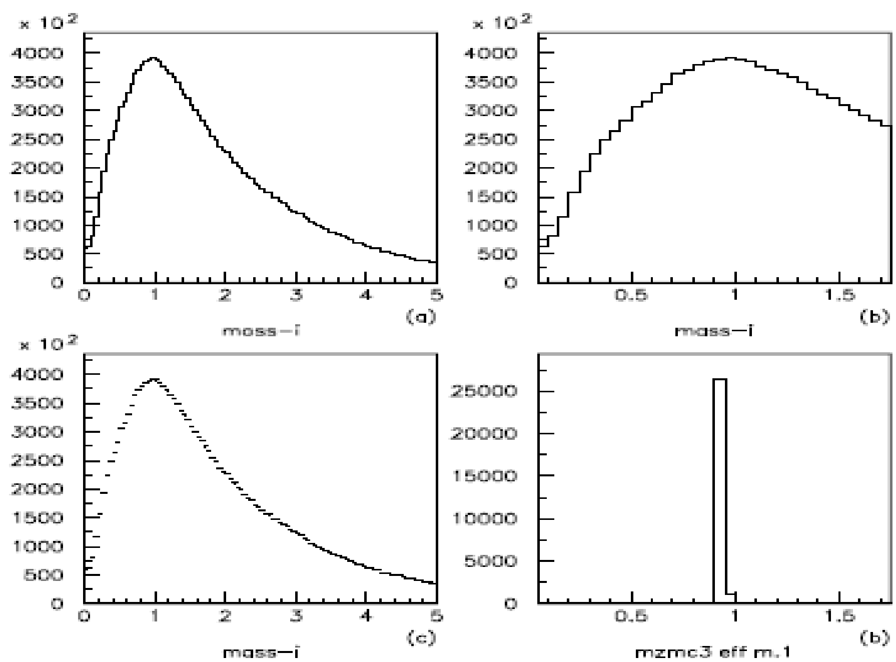

Figure 6.38 Reconstructed mass of neutron candidates in GeV (a) mass of neutron constructed from ZUFO objects not associated with any track; (b) an expansion of Figure (a); (c) neutron mass with errors; (d) neutron from Monte Carlo simulation. The invariant mass of neutron is 0.939GeV [35].

6.2.5.1 Neutron azimuthal angle

In **Figure 6.39,** two dimensional plot of neutron mass (in GeV) versus its polar angle θ is given, showing neutron direction at 0.2 radian (11.5^0) and consistent with observation in **Figure 6.36a.**

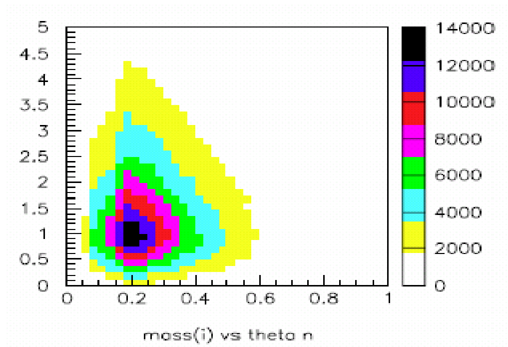

Figure 6.39 (a) Two dimensional plot of neutron mass (GeV) vs polar angle θ (rad) of neutron

6.2.5.2 Differential cross section of neutron

The differential cross section σ of neutron candidates with respect to its variable momentum p, was calculated using **Equation (5.6)** from **Section 6.1.6.1,** with integrated luminosity (2006/2007) of L =145.90pb^{-1} and B as the branching ratio 35.5% for $\Lambda \rightarrow n\,\pi^0$ decay channel.

Figure 6.40 compares the momentum of the measured (**Figure 6.40a)**, matched in magnitude and direction against the ones from generated from Monte Carlo (**Figure 6.40b**) and the corrected neutron candidates (**Figure 6.40c)**, while **Figure 6.41** shows the efficiency, purity and acceptance for momentum of neutron candidates. In these figures, except for **Figure 6.40c** that shows noise signal at momentum range <0.5GeV, the peaks occurred at ~3GeV, indicating that neutron production highest at around this peak.

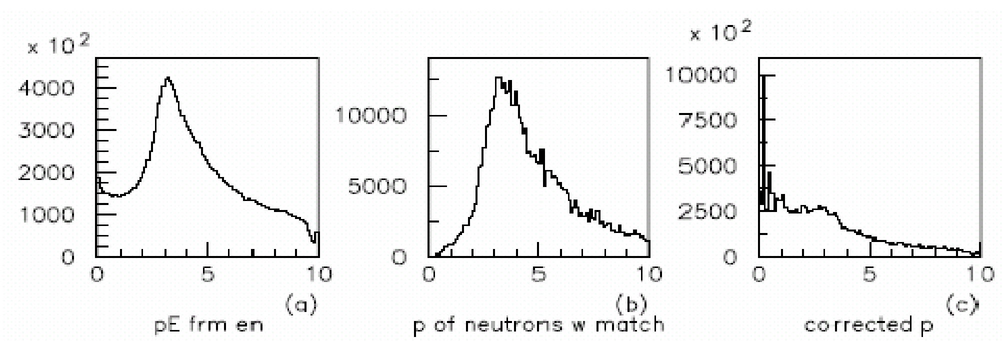

Figure 6.40 Comparison of momentum of neutron candidates (a) measured (b) matched in magnitude and direction against the ones from generated from Monte Carlo; (c) corrected

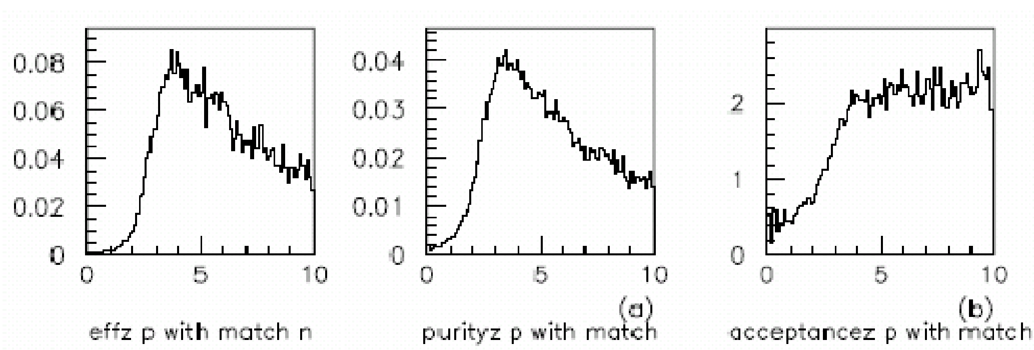

Figure 6.41 Comparison of (a) efficiency; (b) purity; (c) acceptance of momentum of neutron candidates

In **Figure 6.42**, the differential cross section with respect to momentum of neuron candidates showing similar in trend to the corrected momentum in **Figure 6.40(c),** a peak $d\sigma / dp$ ~5000pb/GeV at neutron energy ~3.5GeV. (At <0.5GeV range, there appeared to be noise signals in the differential cross section).

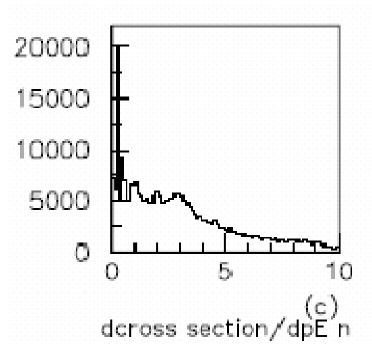

Figure 6.42 Differential cross section (in pb/GeV) of neutron candidates with respect to its measured momentum (in GeV)

6.2.6 Reconstruction of $\pi^0 \to \gamma\gamma$ candidates

To reconstruct the Λ mass from $\Lambda \to n\pi^0$, the π^0 candidates were reconstructed from $\gamma\gamma$ candidates from $\pi^0 \to \gamma\gamma$ decay channel using the selection criteria as given in **Section 5.4** of **Chapter 5**.

The momentum for the reconstructed $\gamma\gamma$ candidates is given in **Figure 6.43**, showing the z-component as having peak at 3GeV as in **Figure 6.43a**, as compare to the momentum of $\gamma\gamma$ candidates with a peak at 3.5GeV as in **Figure 6.43a,** indicating the tendency of $\gamma\gamma$ candidates to move in the forward direction.

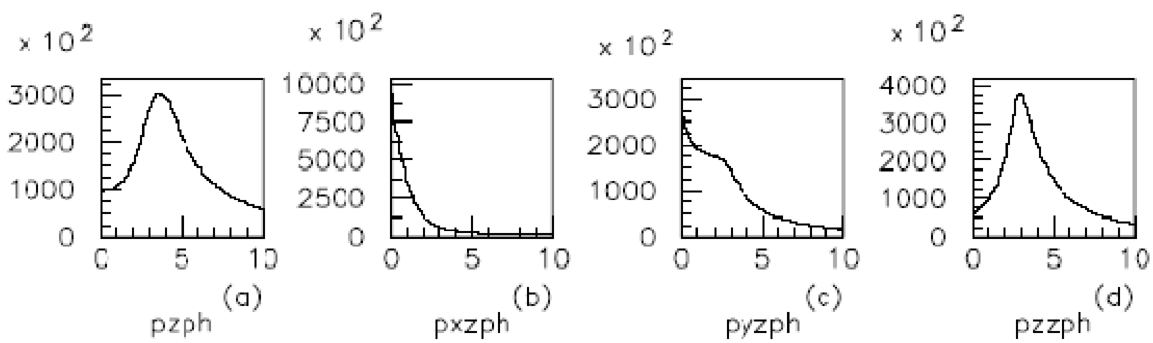

Figure 6.43 Reconstructed momentum (in GeV) of $\gamma\gamma$ candidates from $\pi^0 \to \gamma\gamma$ decay channel (a) momentum (b) momentum in x-direction (c) momentum in y-direction (d) momentum in z-direction

Figure 6.44a shows reconstructed mass of π^0 from $\pi^0 \rightarrow \gamma\gamma$ decay channel, while **Figure 6.44b** gives the energy of $\gamma\gamma$ candidates peaking at 3.5GeV. In **Figure 6.44c** the transverse energy of $\gamma\gamma$ is shown. **Figure 6.44a** shows the energy distribution of $\gamma\gamma$ candidates peaking at 3.5GeV, while the **Figure 6.44a** shows the peaking of polar angle $\theta \sim 14^0 (0.25rad)$ of $\gamma\gamma$ candidates indicating the direction π^0 to be at $\theta \sim 14^0 (0.25rad)$.

The reconstructed π^0 mass should be between $0.133 < \sqrt{E_{\gamma\gamma}^2 - p_{\lambda\gamma}^2} < 0.137\ GeV/c^2$ to narrow down the photon candidates that actually contributed to π^0 mass.

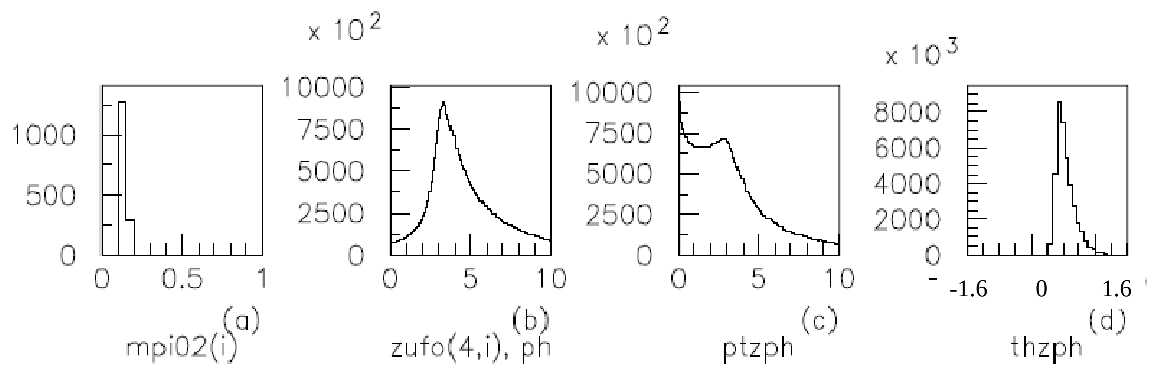

Figure 6.44 Properties of $\pi^0 \rightarrow \gamma\gamma$ candidates: (a) mass of π^0 in GeV narrowed to $0.133 < \sqrt{E_{\gamma\gamma}^2 - p_{\lambda\gamma}^2} < 0.137\ GeV/c^2$; (b) $\gamma\gamma$ energy (in GeV); (c) $\gamma\gamma$ transverse momentum in (GeV); (c) $\cos\theta$ polar angle of $\gamma\gamma$

6.2.7 Reconstruction of Λ

The reconstruction of Λ mass from $\Lambda \rightarrow n\,\pi^0$ decay channel was carried out using $m(\Lambda) \rightarrow m(n\,\pi^0)$. In **Section 6.2.5** of this chapter, the reconstruction of the neutron candidates is given, while in **Section 6.2.6** the result from event selection of π^0 using selection criteria as given in **Section 5.4** of **Chapter 5,** is given. From these event selections, the reconstruction of Λ mass from $\Lambda \rightarrow n\pi^0$ channel has been carried out, with the result as shown in **Figure 6.45.**

In **Figure 6.45a** and **6.45b,** the of Λ mass reconstructed from $\Lambda \rightarrow n\pi^0$ channel is shown, with peak at 1.1GeV which is in good agreement with the invariant mass 1.115 GeV [35]. The standard deviation of the reconstructed Λ mass has small error bars as given in **Figure 6.45c**, indicating good statistical sampling. For comparison purpose, the Λ mass from Monte Carlo simulation is also given in **Figure 6.45 (d).** The high entries of the measured Λ mass as compared with the simulated values indicate that the event selection needs further improvement.

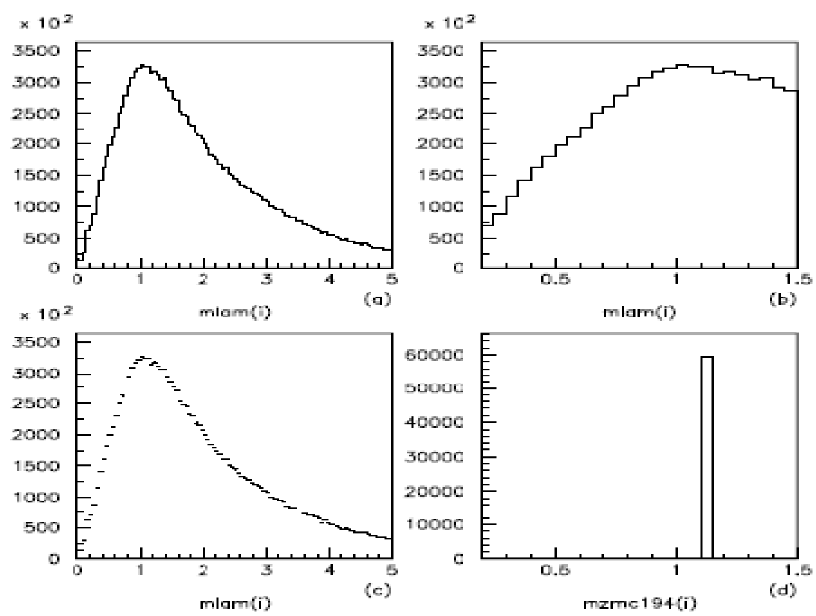

Figure 6.45 Reconstruction of Λ mass (in GeV) from $\Lambda \rightarrow n\pi^0$ channel (a) mass of Λ constructed from $m(\Lambda) \rightarrow m(n\,\pi^0)$ (b) an expansion of Figure (a); (c) Λ mass with errors (d) Λ from Monte Carlo simulation. The invariant mass of Λ is 1.115 GeV [35].

6.2.7.1 Differential cross section of Λ

Figure 6.46 compares momentum (in GeV) of Λ candidates, with **Figure 6.46a** giving the measured momentum, **Figure 6.46b** the corrected momentum and. **Figure 6.46c** simulated momentum from Monte Carlo that was matched in magnitude and direction against its measured momentum. In **Figure 6.46(a),** the momentum peaks at ~7GeV**,** with **Figure 6.46(b)** showing maximum at about the same value but with entries ~500.

In **Figure 6.47,** the efficiency, purity and acceptance of momentum of Λ candidates versus its energy (in GeV) are shown, with the efficiency and purity reaching maximum at ~ 7GeV.

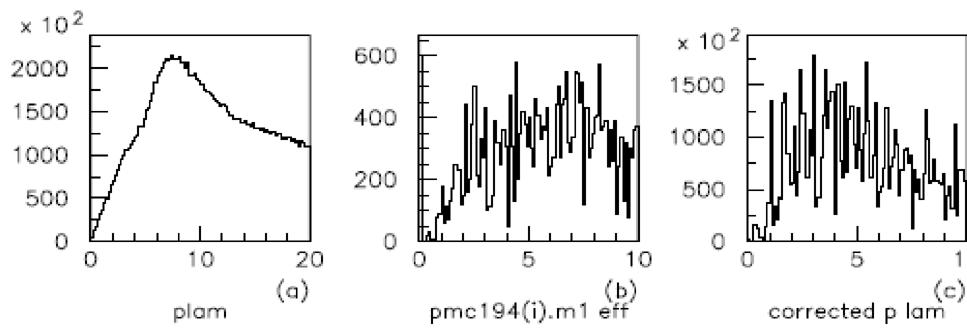

Figure 6.46 Comparison $\phi(1020)$ momentum (in GeV) (a) measured; (b) corrected; (c) simulated from Monte Carlo and matched in against measured momentum

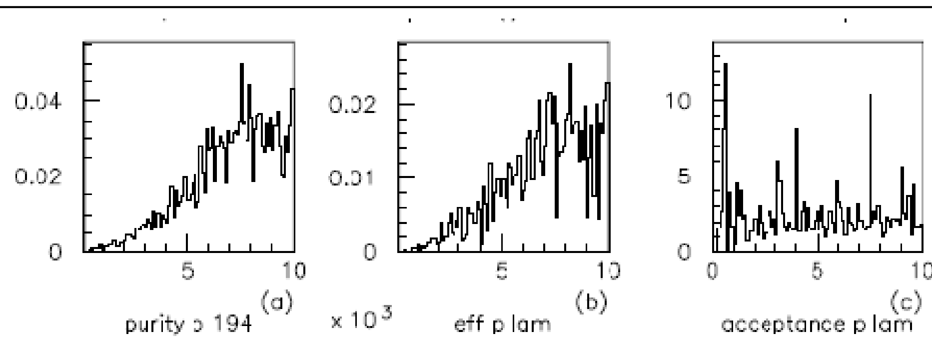

Figure 6.47 Comparison of (a) purity (b) efficiency; (c) acceptance of momentum of Λ candidates versus energy (in GeV)

The differential cross section σ with respect to the momentum p of Λ candidates is given in **Figure 6.48**, calculated using a standard bin-by-bin correction is given in **Equation (5.6)** of this chapter. In this figure, the maximum $d\sigma / dp$ ~15000pb/GeV at ~3.5GeV similar in trend to the corrected momentum in **Figure 6.46(c).**

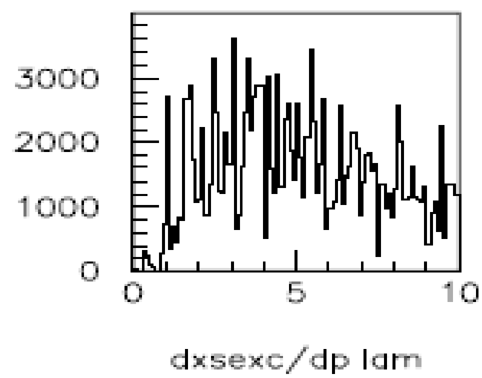

Figure 6.48 Differential cross section of neutron candidates with respect to its measured momentum (pb/GeV) vs its energy (in GeV).

6.4 Summary

In this chapter, the reconstruction of vector meson $\phi(1020)$ was carried out using the $\phi(1020) \rightarrow K_L^0\ K_S^0$ channel and the reconstruction of baryon Λ through the decay channel $\Lambda \rightarrow n\,\pi^0$.

Using the selection criteria in **Chapter 5**, the candidates of long live neutral hadrons K_L^0 and neutron that reached the hadronic calorimeter (HACs) of the ZEUS detector was selected from the uncharged ZUFO objects not associated with any track that formed islands of energy deposits in the HACs.

In both K_L^0 and neutron, their momentum momentums were prominent in the z-direction than in x and y direction, more so for neutron. For K_L^0, the energy deposited in the calorimeter peaked at 5GeV, while for neutron the energy peaked at 6GeV. The small energy range of K_L^0 and neutron that reached the calorimeter suggest that their production were from on-mass-shell hadrons. In the string-fragmentation scheme, a $q\bar{q}$ pair may be created from the vacuum when the string between two color partons provided that the invariant mass of the string pieces exceed on-mass-shell hadrons.

The Vector Meson Dominance (VDM), as described in **Section 2.6**, postulated a scattering of virtual photon from the irradiation of incoming electron, could acquire a hadronic structure that allows it to fluctuate into the hadron target during *ep* interaction, and coupled to a to a bound $q\bar{q}$ state that have the same quantum number as the photon and caused the vector meson (ρ, ω, ϕ) fluctuations, and scattering elastically off the incoming proton via a pomeron exchange. The SU(3) in the proton structure that transformed the gluons in the proton into hadron $\phi(1020)$ with an $s\bar{s}$ state when virtual photon coupled to a bound $q\bar{q}$ state of the proton was modeled by Color Dipole Moment (CDM), that assumed the $q\bar{q}$ pair as as radiation of color dipole between the quark q and antiquark $\bar{q}$ pair. In case of $\phi(1020) \rightarrow K_L^0\ K_S^0$ decay channel, the state of $s\bar{s}$ in $\phi(1020)$ is partially retained in K_L^0 ($d\bar{s}$) with momentum higher than K_S^0 ($d\bar{s}$).

In the Lund String Model as given in Section 2.4, the hadronisation of quarks and gluons to form hadrons during *ep* interacton involves the fragmentation of color flux sring-like gluons that are binding the quarks and antiquarks ($q\bar{q}$) in hadrons. Fragmentation of hadron Λ with state uds into n (udd) and π^0 ($u\bar{d}$) is possible if the energy stored in the string is sufficient enough as when two color partons move apart, to form a $q\bar{q}$ pair from the vacuum.

In case of decay $\Lambda \rightarrow n\,\pi^0$ channel, the conservation of strangeness number S = -1 through where charges of both mother and decay products were conserved. Using the selection criteria as given in **Section 5.1**, the momentum of neutron peaked at ~3.0GeV while the momentum of $\gamma\gamma$ from π^0 decay peaked at ~3.8GeV indicate that the production of n and π^0 as a result from on-mass-shell hadrons.

CHAPTER 7

CONCLUSION AND FUTURE OUTLOOK

7.1 Conclusion

In this thesis, the methodology of using neutral energy deposits in the calorimeter of the ZEUS detector to reconstruct the long-lived neutral hadrons in the final states, i.e. K_L^0.and neutron, has been explored with successful results. This could be seen from invariant mass of both K_L^0 and neutron constructed using the method in this thesis, including the constructed invariant mass of $\phi(1020)$ from $\phi(1020) \rightarrow K_L^0 K_S^0$ decay channel and mass Λ from $\Lambda \rightarrow n\pi^0$ decay channel, that showed good agreement with the standard invariant mass [35].

The algorithm for halomuon identification in the ZEUS detector has been carried out showing good results. This algorithm could be implemented for endcap energy calibration of a detector and to remove halomuons from background reading of a physics event in high energy physics experiment.

The development of FPGA-based read-out control (ROC) for calorimeter ZEUS detector including the hardware has been carried, as part of the project. The integration of four controlling modules ROC on a single FPGA chip has been shown to be feasible, while the PCB for ROC hardware implementation needs further improvement to increase its performance.

7.2 Future Outlook

The use the energy deposits in the hadronic calorimeter for particle identification could further be explored for finding other long-live neutral and charged particles with decay length comparable to the dimension of the calorimeter. The selection criteria could further be improved by making more variables to be associated with the neutral energy deposits by neutral particles in the calorimeter and could be backtracked to Central Tracking Detector (CTD) vertex to provide more information on the neutral particle trajectory and its origin.

The implementation of the FPGA-based read-out control (ROC) for a calorimeter on a single FPGA chip for new data-taking system is very convenient for its compactness, and easier to improve software design.

BIBLIOGRAPHY

1. C-Peter Fagerstroem; Leading neutron production in Deep Inelastic Scattering at HERA; PhD thesis, University of Toronto, 1999
2. Niels Tuning; Proton Structure at HERA; PhD thesis, University of Amsterdam; 2001
3. Claudia Glasman; Jet Production at HERA with the ZEUS Detector: Resolved and Direct Process in Photoproduction and the Gluon Content of the Proton and the Photon; PhD thesis; Wiezmann Institute of Science, Rehovot, Israel, April 1995
4. Gennady M. Baskin; Diffractive Dissociation in ep Deep Inelastic Scattering; PhD thesis; Tel Aviv University, June 1998
5. T.E. Danielson; A Measurement of Multijet Production in Low-x_{Bj} Neutral Current Deep Inelastic Scattering with ZEUS at HERA; PhD thesis; University of Winsconsin - Madison (UM Lab)
6. M. Riveline; Probing the Parton Evolution in DIS at Low X_{BJ} Using Jet Observables; PhD thesis; McGill University, 1998, DESY-Thesis 1999-005 (pg 79)
7. C. Liu; Neutral Strangeness Production with the ZEUS Detector at Hera; McGill University, Montreal; PhD thesis 2007; DESY-THESIS-2007-036
8. H1 Collaboration; Measurement of $F_2^{c\bar{c}}$ and $F_2^{b\bar{b}}$ at Low Q^2 and x Using the H1 vertex detector at HERA; DESY; DESY 05-110 hep-ex/0507081 July 2005, ISSN 0418-9833.

9. M. Khakzad, Measurements of Dijet Cross Sections with a Leading Neutron in Photoproduction at HERA, PhD Thesis York Universiti, Ontario Dec 1999 DESY-Thesis-2000-008 February 2000

10. D.V. Gorbatkov, V.P. Kryuchkov, Space Energy of Radiation Components Behind High Energy Accelerator Shielding; Institute of High Energy Physics, Protvino, Moscow Region, Russia, (1983)

11. Niels Tuning, ZUFOs: Hadronic Final Sate Reconstruction with Calorimeter, Tracking and Backsplash Correction; NIKHEF/University of Amsterdam, ZEUS-01-021 June 27th 2001

12. V. Adler, Optimising of Design Parameters of the TESLA Vertex Detector and Search for Events with Isolated Leptons and Large Missing Transverse Momentum with ZEUS-Experiment (HERA-II), PhD Thesis Unversity of Hamburg, DESY-Thesis-2006-012 June 2006

13. Rico Wichmann, Properties of the Hadronic in Final State in Diffractive Deep Elastic Scattering Tagged with the Leading Proton Spectrometer of ZEUS; PhD Thesis Uiversity of California, Dec 1999, DESY-Thesis-2000-015 April 2000

14. Zeus Collaboration, Measurement of Neutral Current Cross Sections at High Bjorken-x with the ZEUS Detector at HERA, DESY 06-116 hep-ex/0608014 July 2006 (pg6), Lab UM

15. A. Gabareen Mokhtar, Study of Neutral and Charged Current Cross Sections at High Q^2 at HERA, DESY-Thesis-2006-005 January 2006, Tel Aviv University (pg 35)

16. Reference Zeus Collaboration, Neutral Strange Particle Production in Deep Inelastic Scattering at HERA, Zeus Collaboration, ESY 95-084 April 1995

17. P.D. Ryan, Photoproduction of Events with Rapidity Gaps between Jets with ZEUS at HERA, PhD thesis, University of Wisconsin, Madison, 2006, DESY –THESIS-2006-030 Nov 2006

18. Henning Raach, Inclusive Jet Cross Sections in Neutral Current Deep Inelastic Scattering in the Breit Frame at ZEUS, PhD thesis, Albert-Ludwigs-Universitat, Jun 2001

19. Jan R. Okransinski, Measurements of Hadronic Final State in Deep Inelastic Scattering at HERA, PhD thesis, Pennsylvania State University, Aug 1999 (*file jokras.ps)*

20. Monica Luisa Vazquez Acosta, Jet production in charged current deep inelastic scattering at HERA, PhD thesis, Universidad Autonoma de Madrid, 16 Dec 2002,

21. Halina Abromowicz, Allen Caldwell, HERA Collider Physics, May 22, 2006, submitted to Reviews of Modern Physics

22. F.J. Gilman[1], K Klienknecht[2], B. Renk[2], The Cabbibo-Kobayashi-Maskawa Quark-Mixing Matrix, [1]Carnegie-Mellon University, [2]Johannes-Gutenburg Universitat Mainz, January 2004

23. (??),Introduction to High-Energy Heavy-Ion Collision, Chap 2.4 pg 24

24. Joost Herman Vossebeld, Dijet Photonproduction at High Transverse Energies, Universitiet van Amsterdam, Sept 1999

25. Halina Abramowicz, Allen Caldwell, HERA Collider Physics, May 22, 2006, submitted to Review of Modern Physics

26. Y.F. Wang,V. Balic, G. Gratta,A, Fassim, S. Roesler, A, Ferari, Predicting neutron production from cosmic-ray muons, Physical Review D. Volume 64,013012

27. Grenndy M. Briskin, Diffractive Dissociation in ep Deep Inelastic Scattering, PhD thesis, Tel Aviv University, June 1998

28. S. Chekanov, B. Levchenko, J. Repond; Inclusive φ(1020)-meson production in neutral current deep inelastic scattering at HERA; Zeus-Note 01-047 Dec 3, 2001

29. Riko Wichmann, Properties of the Hadronic Final State I Diffractive Deep Inelastic Scattering Tagged with the Leading Proton Spectrometer of ZEUS, PhD thesis, Universiti of California 1999, Zeus-Note 99-079

30. Joost Herman Vossebeld, Dijet Photoproduction at High Transverse Energies, PhD thesis, Universiteit van Amsterdam, Sept 1999

31. ZEUS Collaboration; Neutral Strange Particle Production in Deep Inelastic scattering at HERA; DESY 95-084 April 1995

32. S. Chekanov, B. Levchenko, J. Repond, Inclusive φ(1020)-meson production in neutral current deep inelactic scattering at HERA; ZEUS-Note 01-047, December 3, 2001

33. Neils Tuning, ZUFOs: Hadronic final state reconstruction with calorimeter, tracking and backsplash correction, NUKHEF, University of Amsterdam, ZEUS-01021 June 27, 2001

34. R.R. Akhmetshin et.al., Study of the process $e^+e^- \rightarrow K_L^0 K_S^0$ in the c.m. energy range 1.05-1.38 GeV with CMD-2, Physics Letters B 551(2003) 27-34

35. W.M. Yao et. al., Particle Physics Booklet; Institute of Physics July 2006

36. ZEUS Collaboration, Measurement of isolated photon production in deep inelastic ep scattering, DESY-09-142, 30 Sept 2009

37. ZEUS Collaboration, Measurement of dijet photoproduction for events with a leading neutron at HERA, DESY-09-139, Sept 2009

38. ZEUS FNC Group, Design and Test of a Forward Neutron Calorimeter of the ZEUS experiment, DESY 97-006 January 1997, ISSN 014-9833

39. M. Reveline, Probing the Parton Evolution in DIS at low X_{jb} Using Jet Observables, PhD thesis, McGill University, DESY-THESIS-1999-005 February 1999

40. O. Biebel et.al, Fragmentation function in e^+e^- in annihilation and lepton-nucleon DIS, Review of Particle Physics Rev Aug 2007

41. Ewe Holm (ed.), The Zeus Detector Status Report 1993, Zeus Collaboration Feb. 1993

42. M. Barbi, Calibration and monitoring of the ZEUS Uranium Scintillator Calorimeter at HERA, McGilll University, Canada for the ZEUS Calorimeter Group

43. Shinji Kagawa; Study of the diffractive photoproduction o dijets in ep collision at Hera, Ph.D. Thesis, Department of Physics, University of Tokyo, Dec 21, 2004

44. Particle Data Group, Review of Particle Physics 2006, Institute of Physics Publishing

45. Shinji Kagawa, Signal – Noise Seperation in the Silicon Pad Detector of ZEUS; Mastet thesis, University of Tokyo, Jan 2002

46. G.F. Hartner, VCTRAK Briefing: Program and Math, ZEUS-Note 98-058, Aug 15, 1998

47. Niels Tuning, ZUFOs: Hadronic final state reconstruction with calorimeter, tracking and backplash correction, ZEUS-01-021 June 27, 2001

48. T. Sjöstrand, L. Lönnblad, S. Mrenna, Phytia 6.2 Physics and Manual, hep-ph/010264 LU TP 01-21 Aug 2001

49. Lief Lonnblad, Ariadne version 4: A Program for Simulation of QCD-Cascades Implementing the Colour Dipole Model Revision 12, Lund University Sweden, Oct 2001

50. H1 Collaboration, Forward π^0 Production and Associated Transverse Energy Flow in Deep-Inelastic Scattering at HERA, DESY 04-051 April 2004

51. H1 Collaboration, Search for Odderon-Induced Contribution to Exclusive π^0 Photoproduction at HERA, DESY 02-087 hep-ex/0206073 June 2002

52. A. Caldwell and S. Ritz, User Interface to the CAL Electronics Readout, ZEUS-Note 92-046
53. B. Schmidke, The CAL Readout; Columbia University/ZEUS Collaboration
54. F. Mohamad Idris, W.A.T. Wan Abdullah, Z.A. Ibrahim, M.A.F. Mat Jusoh, Y. Yamazaki, P. Goettlicher, W. Schmidke; FPGA Implementation of the Readout Control; CAL-HES Meeting ZEUS Collaboration February 2006
55. W. Wiggers, Shielding of proton-induced background, ZEUS-Note 87-012 March 1987
56. D.V. Gorbatkov, V.P. Kryuchkov, Space-energy characteristic of Radiation components behind high-energy accelerator shielding, Institute of High Energy Physics, Protvino, Moscow Region, Russia
57. T. Lampen; General Alignment Concept of CMS; Workshop on Tracking in High Multiplicity Environment 2005J.F. Zhou, In situ calibration of the forward and rear calorimeter using halo muons, ZEUS-Note 94-131, 31.10.1994
59. A. Freidhof, A Fürtjes, Muons from the proton halo: a precision test to monitor the F/CAL calibration, ZEUS-Note 93-076, September 1993
60. Claudia Buettner, Relative energy calibration with halo muons in the first inner ring of FCAL and RCAL, 20 Oct 2005
61. Xiang Liu, A quick study on halomuon trigger with run 46179, 47987 and 47989, Feb 29, 2004
62. Xiang Liu, A quick study on halomuon trigger with run 46179, 47987 and 47989, Feb 28, 2004
63. Paul de Jong, Status of the uranium calorimeter reconstruction software, user guide version 2.00, ZEUS-Note 92-019, version 1.00, Feb 29, 1992

64. ZEUS Collaboration, Measurement of K_S^0, Λ and $\overline{\Lambda}$ production at HERA, DESY, DESY 06-0026 December 2006